A STUDY OF T = 1, T = 3/2, AND T = 2 STATES IN SOME LIGHT NUCLEI USING (He^3, n) REACTIONS

Thesis by
Eric George Adelberger

In Partial Fulfillment of the Requirements

For the Degree of
Doctor of Philosophy

California Institute of Technology
Pasadena, California
1967
(Submitted March 15, 1967)

ACKNOWLEDGMENTS

It is a distinct pleasure to acknowledge the stimulating and thoroughly enjoyable atmosphere provided by the staff of the Kellogg Radiation Laboratory. Especially pleasurable and helpful were numerous conversations with Professor C. A. Barnes, who suggested much of this work, and with Professor T. A. Tombrello. Dr. N. B. de Takacsy has been exceedingly generous with his time and his theoretical insights. I am deeply indebted to Dr. F. S. Dietrich III who introduced me to the techniques of time-of-flight spectroscopy. Financial assistance from the National Science Foundation and the California Institute of Technology is gratefully acknowledged. It has been a pleasure to work with Mr. A. B. McDonald in the later stages of these experiments, and to have had the able assistance of Mr. R. W. Moore in data reduction. Finally, I wish to thank my wife for choosing to spend weekends with me in the incomparable high mountains of California, rather than prosaically typing up this thesis.

ABSTRACT

The (He^3, n) reactions on B^{11}, N^{15}, O^{16}, and O^{18} targets have been studied using a pulsed-beam time-of-flight spectrometer. Special emphasis was placed upon the determination of the excitation energies and properties of states with T = 1 (in Ne^{18}), T = 3/2 (in N^{13} and F^{17}) and T = 2 (in Ne^{20}). The identification of the T = 3/2 and T = 2 levels is based on the structure of these states as revealed by intensities and shapes of angular distributions. The reactions are interpreted in terms of double stripping theory. Angular distributions have been compared with plane and distorted wave stripping theories. Results for the four reactions are summarized below:

1) $O^{16}(He^3, n)$. The reaction has been studied at incident energies up to 13.5 MeV and two previously unreported levels in Ne^{18} were observed at $E_x = 4.55 \pm .015$ MeV ($\Gamma = 70 \pm 30$ keV) and $E_x = 5.14 \pm .018$ MeV ($\Gamma = 100 \pm 40$ keV).

2) $B^{11}(He^3, n)$. The reaction has been studied at incident energies up to 13.5 MeV. Three T = 3/2 levels in N^{13} have been identified at $E_x = 15.068 \pm .008$ MeV ($\Gamma < 15$ keV), $E_x = 18.44 \pm .04$, and $E_x = 18.98 \pm .02$ MeV ($\Gamma = 40 \pm 20$ keV).

3) $N^{15}(He^3, n)$. The reaction has been studied at incident energies up to 11.88 MeV. T = 3/2 levels in F^{17} have been identified at $E_x = 11.195 \pm .007$ MeV ($\Gamma < 20$ keV), $E_x = 12.540 \pm .010$ MeV ($\Gamma < 25$ keV), and $E_x = 13.059 \pm .009$ MeV ($\Gamma < 25$ keV).

4) $O^{18}(He^3, n)$. The reaction has been studied at incident energies up to 9.0 MeV. The excitation energy of the lowest T = 2 level in Ne^{20} has been found to be $16.730 \pm .006$ MeV ($\Gamma < 20$ keV).

Angular distributions of the transitions leading to the above higher isospin states are well described by double stripping theory. Analog correspondences are established by comparing the present results with recent studies of (t, p) and (He^3, p) reactions on the same targets.

TABLE OF CONTENTS

I. INTRODUCTION

This thesis describes an investigation of the (He^3, n) reactions on targets of B^{11}, N^{15}, O^{16}, and O^{18}, with special emphasis on the determination of the excitation energies and properties of states with T = 1 (in Ne^{18}), T = 3/2 (in N^{13} and F^{17}) and T = 2 (in Ne^{20}). The neutrons were detected and studied by means of a pulsed-beam time-of-flight spectrometer which is described in Part II of the thesis. Because of current interest in the electromagnetic splitting of isobaric multiplets an effort was made to obtain as precise values as possible for the excitation energies of the T = 3/2 and T = 2 levels.

The identification of the levels with T = 3/2 in the $T_z = 1/2$ nuclei and T = 2 in the $T_z = 0$ nuclei is, of necessity, somewhat indirect. The widths of these states cannot be measured with the present technique since they are expected to be much less than the experimental resolution. They lie at high excitation energy where the level density is so great that one cannot identify them on the basis of excitation energy alone, since many states may lie within the range of excitations where the higher isospin state is expected.

The identifications therefore were made on the basis of the structure of these states, as shown by angular distributions and intensities, using the selection rules imposed by a simple, one-step, stripping mechanism. These can be summarized as,

$$\begin{aligned} \Delta A &= 2 \\ \Delta \vec{T} &= 1 \\ \Delta \pi &= (-1)^{L} \\ \Delta \vec{J} &= \vec{L} \ , \end{aligned} \tag{1}$$

where L is the orbital angular momentum of the transferred proton-pair which can usually be inferred from the shape of the neutron angular distribution. The first two selection rules, on A and T, are of course quite rigorous, depending only upon the properties of the nucleon. The last two are approximate, depending on the s-wave purity of the He^3 wave function, which is quite good, and upon the validity of the assumed model of a one-step stripping process. The latter assumption is somewhat questionable since simple stripping must compete with other reaction mechanisms (such as stripping with core excitation, the so-called heavy-particle stripping, and compound nuclear formation). This simple model, however, will be shown to be rather successful in describing the reactions reported in this thesis. It should be noted that for (He^3, n) stripping, unlike deuteron stripping, there is no ambiguity in the selection rule for J.

The $\Delta \vec{T} = 1$ selection rule is, of course, one of the main reasons why this reaction is so attractive as a device for studying states of higher isobaric spin. Although the (p, n) reaction has the same selection rule, it is not expected to be as effective in identifying the low-lying T = 3/2 levels in the light nuclei with

$A = 4n + 1$. (A similar argument applies to the $T = 2$ levels.) To see this, we shall assume that the extreme single particle shell model describes the lowest lying $T = 3/2$ levels, which are bound in the $(4n + 1)$ nuclei with respect to the strong interactions. Then the lowest $T = 3/2$ level in F^{17}, for example, should have a two-particle, one-hole configuration based on an O^{16} core. The "quasi-elastic" (p, n) reaction on O^{17} should mainly populate single-particle states, especially the ground state of F^{17}, which is the "mirror" of the O^{17} ground state. In other words, it changes T_z but not T. $N^{15}(He^3, n)$ on the other hand, will strongly populate two-particle, one-hole states and should be much more effective than $O^{17}(p, n)$ in identifying the lowest $T = 3/2$ levels in F^{17}.

The influence of the structural properties of the higher isospin levels upon the intensities observed in a one-step stripping process is well illustrated by the reaction $Be^9(He^3, n)C^{11}(T = 3/2)$. This transition is, of course, allowed by the isospin selection rules. However, the spin and parity of the lowest $T = 3/2$ level in C^{11} are expected to be $1/2^+$ (Talmi and Unna 1960) which cannot be reached by a one-step stripping process except via 1s hole impurities in the Be^9 ground state, or by placing a proton in the 2s shell. The (He^3, n) transition in this case should be very weak. We have examined this reaction and were unable to see the transition to the lowest $T = 3/2$ level.

In order to take full advantage of the selection rules (1) it is necessary to determine the transferred angular momentum L. In order to extract this quantum number, one needs a detailed theory of the stripping process. The simplest form of such a theory uses the Plane Wave Born Approximation (PWBA). Although it has been claimed that the PWBA is never a good approximation (see for

example Satchler 1964) it has the virtue of yielding analytic solutions. A widely used approximate form of this theory for double stripping (Newns 1960) yields the expression

$$\frac{d\sigma}{d\Omega} \propto \exp(-K^2/4\gamma^2) j_L{}^2(kr_o) , \qquad (2)$$

where

$$\vec{K} = \frac{1}{3}\vec{k}_{He^3} - \vec{k}_n ,$$

$$\vec{k} = \vec{k}_{He^3} - \frac{m_I}{m_F}\vec{k}_n ,$$

$$\gamma = .255\ f^{-1} ,$$

m_I and m_F are the masses of the target and residual nuclei, and r_o is a cutoff which should be on the order of the nuclear radius. This approximation has met with some success in describing the shape of angular distributions, particularly in the extensive study of (t, p) reactions by Middleton and Pullen (1964a, 1964b). However, absolute cross sections predicted by the theory are quite unreliable. Furthermore, Middleton and Pullen have pointed out that for negative Q-value transitions the plane wave theory is very sensitive to the choice of r_o, since k is not necessarily small at forward angles. It is often possible to get equally good fits with several L-values by making small changes in r_o. Therefore, they regard L-value assignments for negative Q-value transitions as tentative. This defect in the theory is of serious concern in the present study since the transitions

of interest have Q-values between -3.2 and -8 MeV. Similar difficulties with the plane wave theory were encountered in this work and are discussed in Part III.

Recently it has become practical to make a more sophisticated approximation, in which the first Born Approximation matrix element is taken between elastic scattering, rather than plane waves. This distorted wave Born Approximation (DWBA) in which the scattering waves are generated by the optical model has been treated extensively; a detailed discussion is given by Bassel, Drisko, and Satchler (1962).

Although DWBA calculations cannot be carried out analytically without making unsatisfactory approximations, a vast body of deuteron stripping data has been successfully fitted by DWBA calculations in many cases where difficulties were encountered with the PWBA. Recently a few two-nucleon DWBA stripping calculations have been published which appear to be quite successful (see for example Glover and Jones 1966b). We have also attempted to fit our data using the DWBA, with results which are, in general, quite acceptable. The success of the calculations has made it possible to extract some unambiguous L-values (which was not possible with the plane wave theory) and supports the assumption that a one-step stripping process dominates the (He^3, n) transitions to the observed low-lying states with T = 1, T = 3/2, and T = 2. Since DWBA two-nucleon stripping calculations have not been extensively treated in the literature, a brief discussion of this topic is presented in Appendix B.

The logical outline of the work presented here is as follows: 1) Since the identification of higher isospin levels rests upon the double-stripping model, we first tested the model in a case where the structure of the low-lying states of the residual nucleus is fairly

well known, the reaction $O^{16}(He^3, n)Ne^{18}$. This reaction was studied in some detail and it was found that the DWBA theory provided an acceptable description of the transitions to the low-lying levels of Ne^{18}. This work is discussed in Part IV.

2) Having thus achieved some confidence in the double-stripping model, in Parts V, VI, and VII we describe a search for higher-isospin states in the reactions $B^{11}(He^3, n)N^{13}(T = 3/2)$, $N^{15}(He^3, n)F^{17}(T = 3/2)$ and $O^{18}(He^3, n)Ne^{20}(T = 2)$. These reactions were expected to populate the low-lying higher-isospin levels strongly and this expectation has been well confirmed in the present work, and in an earlier study of the reaction $Li^7(He^3, n)B^9(T = 3/2)$ by Dietrich (1964, 1965).

II. APPARATUS

The experiments reported here were all performed using the pulsed-beam time-of-flight spectrometer facility at the ONR-CIT tandem accelerator. This system has been described previously (Dietrich 1964). However, since 1964 several important changes have been made which significantly improve the performance of the system. We shall therefore describe the spectrometer with particular emphasis upon those features which have been modified since 1964.

A. Beam Pulsing System

A schematic drawing of the beam pulsing system is presented in Figure 1. The continuous beam from the tandem accelerator is chopped into pulses with a duration of approximately one nanosecond by applying a radio frequency (RF) voltage to a pair of deflection plates located at the high energy "tee" of the tandem. The beam is swept vertically (in order to avoid interfering with the energy regulation of the tandem) at 3.531 MHz across a pair of chopping slits located near the image focus of the 90-degree analyzing magnet, immediately behind the slits used to regulate the accelerator. Placing the chopping slits at the image rather than between the object of the 90-degree analyzer and magnet itself as was done prior to 1964 offers several advantages. Since the chopping slits are after the image slits, a larger beam current is available for regulating the tandem, which makes it easier to obtain regulation before the beam has been tuned for maximum current. Also since the beam spot at the new slit location has a smaller

diameter (being close to the image focus) and is a greater distance from the deflector, a smaller angular deflection is needed to obtain a given burst duration.

In order to increase the time-averaged pulse beam current, the ions are velocity modulated (bunched) before entering the tandem so that the current immediately before the chopping slits passes through sharp maxima. If the phase and amplitude of the bunching voltage are properly adjusted the current maxima will occur just as the beam is sweeping past the slit opening and the beam current pulses will be greatly enhanced (Dietrich 1964).

Two separate bunchers are required--one for negative-ion (hydrogen isotope) injection and one for neutral (helium isotope) injection. This is necessary since the helium ions have already been neutralized before passing through the negative-ion buncher. (see Figure 1).

In order for the bunching to be effective the fluctuations in the mean flight time τ_F of ions from buncher to deflector must be smaller than the beam burst duration δ, or else the current maxima will be out of phase with the deflector. This requirement of phase stability imposes a severe restriction on the energy spread $\Delta E/E$ of the ion source,

$$\frac{\Delta E}{E} < \frac{\delta}{\tau_F} \quad . \tag{3}$$

For example, in the case of neutral injection, helium ions are injected at 650 keV and must travel about 13 meters before being accelerated and passing through the deflector. If one desires 1.5 nanosecond bursts, the injection energy must therefore be regulated to better than 500 eV to gain full advantage from the buncher.

Prior to 1965 the small electrostatic generator which serves as a helium ion injector was regulated only by the generating voltmeter; the energy stability was so poor that constant manual control of the injection energy was necessary to achieve time-averaged He^{3++} currents as high as 30 nanoamperes, even with bursts as long as 5 nanoseconds.

Following a suggestion of C. A. Barnes an improved energy regulator for the helium injector was installed in early 1965. It derives its energy regulation signal from the un-neutralized fraction of the injected beam which is momentum analyzed by deflection in the 20^{o} magnet supplied with the accelerator. The improved injector still required constant manual fine control of the injection energy, but allowed one to obtain time-averaged He^{3++} currents up to 100 nA with approximately 2 nanosecond beam bursts. This method of beam stabilization could probably have been much improved by deflecting the charged beam through a larger angle and by improving the optical properties of the deflection magnet, both of which would have required the acquisition of a new magnet.

However, accurate regulation of the injection energy is not the only way to achieve phase stability. As an alternative, one can accept relatively poor regulation of the injection energy and electronically adjust the phase of the bunching waveform to compensate for variations in the injection energy. In the summer of 1966 a phase stabilizer working on this principle was developed. Details of the stabilizer principles and circuitry are found in Appendix A. With the phase stabilizer in operation time-averaged He^{3++} currents up to 200 nA with 1.5 nanosecond bursts are achieved with no manual control of the energy regulation. In addition, the beam

current is very steady, which greatly simplifies tuning procedures on the tandem accelerator.

It is interesting to consider some of the factors which limit the shortness of the beam bursts as observed at the target. These are:

1) the minimum attainable burst duration at a point immediately after the chopping slits,

2) the spreading of the bursts due to variations in the lengths of orbits between the chopping slits and target,

3) the spreading of beam bursts due to space charge effects, and

4) the spreading of the bursts due to fluctuations in beam energy. Such fluctuations come from the energy modulation introduced by the buncher and chopper as well as imperfect regulation of the tandem.

Let us consider these in inverse order. The distance from chopping slits to the target is approximately 20 meters. Over this distance a 10 keV variation in the energy of a 10 MeV He^3 beam will produce a flight time difference of only 0.4 nanoseconds. The energy spread introduced by the buncher should be less than 10 keV since the most heavily modulated ions do not arrive at the deflector in phase to pass through the slits.

A direct calculation of space charge effects is quite difficult. However, Flerov (1957) has bunched a 200 keV ion beam to give 0.5 nanosecond bursts and peak currents of 5 mA. Since peak currents

on the Caltech tandem after bunching are at best only $\sim$ 30 μA, it is not expected that space charge effects are a significant factor in determining the beam burst duration.

Next we estimate the possible variations in path length of orbits between the chopping slits and the target. Since there are two quadrupole magnets along the 20 meter path between chopping slits and target we will consider that the beam passes through a point focus 3 times. The maximum variation in flight paths is given by the difference between the lengths of the "straight" orbit and the orbit limited by the magnet apertures, taken to be 2.5 cm in radius. In this case the variation in path length is only .25 mm. This corresponds to a time spread of 10 picoseconds which is negligible.

One might think that the duration of the beam bursts immediately after the chopping slits could be made shorter than 1 nanosecond, at the expense of beam current, merely by making the deflection voltage sufficiently large. This is not true for the deflection geometry used in these experiments. This can be seen as follows. Those ions which pass through the chopping slits (i.e., which have the correct vertical deflection) must all have passed through the deflection plates within a time interval which can be made very short by increasing the deflection amplitude. However, if the orbits between deflector and chopping slits are not isochronous, the beam bursts at the chopping slits cannot be shorter than the variation in transit time. In the geometry used here the orbits are definitely not isochronous because of the range in orbits allowed by the 90-degree analyzing magnet. We can estimate the magnitude of this effect as follows: We assume that inhomogeneities in beam

energy and slit spacings are negligibly small. We then assume that the beam at the foci of the magnet has the full angular spread allowed by the horizontal aperture of the magnet, taken to be 1.25" (Pearson 1963), so that the difference in path length of orbits which just graze the inner and outer edges of the vacuum box is 1.75". (Variations in path length due to the $\Delta r/r$ allowed by the entrance and exit slits are negligible in comparison with this difference.) For 10 MeV He^{3++} ions, this corresponds to a minimum burst length of 1.75 nanosecond.

These calculations are supported by experience with the pulsed-beam apparatus. As the deflection voltage is increased to a certain value the time resolution of the system is improved and the time-averaged current goes down. If the voltage is increased to yet higher values the time-averaged current continues to drop--but the time resolution never gets better than about 1.8 nanosecond.

B. Neutron Detector and Shielding

A neutron detector for time-of-flight applications must have the following properties:

1) it must have a large enough area to subtend a reasonable solid angle at the flight paths contemplated (in this case 1.0-3.5 m).

2) it must detect the neutrons by as efficient a process as possible so that the detector thickness introduces only a small uncertainty in the flight path.

3) it must have a fast time response.

These requirements are conventionally met with a proton-recoil scintillation counter which takes advantage of the large p-n scattering cross section and the fast response of a plastic scintillator. All the work described in this thesis was done using a 2" thick by 5" diameter piece of "Pilot B" plastic scintillator mounted on a fast 5"-diameter phototube of type 58AVP or XP1040. The rise time of this combination is approximately 3 nanoseconds.

In order to reduce the background, principally gamma rays and neutrons, the detector is buried in a massive collimator and shield. Room-scattered neutrons are attenuated by a 6.5"-thick cylinder of lithium carbonate and paraffin while the gamma rays are attenuated by a lead cylinder 1.625" thick. Since a major source of the gamma background is from annihilation radiation produced by the positron decaying products of He^3-induced reactions, a 1/2"-thick lead disc is placed in front of the neutron detector. This attenuates 511 keV gamma rays by a factor of 8.5. The total neutron cross section for lead in the range 1.0-20.0 MeV is quite flat and neutrons in this energy region are attenuated only by a factor of about 1.5.

The collimation of neutrons with energies between 0.5 and 30 MeV is not as simple as for charged particles, however, and the shield is a mixed blessing as can be seen from Figure 27 which shows a $B^{11}(p, n)$ spectrum. Note that, although the gamma peak is very clean, the neutron peak has a pronounced tail on the side corresponding to longer flight times. This tail is not present when the detector is used without the shield, and seems to arise from two sources:

1) neutrons which scatter off the inner walls of the collimator and thus have longer flight times, and

2) (n, γ) reactions in the shielding material.

The main difficulty caused by the tail are ambiguities in determining the detector efficiency, and a distortion of spectrum shapes in complicated spectra-especially in those cases with a pronounced continuum.

The detector, shielding, and fast electronics are all mounted on a cart which is constrained to move along a steel I-beam. The I-beam is pivoted about a spot directly below the target, allowing the detector to be easily and reproducibly placed at laboratory angles between 0 degrees and 150 degrees, and flight distances from 1.0 to 3.6 meters.

C. Counting Electronics

The electronic circuitry directly associated with the measurement of flight times is described and shown in a block diagram in Figure 3.

In pulsed-beam experiments the flight time is determined by the time interval between two signals--one derived from the detector and the other from either the beam current pulse at the target or the RF waveform used in the beam pulsing apparatus. In the present work, the START pulse for the time-to-pulse-height converter (TPHC) is taken from the neutron detector and the STOP pulse from the RF waveform.

Two signals are obtained from the photomultiplier tube, a fast bipolar timing signal from the anode, and a slow, charge-measuring signal taken from dynode 11. The anode signal is clipped at the tube base by a shorted cable 37 cm long, producing a fast signal which is roughly proportional to the time derivative of the current pulse at the anode and crosses through zero with a large positive slope. The START pulse for the TPHC is generated

by a discriminator which "picks off" the zero crossing point of the fast signal. Ideally the zero-crossing discriminator (ZCD) should produce a pulse with a constant shape whose delay relative to the zero crossing time should be independent of the amplitude of the start pulse, that is, it should exhibit no "time-slewing". The majority of the data for these experiments was taken using a Tektronix Type 661 Sampling Oscilloscope as a ZCD--with the START pulse obtained from the Delayed Pulse output of the oscilloscope. The oscilloscope has a slewing of 1-1.5 ns/20db, and provides a convenient monitor of the apparatus. In addition, a ZCD was developed based on a design of Brafman (1965). It has superior slewing properties but has a more limited dynamic range.

The slow signal from the photomultiplier is used to gate the multichannel analyzer. It is amplified and fed into a lower level discriminator which rejects almost all phototube noise and those pulses due to events producing insufficient light to give good time resolution. Thus the discriminator bias partially determines the detector sensitivity, especially for low energy neutrons.

The STOP pulse for the TPHC is derived from the RF signal induced in a two-turn loop located near the plates of the beam deflector. The signal is amplified and squared before being fed to a discriminator which therefore "picks off" the time at which the RF signal went through zero.

The performance of the detector and counting circuitry was tested as shown in Figure 4. A Na^{22} source was used as a source of coincident 511 keV gamma rays and was viewed by two scintillation counters both using XP1040 tubes. The phototube, scintillator, and fast electronics in one channel were those used in the time-of-flight work. The other channel used similar apparatus. The resolving

time of the apparatus was 1.5 nanoseconds FWHM, which yields approximately 1.0 nanoseconds per counter and associated electronics, since the time converter and slow amplifier contributes little to the observed time spread.

With the improved resolution made possible by the phase stabilizer it was found that phase drifts in the STOP pulses were a major source of line width broadening. This contribution to the resolution was greatly reduced in the summer of 1966 by using a digital spectrum stabilizer operating on the prompt gamma peak to adjust the zero level of the analyzer to compensate for the STOP pulse drift.

It was also found that a 1% change in the amplitude of the chopping voltage caused a shift of 0.1 nanosecond in all peaks. In order to reduce this source of phase drift, an automatic gain control was added to the main chopper amplifier.

D. Target Chambers and Integration

Since both solid and gaseous targets were employed in the course of this work two different target chambers were used. The chamber used for solid targets was made of glass and was of conventional construction. The gas target is shown in Figure 5. The nickel entrance foils used were nominally 5000 angstroms thick. The gas cell is constructed of stainless steel and lined with tantalum to reduce the empty target background.

In all cases the targets were held at +300 V to prevent loss of electrons caused by secondary emission from the target, and the

beam passed through a suppressor electrode at -300 V before reaching the target. Integrated beam charge was collected on an Eldorado Model CI-110 Current Integrator which was used to gate the multichannel analyzer.

III. EXPERIMENTAL METHOD

A. Calibration of the Time Scale and the Measuring of Q-Values

We first discuss some general features of the time spectra obtained in this work and then discuss the techniques by which they are converted into equivalent spectra with neutron energy as the independent variable.

All spectra were taken using 200 channel subgroups of the RIDL analyzer with the time scale chosen to be approximately 1 ns/channel. However, due to extreme nonlinearity in the multichannel analyzer the lowest 20 channels are unuseable so that in effect the longest measureable flight time is about 180 nanoseconds.

Since the time-to-pulse-height converter measures the interval between a START pulse triggered by a neutron arriving in the detector and the next STOP pulse, short flight times correspond to large pulses from the time converter. Thus, neutron energy increases with increasing channel number. Since the STOP pulses are not, in general, coincident with the arrival of beam bursts at the target, but are delayed by a constant but arbitrary interval, one cannot measure flight times directly. Instead, one always measures the difference in flight time between neutrons and the prompt gamma ray group which is present in all our spectra.

The time scale calibration and calculation of relativistic Q-values were performed with the aid of a 7094 program developed by Dietrich (1964). At the beginning of every running day a linearity spectrum (see Figure 6) was taken with a Cs^{137} source producing the START pulses, and the STOP pulses generated as usual from the RF waveform. Since these time intervals are random, the linearity

spectrum would be flat if the time-to-pulse-height converter, amplifier, and analyzer were indeed linear. The linearity spectrum is first "smoothed" by averaging the counts in a given channel with those on either side of it, and then a time interval proportional to the counts in the smoothed spectrum is assigned to each channel. The proportionality constant can then be evaluated if the time difference between any two channels is known.

Two methods for producing peaks separated by a known time interval were used. The most convenient is to use a calibrated delay cable inserted between the STOP pulse discriminator and the time converter to shift the time spectrum a known amount. The cable (approximately 100' of RG 8/U) was calibrated by two independent means - by using neutrons of known energy and by using an RF oscillator.

The calibration using neutrons was made by producing neutrons of about 1 MeV from the $B^{11}(p, n)$ and $Li^{7}(p, n)$ reactions, for which the Q-values are well known. The flight paths and energies were adjusted so that the flight time difference between neutrons and gammas was nearly equal to the delay time of the cable. The mean of seven separate determination gives a delay time of 149.5 ± 0.2 nanoseconds.

The calibration using an oscillator was made by shorting one end of the cable and driving the other end with an oscillator. The driving frequency was adjusted to produce a node in the standing wave pattern at the oscillator end of the cable, and this frequency was measured using the Hewlett Packard Frequency Meter which is used in the NMR apparatus. Ten nodes were found corresponding to the fundamental and the first nine harmonics. The ten frequencies f_n were fitted with an empirical formula

$$L = (\frac{n}{2} - .00621)/f_n \quad , \tag{4}$$

and give a mean delay time of 150.5 ± 0.1 nanoseconds. Combining these results yields 150.0 ± 0.5 nanoseconds for the cable length, which provides an accurate enough time calibration for all but the most precise work.

When the maximum precision was desired from the time-of-flight spectrometer, as in the accurate determination of Q-values, a different means of calibrating the time scale was employed. A calibration reaction with a well known Q-value was used to produce neutrons having essentially the same energy as the neutron group from the level under study. Then the spectrometer was used only as a device for comparing flight times, and errors due to non-linearities in the time scale, uncertainties in the flight path, etc., cancelled out. In addition, some other important sources of error are partially cancelled by the procedure, for example, possible errors in the calibration constant of the 90^{o} analyzing magnet.

With this calibration technique, errors in the resulting Q-value are usually dominated by uncertainties in the incident beam energies. Therefore, the calibration reaction was chosen so that the effects of any systematic errors in the beam energies were minimized.

In order to minimize the effects of differential hysteresis in the beam analyzing magnet, the following procedure was used in setting the magnet current during Q-value determinations. The magnet current was first increased to approximately 40 A., then reduced to zero, before carefully setting the current so as not to "overshoot" the resonance on the NMR magnetometer.

B. Determination of Detector Efficiency

The pulse height spectrum produced by monoenergetic neutrons incident upon a proton-recoil scintillator extends from zero up to a maximum value determined by the neutron energy. Thus the detection efficiency is a function of the bias used in the slow channel.

In order to keep the efficiency reproducible from day to day the bias was always set by the following technique. The lower-level discriminator was adjusted to reject those pulses having a height less than a point half way down the high energy side of the Compton edge of 662 keV Cs^{137} gamma radiation. The gain of the slow amplifier preceding the discriminator was then increased by a factor of eight, effectively lowering the threshold by the same factor. The gain of the photomultiplier was always set so that all events which exceeded the bias in the slow channel also triggered the time-to-pulse-height converter.

The relative detection efficiency was measured with neutrons from the T(p,n) reaction, produced in a zirconium-tritide target. The efficiency was determined using the same detector and shielding geometry employed for all the work described here to eliminate the need for corrections due to scattering and absorption in the collimator and shield.

The results of this determination are displayed in Figure 7. Here we have used the T(p, n) cross sections of Wilson et al. (1961) and Goldberg et al. (1961). The curve in Figure 7 is an expression derived by Dietrich (1964) in which multiple scattering, scattering from carbon, and scattering and absorption in the collimator and

shield are all neglected, and the (n, p) cross section is approximated by a simple analytical expression. Agreement is better than 5%, and for all purposes in data reduction the relative efficiency was taken to be the value given by Dietrich's expression with an error of ± 5%.

An absolute determination of the detection efficiency was made for 6.23 MeV neutrons using the D(D, n) reaction and a gas target. With the assumption that the effective temperature of the gas along the beam path did not differ appreciably from the temperature of the walls of the cell, and using the cross sections of Goldberg and LeBlanc (1960), the detection efficiency was measured to be 0.323 ± .033 at 6.23 MeV. Dietrich's expression predicts 0.282. All absolute cross sections were computed using Dietrich's expression with an uncertainty of ± 10% in the absolute normalization.

C. Determination of Level Widths

The determination of level widths using time-of-flight spectroscopy is difficult since the energy resolution of the apparatus depends upon many factors, some of which are very difficult to determine accurately. Among the factors which contribute to the resolution are beam energy resolution, beam burst length, electronic resolution, the total neutron flight time, the flight time of neutrons through the scintillator, and target thickness; the resolution function depends in a complicated way upon neutron energy and the energy of the incident beam.

It is sometimes possible to measure the resolution of a given experimental configuration directly. This can be done if there exists a reaction which allows one to produce neutrons with the energy

of interest leading to a very sharp state, without changing the beam energy or target thickness appreciably. Then the resolution is simply given by the observed width of the sharp group. Unfortunately this is usually not possible when studying highly excited levels populated by (He^3, n) reactions, since there are almost no known sharp states with high thresholds available for comparison.

It is possible, however, to calculate the resolution function by making some reasonable approximations. These are:

1) The electronic resolution for neutrons is independent of neutron energy and identical to the electronic resolution for gammas. This assumption is not strictly valid because the electronic time resolution for events which produce little scintillation light is broadened by statistical fluctuations, and neutrons of interest usually produce smaller pulses than the gammas. However, variations in the electronic time resolution will not be very important since the total resolution for gamma rays has been measured to be 1 nanosecond, and we are dealing with an overall resolution of 3-5 nanoseconds for low energy neutrons.

2) The time resolution function due to the finite scintillator thickness can be approximated by a rectangle.

3) The beam energy spread is due entirely to energy losses in the target, and that the time resolution function due to this effect can likewise be approximated by a rectangle.

The shape of the prompt gamma peak present in all our time spectra is due to the effects of the beam burst duration plus the electronic resolution (which according to assumption 1) is the same for neutrons and gammas). The resolution function for neutrons is

then obtained by folding in the effect of the finite scintillator thickness and energy losses in the target. This is easily done by numerical methods. Of course, this technique does not reproduce the "tail" due to the collimator. The procedure has been checked by computing the widths of neutron groups corresponding to bound levels in the residual nucleus, and comparing these with the observed widths. This technique predicts the widths to within 0.2 channels. For a sample fit see Figure 2. It is interesting to note that the predicted width of bound groups is always slightly less than the observed width, which is reasonable since assumptions 1) and 3) both cause us to slightly underestimate some contributions to the width.

Once the resolution function is known, level widths can be determined in a straightforward manner by folding the time resolution into the natural level shape, and varying the level width to give the best fit. The natural level shape is obtained by converting a Breit-Wigner shape into the corresponding function which has flight time as the independent variable.

IV. A STUDY OF THE $O^{16}(He^3, n)Ne^{18}$ REACTION

A. Introduction

The low lying T = 0 and T = 1 levels in the mass 18 nuclei have received considerable theoretical attention since they may be described with some success as two interacting nucleons outside a doubly closed O^{16} core. Experimental work has been directed almost exclusively toward O^{18} and F^{18}, since at tandem energies Ne^{18} can be reached only via the $O^{16}(He^3, n)$ reaction. A good summary of experimental and theoretical work on the low lying states of O^{18} is given by Litherland et al. (1961) and Ollerhead et al. (1965). Previous work on the $O^{16}(He^3, n)$ reaction by Towle and Macefield (1961) using the counter ratio method had located levels in Ne^{18} at 1.88, 3.36, and 3.61 MeV excitation.

Gale et al. (1961) and Krick and Legge (1966) have measured the angular distributions of neutrons corresponding to the ground and first excited states and interpreted the results in terms of Newns' plane wave theory (1960).

Our interest in the $O^{16}(He^3, n)Ne^{18}$ reaction was originally directed toward testing double-stripping theories and this reaction provides an excellent test case. It was possible to obtain accurate experimental data since spectra are characterized by prominent sharp peaks and a weak continuum. This contrasts with the usual situation with (He^3, n) reactions where the continuum dominates, and uncertainties in the background subtraction are a major source of error. The theoretical interpretation was also expected to be quite "clean". Because of the 6.05 MeV gap between the ground and first excited states in O^{16}, core excitations should play a relatively

unimportant role, and the double-stripping selection rules allow only a single L-value for each transition since the O^{16} ground state has J = 0. In addition wave functions for the T = 1, A = 18 levels, expressed as two coupled nucleons surrounding an inert core, are available, which allows one to compute spectroscopic factors.

If we consider the extra-core nucleons in Ne^{18} to be restricted to the $d_{5/2}$ and $s_{1/2}$ subshells, we expect 6 states. From the $(d_{5/2})^2$ configuration we get the sequence 0^+, 2^+, 4^+, from $(s_{1/2})^2$ 0^+, and from $(s_{1/2}d_{5/2})$ a 2^+ and a 3^+ state. It has been suggested (Ollerhead et al. 1965) that the lowest 5 states in O^{18} (see isobar diagram in Figure 18) are due mainly to these 0^+, 2^+, and 4^+ configurations and that the 3^+ occurs at 5.37 MeV. The spin of the 6th excited state in O^{18} at 4.45 MeV has recently and unexpectedly been definitely established as 1 (Ollerhead et al. 1965) and there are strong indications that its parity is negative (Zeidman and Braid 1965). Such a state of course cannot be fitted into the simple model of an inert O^{16} core surrounded by two sd shell nucleons, and it cannot be populated by double stripping except via impurities (for example 2 particle-2 hole or 4 particle-4 hole) in the O^{16} ground state or by promoting a nucleon into the $f_{7/2}$ shell.

In light of the extensive work on O^{18} and the simple model of the mass 18 nuclei, it was deemed interesting to examine the mirror correspondences in Ne^{18}, and to use the reaction as a test of double-stripping theory.

B. Experiment

The $O^{16}(He^3, n)$ reaction was investigated at 8 different bombarding energies between 9.0 and 13.5 MeV. Angular distributions were taken at 9.0, 9.5, 10.5, 11.0 and 12.5 MeV. Three different targets were employed. The majority of the data was taken using a target formed by oxidizing a carefully cleaned blank of tungsten to a deep blue color in an induction furnace. Domingo (1963) reports that such targets have a chemical composition of $WO_{2.6}$ and are ~ 10 KeV thick for 2.6 MeV protons. This target was very stable and showed little tendency to pick up carbon. However, it had the disadvantage that the oxide layer was not well defined and therefore contributed some uncertainty to measurements of excitation energies and widths.

The gas cell (shown in Figure 5) with a 5000 Å nickel entrance foil was used to obtain absolute cross sections, and permitted the thickness of the tungsten oxide target to be computed by comparison of yields from the $WO_{2.6}$ and gas targets.

For Q-value measurements attempts were made to use a target prepared by evaporating BaO onto tantalum, but it picked up carbon so rapidly that useful results were difficult to obtain.

At all energies studied, the continuum is very weak and time spectra are dominated by sharp groups corresponding to previously observed states in Ne^{18} at 0.0, 1.88, 3.36, and 3.61 MeV excitation energy. These groups are readily resolved in the 9.0 MeV spectrum shown in Figure 8. In addition spectra taken at 12.5 and 13.5 MeV (Figures 9 and 10) show intense groups corresponding to previously unobserved levels in Ne^{18} at excitation energies of 4.55 and 5.14 MeV. No other narrow groups were seen at excitations in Ne^{18} up to 7.6 MeV.

We demonstrate that the 4.55 and 5.14 MeV groups do indeed correspond to levels in Ne^{18} in Figure 11. Here we have plotted the measured Q-value of the transitions to these levels assuming targets with $14 \leq A \leq 18$. We have made measurements at laboratory angles up to 150^{o}. The points for the correct target mass should lie on a horizontal line. It is seen that in both cases the best fit to a single Q-value is obtained for an A = 16 target, and targets with A = 14, or A = 18 are definitely excluded.

N^{15} can definitely be excluded as responsible for either the 4.55 or 5.14 MeV state since it has been studied (see Section VI of this thesis) and no sign is seen of the continuum or the intense neutron group leading to the 3.10 MeV state in F^{17}. This state would produce neutrons of a higher energy than any groups from $O^{16}(He^{3}, n)$ and would be clearly visible.

The relative intensities of the Ne^{18} groups are the same for targets of tungsten oxide and natural oxygen gas. Since natural oxygen contains only 0.37% O^{17}, the observed intensity of the 4.55 MeV group in Figure 9 would require a zero degree differential cross section of 370 mb/sr if it arises from O^{17}. We conclude therefore that the 4.55 and 5.14 MeV states are definitely in Ne^{18}.

C. Excitation Energies

Q-values for the $O^{16}(He^{3}, n)$ reaction leading to the previously unobserved levels at 4.55 and 5.14 were made using both the $WO_{2.6}$ and BaO targets. The time scale in these measurements was calibrated using the ground state group from the $B^{11}(p, n)$ reaction.

The energy loss of protons in the B^{11} target was found indirectly by using the magnetic spectrometer to determine the energy loss, in the boron layer, of He^3 ions elastically scattered from the tantalum target backing. This energy loss was then scaled for protons using the tables of Demirlioglu and Whaling (1962). The energy loss in the BaO target was determined in a similar manner; however, the intense elastic scattering from the barium complicated the determination.

The energy loss of He^3 ions in the tungsten oxide target was estimated in two ways:

1) The $O^{16}(He^3, n)$ yield from the oxide target was compared with the yield from O^{16} in a gas cell, to give the number of O^{16} atoms/cm^2 in the oxide target. The target was then assumed to consist of a layer of $WO_{2.6}$ followed by pure W. The energy loss in the $WO_{2.6}$ layer was computed using the tables of Demirlioglu and Whaling. This method estimated the target as being 44.6 keV thick to 9.9 MeV He^3 ions.

2) The 10 keV energy loss given by Domingo for 2.6 MeV protons in the $WO_{2.6}$ targets was scaled to He^3 ions using the tables of Demirlioglu and Whaling. With this method the target thickness is estimated as 35.4 keV for 9.9 MeV He^3 ions. The discrepancy between the determinations is small enough that it contributes negligibly to the uncertainty in the incident energy.

A sample calculation of the Ne^{18} Q-values taken from runs using the tungsten oxide target is summarized in Table I. A sample calculation of errors in the derived excitation energies is summarized in Table II. From the runs with the BaO target we obtain $E_x = 4.55 \pm .018$ and $E_x = 5.13 \pm .02$ MeV; for the tungsten oxide

measurements we find $E_x = 4.545 \pm .016$ and $E_x = 5.15 \pm .02$ MeV. A major contribution to the quoted errors arises from uncertainty in the beam energies. This error is systematic (we cannot be sure that proton and He^3 orbits through the analyzing magnet do not differ slightly) and we therefore combine our results to give $E_x = 4.55 \pm .015$ and $E_x = 5.14 \pm .018$ MeV. The uncertainty in incident energy $\pm \delta E$ was taken to be one half of the theoretical maximum beam spread $\pm \delta E_m$ allowed by the slits (see Pearson 1963)

$$\frac{\delta E}{E} = \frac{1}{2} \frac{\delta E_m}{E} = \frac{1}{2} \left(\frac{S_1 + S_2}{R} \right) \qquad (5)$$

where E is the beam energy.

$2 S_1$ and $2 S_2$ are the full widths of the object and image slits and R is the radius of the 90^o magnet, taken to be 34".

The only other significant source of error lies in the location of the centers of the peaks corresponding to the levels in Ne^{18}. This error is dominated by counting statistics. A spectrum from which one of the Q-value measurements of the 4.55 MeV state was taken is presented in Figure 12.

D. Widths

The levels at 4.55 and 5.14 MeV are unbound to particle decays into $F^{17} + p$, and $O^{16} + p + p$(the 5.14 MeV state can also decay via $O^{14} + \alpha$), and hence have measurable widths. Widths for these levels were obtained from runs using both the barium oxide and tungsten oxide targets. The resolution function was calculated as described in Section IIIC of this thesis. The level widths were

found by folding the time resolution into that function which corresponds to a Breit-Wigner curve in an energy spectrum. The level width was adjusted to give the best fit by a chi-square test, with the experimental and calculated points normalized to the same area. With this procedure we obtain widths of 70 ± 30 keV for the 4.55 MeV state, and 100 ± 40 keV for the 5.14 MeV state. The errors are largely statistical and should be interpreted as standard deviations.

E. Angular Distributions

Angular distributions taken at 9.0, 10.5, and 12.5 MeV incident energy are presented in Figures 13, 14, and 15 respectively. Sample spectra from which these distributions were derived are shown in Figures 8 and 9. The choice of background is indicated by the straight lines. In the 9.0 and 10.5 MeV spectra, the groups corresponding to the 0.0, 1.88, 3.36, and 3.61 MeV levels are clearly resolved, and the new levels are not visible. At 12.5 MeV, the 3.36 and 3.61 MeV levels are not resolved, but the 4.55 and 5.14 groups are quite intense. The 10.5 MeV distribution was taken with a gas target and hence cross sections at this energy are absolute. Cross sections were computed by the relation

$$\left.\frac{d\sigma}{d\Omega}\right|_{CM} = Y \frac{d\Omega_L}{d\Omega_{CM}} \frac{d^2}{Q\eta} \frac{q}{n} \frac{1}{p} \times 3.839 \times 10^{-2} \text{ mb/sr} \qquad (6)$$

where $Y = N_{TOT} - N_{BACK}$ is the experimental yield with background subtracted.

Q = total charge collected

η = detector efficiency - taken as the value predicted by Dietrich's expression

d = flight path in meters

qe = charge of bombarding ion

n = atoms/molecule in the target gas

p = pressure in cm Hg of the target gas

The numerical constant is evaluated for a gas cell 1.54 cm long containing gas at a temperature of 293°K.

The error bars include contributions from counting statistics, uncertainty in choice of the mean background, and a 5% uncertainty in beam current integration and relative detector efficiency. The relative errors ϵ were computed by the relation,

$$\epsilon = \pm \left[\frac{N_{TOT} + (\delta N_{BACK})^2}{(N_{TOT} - N_{BACK})^2} + (.05)^2 \right]^{1/2}, \qquad (7)$$

where N_{TOT} is the total number of counts under a peak,

N_{BACK} is the number of background counts under the peak, and

δN_{BACK} is the uncertainty in the mean background under the peak.

In addition to the errors denoted by the flags there is an estimated uncertainty of ± 10% in the absolute normalization.

When this work was begun, we expected that the (He^3, n) results would be similar to those found at E_t = 10 MeV in the mirror reaction O^{16}(t, p)O^{18} by Middleton and Pullen (1964b). This data is shown in Figure 16, the smooth curves are plane-wave fits (Newns 1960). All levels can be fitted with a radius of 5.5f except for the 4.45 MeV state which is very weak and does not seem to be reached by stripping, and the 5.33 MeV state which requires 5.0f.

We have also analyzed our data at 9.0 and 12.5 MeV incident energy using the plane-wave theory. See Figures 13 and 15. The data can be fitted equally well with several sets of L-values by making small changes in the cutoff radius. The sensitivity of the shape of the plane-wave distributions to the choice of cutoff radius appears to be most pronounced in negative-Q transactions, an effect that has previously been observed by Middleton and Pullen.

L-values for the levels at 4.55 and 5.14 MeV were obtained by assuming that the spins and parities of the ground and first excited states of Ne^{18} could be inferred from the systematics of even - even nuclei and the known values in the mirror nucleus. This fixed the L-value for these transitions as 0 and 2 respectively and required cutoff radii between 4.0 and 4.75f. A search for L = 0, 1, 2, or 3 fits was then performed using cutoff radii between 3.75 and 5.25f, leading to tentative assignments of 1^- for the 4.55 MeV state and 0^+ or 2^+ for the level at 5.14 MeV. The 2^+ assignment is favored since it requires a radius closer to that used in fitting the other levels.

There are several troublesome points in the plane-wave analysis:

1) It is impossible to get a good fit to the ground and first-excited states using the same radius in both cases. This is true at both 9.0 and 12.5 MeV incident energy.

2) The cutoff radius necessary to fit an experimental distribution with a given L-value is energy dependent. For the L = 0 ground state transition Gale et al. (1961) use 4.3f at 5.6 MeV. We need 4.5f at 9.0 MeV and 4.0f at 12.5 MeV.

3) The radii required by our data (4.0 - 4.75f) are much smaller than the 5.5f value used in the mirror reaction O^{16}(t, p). However, our cutoff is consistent with the 4.0f value we find for the $B^{11}(He^3, n)$ reaction (see Figure 28). In the B^{11}(t, p) reaction, however, Middleton and Pullen use a radius of 5.0f. Thus, it appears that (He^3, n) transitions require systematically smaller radii than found for the (t, p) reactions on the same targets.

Distorted wave calculations were undertaken to see if the DWBA would remove the ambiguities found with the plane-wave theory. Results for the data at 10.5 and 12.5 MeV are presented in Figures 14 and 17. The potentials used, taken without modification (except for Coulomb effects) from an analysis of the O^{16}(t, p) by Glover and Jones (1966b), are listed in Table XIV. The only free parameters are the normalizations. The fits are quite good, especially for the L = 0 transition, and are unambiguous as to L-value. It is not possible to greatly alter the shape of distributions by changes in the potentials and, except near threshold, different L-values have distinct shapes. In these and other respects the DWBA is clearly superior to the plane-wave theory.

An interesting and unexplained feature of this reaction is the variation in the shape of the angular distribution of the 1.88 MeV state. The zero-degree minimum is comparatively shallow at 9.0 and 12.5 MeV (Figures 13 and 15), and quite deep at 10.5 MeV (Figure 14) and 9.5 and 11.5 MeV (not shown). The dip appears to be deepest at incident energies around 10 MeV, as can be seen in the zero-degree spectrum taken at 9.9 MeV (Figure 12).

With the 10.5 and 12.5 MeV angular distributions and DWBA fits it is possible to assign spins and parities to some of the levels in Ne^{18}, and to find mirror correspondences between O^{18} and Ne^{18}. An isobar diagram of the mass-18 nuclei which summarizes this is presented in Figure 18. The ground and first excited states are well fitted by L = 0 and L = 2, and hence can definitely be assigned spin parities of 0^+ and 2^+ respectively. The analogs in O^{18} are obvious. The 3.61 MeV level is fitted by L = 2, and not by L = 0, 1, 3, or 4. It probably is the analog of the 3.92 MeV state in O^{18}. The angular distribution of the 3.36 MeV "state" cannot be fitted with L = 0, 1, 2, 3, or 4. It is therefore likely that this "level" is an unresolved doublet corresponding to the 4^+ and 0^+ states in O^{18} at 3.55 and 3.63 MeV. In Figure 14 we have fitted the 3.36 MeV level with a mixture of L = 0 and L = 4, and it seems satisfactory.

The 4.55 and 5.14 MeV states are unbound to diproton decay and cannot be handled by our DWBA code, forcing us to rely upon the plane-wave results. We obtain fits for the 5.14 MeV state for both L = 0 and L = 2. The state has a significant (100 ± 40 keV) width and may be a resolved doublet consisting, perhaps, of analogs of the 5.25 MeV 0^+ and 5.33 MeV 0^+ states in O^{18}. Such an assignment is favored by the relative intensities in the $O^{16}(He^3, n)$ and $O^{16}(t, p)$ reactions.

When we try to fit the 4.55 MeV state into the O^{18} level sequence we find some striking difficulties. The $O^{16}(He^3, n)$ transition to this level is quite strong, and is fitted in plane-wave theory by L = 1, and not by L = 0, 2, or 3. The plane wave L = 1 assignment must be tentative, but the level is intense and well fitted by L = 1, indicating that the reaction is most likely proceeding by one-step stripping. We shall consider three levels in O^{18} as possible analogs of the 4.55 MeV state:

1) the O^{18} 4.45 MeV 1^- state. This state is an obvious choice since it would require the smallest level shift (+30 keV between F^{18} and Ne^{18}) of the three candidates, and its known spin and parity is consistent with the strong L = 1 transition to the Ne^{18} 4.55 MeV state. However, the O^{18} 4.45 MeV state is very weakly populated in the $O^{16}(t, p)$ reaction, as would be expected for L = 1 stripping from a doubly closed O^{16} core. If these states are analogs, the departure from mirror symmetry is quite remarkable. The ratio of peak cross sections of the "1^-" level to the ground state is seven times greater in $O^{16}(He^3, n)$ than in $O^{16}(t, p)$. See Figures 15 and 16. This apparent violation of isospin conservation does not necessarily imply that the 4.45 and 4.55 MeV levels are not isobaric analogs, since a similar difficulty is found for the lowest 2^+ states in O^{18} and Ne^{18} which are clearly analogs. The ratio of peak cross sections of the lowest 2^+ state to the ground state is 2.5 times greater in $O^{16}(He^3, n)$ (Figure 15) than in $O^{16}(t, p)$ (Figure 16).

2) the O^{18} 5.09 MeV state. If this state were the analog of the 4.55 MeV state it would require a larger level shift (-570 keV between F^{18} and Ne^{18}). The angular distributions in the $O^{16}(He^3, n)$ and $O^{16}(t, p)$ reactions to the states have different shapes, and the

peak cross section of the transition (in each case normalized to the ground state) is three times larger in the $O^{16}(He^3, n)$ reaction.

3) the O^{18} 5.25 MeV 0^+ state. If this state were the analog of the 4.55 MeV level it would require a large (-710 keV between F^{18} and Ne^{18}) level shift, but the peak cross sections of the transition (normalized, in each case, to the ground state) are about equal in the $O^{16}(He^3, n)$ and $O^{16}(t, p)$ reactions.

The L = 1 plane wave assignment favors alternative 1). If this assignment is correct, mirror symmetry is apparently broken. This apparent violation of isospin conservation may occur in either the O^{16} target or in the residual nuclei O^{18} and Ne^{18}. The strong L = 1 transition in $O^{16}(He^3, n)$ suggests that O^{16} has a substantial p-shell hole impurities. This is consistent with the wave functions of Brown and Green (1966) who find that the O^{16} ground state is 0.874 0p-0h, 0.469 2p-2h, and 0.130 4p-4h. The difference in $O^{16}(t, p)$ and $O^{16}(He^3, n)$ transitions to the 4.5 MeV states appears to imply either that

1) the impurities in the O^{16} wave function violate isospin conservation, being more important in the proton shell, or

2) that the wave functions for the presumed analog states in Ne^{18} and O^{18} are different.

It is quite unexpected that the Coulomb interaction in such light nuclei should cause so blatant a departure from mirror symmetry. The solution to this intriguing puzzle must await further study, and perhaps a DWBA theory for unbound states.

F. Conclusions

We have investigated the $O^{16}(He^3, n)$ reaction at incident energies up to 13.5 MeV, corresponding to excitation in Ne^{18} up to 7.6 MeV. In addition to previously reported levels at 0.0, 1.88, 3.36, and 3.61 MeV excitation the reaction populates levels at $4.55 \pm .015$ and $5.14 \pm .018$ MeV. Angular distributions to all levels show characteristic stripping patterns.

Some difficulties were experienced in analyzing our data with plane-wave stripping theory (Newns 1960), rendering the L values obtained somewhat uncertain. For the 0.0, 1.88, 4.55, and 5.14 MeV levels we find L = 0, L = 2, L = 1, and L = 0 or 2 respectively.

On the other hand, calculations using the distorted wave Born approximation reproduce shapes and intensities quite faithfully. The DWBA calculations give L = 0, L = 2, and L = 2 for the 0.0, 1.88, and 3.61 MeV states respectively. The 3.36 MeV state can be fitted with a mixture of L = 0 and L = 4. Higher levels are unbound to diproton decay and cannot be handled with conventional DWBA theory.

A striking departure from mirror symmetry may have been observed in the transition to the 4.5 MeV state in the $O^{16}(t, p)$ and $O^{16}(He^3, n)$ reactions. The Ne^{18} state is populated strongly in $O^{16}(He^3, n)$ with L = 1, the O^{18} state has been found to have $J = 1^-$, but is very weak in $O^{16}(t, p)$. This discrepancy merits further investigation.

V. OBSERVATION OF T = 3/2 STATES IN N^{13} USING THE REACTION $B^{11}(He^3, n)N^{13}$

A. Introduction

In the $T_z = 1/2$ light nuclei with $A = 4n + 1$ $(n > 1)$, the lowest $T = 3/2$ levels are bound with respect to isospin-conserving particle decays. Thus, they are expected to be quite narrow, in spite of their high excitations. The first such levels to be seen were in mass 9. Lynch, Griffiths, and Lauritsen (1965), studied $Li^7(He^3, p)Be^9$ $(T = 3/2)$ and Dietrich (1964, 1965) used $Li^7(He^3, n)$ to study B^9 $(T = 3/2)$. Continuing this program, we have searched for $T = 3/2$ states in N^{13} using the reaction $B^{11}(He^3, n)$.

Prior to this work and the related study of $B^{11}(He^3, p)C^{13}$ by Hensley and Barnes (1965), very little was known about the $A = 13$, $T = 3/2$ isobaric multiplet. As usual, the $T_z = -3/2$ member of the quartet had received the most attention. Middleton and Pullen (1964a) used $B^{11}(t, p)$ to see the ground and first nine excited states of B^{13}, and assigned seven L-values using plane-wave double-stripping theory. No $T = 3/2$ states were known in either C^{13} or N^{13}. O^{13} was seen via its delayed proton activity (Barton et al., 1963 and McPherson et al., 1965), but the mass was not directly determined.

One may estimate the mass of the lowest $T = 3/2$ level in N^{13} since the B^{13} ground state mass is known. We neglect Thomas-Ehrmann shifts and assume that except for Coulomb effects and the neutron-proton mass difference, the masses of the different members of an isobaric multiplet are identical. Then we may write the mass of a member of an isobaric multiplet as

$$M(T_z) = Z(M_p + M_e) + (A - Z)M_n - B + Z(Z - 1)KA^{-1/3} \quad (8)$$

where B is the binding energy of the strong forces and is taken to be constant within a given multiplet, K is the Coulomb constant, which is assumed to be the same within an isobaric multiplet and for all levels of a given nucleus. We have, of course, neglected the electron binding energies. If we evaluate K from the C^{13} - N^{13} ground state mass difference, we can then use the B^{13} mass to predict an excitation of 15.17 MeV for the lowest T = 3/2 levels in N^{13} and C^{13}. The lowest T = 3/2 particle decay in N^{13} proceeds via C^{12} (T = 1) + p. Thus T = 3/2 levels with excitations less than 17.05 MeV are bound with respect to isospin-conserving strong decays. The first four excited states in B^{13} have excitations between 3.483 and 3.712 MeV. Therefore, by analogy we expect 4 T = 3/2 states in N^{13} at excitations between 18.65 and 18.88 MeV. These states would be unbound to strong decays and therefore expected to have appreciable widths.

It is interesting to note that equation (8) predicts that analogous levels in mirror nuclei should have equal excitation energies. This result depends upon the assumption that the Coulomb constant K is the same for all levels in a given nucleus. If we make the reasonable assumption that the nuclear radius is greater for the T = 3/2 states than for the T = 1/2 states we find that equation (8) predicts that the T = 3/2 states in a $T_z = -1/2$ nucleus (in the convention where T_z for the proton is +1/2) have higher excitations than the analogous states in the nucleus with $T_z = +1/2$. This is exactly what is observed in the A = 13 nuclei. The argument, however, ignores level shifts, which in some cases (mass 9 would seem to be a good example) are not negligible.

We may make some qualitative predictions about the configuration of the lowest T = 3/2 level in N^{13} using the extreme single particle shell model. If Coulomb mixing with T = 1/2 states is small, the simple shell model should be as valid an approximation for the lowest T = 3/2 levels as for the lowest T = 1/2 levels. Then, based on C^{12}, the dominant configuration of the lowest T = 3/2 state should be $(p_{3/2})^{-1}(p_{1/2})^2_{T=1,\ J=0}$. This is supported by the known J^π of B^{13} which is $3/2^-$. This configuration, which can be coupled to either T = 1/2 or T = 3/2, is readily reached by L = 0, one-step double-stripping, on B^{11} which is predominantly $(p_{3/2})^{-1}$. In fact in the approximation of a pure $(p_{3/2})^{-1}$ structure for B^{11}, $(p_{3/2})^{-1}(p_{1/2})^2_{T=1,\ J=0}$ is the only configuration reached by L = 0 stripping unless two nucleons are promoted across a major shell closure. Thus in this simple-minded picture we expect our spectra to be dominated by L = 0 transitions to low lying $3/2^-$ states with T = 1/2 and T = 3/2. This two-particle stripping strength should be concentrated upon the lowest T = 3/2 level, and upon the lowest T = 1/2 level with spin-parity $3/2^-$, which occurs at 3.51 MeV, because of the large energy gap between them and other $3/2^-$ states. The next T = 1/2, $J^\pi = 3/2^-$ state occurs at 9.47 MeV (Lauritsen and Ajzenberg-Selove 1962) while the next T = 3/2, $J^\pi = 3/2^-$ state is expected at 24.8 MeV (Boyarkina 1964).

We, therefore, expect to preferentially populate the lowest T = 3/2 state in N^{13} because its configuration is easily reached by one-step diproton stripping, whereas the neighboring T = 1/2 levels have complicated configurations which have a small overlap with $B^{11}(0.0)$ surround by two correlated protons. With these simple arguments it is not possible to make predictions about the higher T = 3/2 states.

B. Experiment

The B^{11} (He^3, n) reaction was studied at incident energies between 7.0 and 13.5 MeV, corresponding to excitation energies in N^{13} up to 20.4 MeV. Targets prepared by evaporating metallic boron enriched to 98.6% in B^{11} onto tantalum backings were kindly supplied by D. C. Hensley. These targets contained a significant oxygen contamination, which produced sharp neutron groups with energies close to those expected from T = 3/2 states in N^{13}. In an effort to reduce the oxygen content, later targets received a thin (estimated to be 100 Å thick) coating of gold before air was admitted to the belljar. With this procedure it was possible to reduce the oxygen content significantly.

Time spectra taken at incident energies of 7.0, 9.0, 12.5, and 13.5 MeV are presented in Figures 19, 20, 21 and 22. They are characterized at excitations above 1.94 MeV by an intense continuum due to the many possible multi-body breakups. The most prominent structures superimposed upon the continuum are sharp peaks at 3.51 and 15.07 MeV excitation energy in N^{13}. This is especially noticeable in the 9 MeV spectrum (Figure 20) and nicely confirms the simple arguments above based on double stripping.

At a beam energy of 13.5 MeV some additional structure at higher excitations is apparent. This can readily be seen in the spectrum of Figure 22, where, in addition to the peak at 15.07 MeV, an intense peak at 18.98 MeV excitation and a weaker one at 18.44 MeV are evident. The 18.98 MeV group can be distinguished in 12.5 MeV spectra (see Figure 21), but the 18.44 MeV group is not sufficiently prominent to stand out above the background. These two sharp groups lie in the excitation region expected for higher

T = 3/2 states in N^{13}. We tentatively (and perhaps brashly) suggest a T = 3/2 assignment.

We next demonstrate that the previously unobserved groups corresponding to levels in N^{13} at 15.07, 18.44 and 18.98 MeV are indeed in mass 13. In Figure 23 we have plotted the Q-values for the (He^3, n) transition to the 15.07 MeV state obtained from runs at laboratory angles between 0^o and 135^o under the assumption that the target mass was 10, 11, or 12. The points for the correct mass should lie on a horizontal line. The 15.07 MeV level is conclusively demonstrated to be in mass 13.

Unfortunately, it was not feasible to make Q-value measurements for the 18.44 and 18.98 MeV states over such a wide range of angles, and at neutron energies where the precision of the spectrometer was as great as for the 15.07 MeV level. The problem was especially severe for the 18.44 MeV state which is nearly obscured by the intense continuum and nearby structure. Due to the small angular range covered ($0^o \leq \theta L \leq 30^o$) and difficulties in locating the peak, the measured kinematic shift was consistent with $10 \leq A_{target} \leq 44$. We were not able to extend the angular range because the 18.44 and 18.98 MeV states are not sufficiently intense to be easily identified at back angles.

It was checked that neither the 18.44 or 18.98 MeV state could have been produced from the contaminants known to be present on the target. In Figures 24 and 25 spectra from the B^{11} target are compared with those observed when natural carbon and oxide targets were substituted for the B^{11} target without changing beam energy or detector geometry. It can be seen that the 18.44 and 18.98 MeV states could not be produced by these contaminants. Since the target was prepared from B^{11} with a nominal purity of

98.6% it is most unlikely that these states could be produced from B^{10} or any other contaminant.

The kinematic shift of neutrons corresponding to the 18.98 MeV state was measured with sufficient precision to restrict the target to A = 11. This is displayed in Figure 26 where the goodness of fit of the experimental Q-values to a constant is shown for various assumed target masses.

C. Excitation Energies

Q-value measurements of the $B^{11}(He^3, n)$ reaction leading to the sharp 15.07 MeV state were made at 7 MeV. For a typical spectrum see Figure 19. To obtain the greatest accuracy the spectrometer was used as a comparison device. After a (He^3, n) run the beam was changed from He^3 to protons as rapidly as possible (generally less than one hour elapsed between runs) and the $B^{11}(p, n)$ $C^{11}(0.0)$ reaction was run with the same target and detector geometry. For a sample spectrum see Figure 27. The incident proton energy was adjusted to give neutrons of the same flight time from both reactions.

The only significant errors in Q are due to uncertainties in the incident beam energy, Q-value of the calibration reaction, and location of the neutron and gamma peaks. The dominant uncertainty is in the effective beam energy. This arises from possible errors in the frequency constant of the analyzing magnet, the range of energies allowed by the finite regulating slits, and uncertainties in the mean energy loss in the target. The error due to the frequency constant is small since it is partially cancelled by the calibration reaction. The target thickness was determined by using the magnetic spectrometer to measure the energy loss in the boron layer of He^3 particles

elastically scattered from the tantalum backing. This was done before and after the series of runs which established the Q-value. The mean beam energy loss was taken to be one half the total energy loss. This is strictly valid only if (1) the yield is independent of energy and (2) contaminants in the target (most notably oxygen) have the same distribution in the target as the B^{11}. Since the total energy loss of 7 MeV He^3 particles in the target was only 47 keV it is unlikely that assumption (1) is not justified. We estimate an uncertainty in beam energy due to 2) of 5 keV.

The most important source of error is caused by the uncertainty in the incident beam energy allowed by the finite object and image slit spacings. These uncertainties were taken to be 1/2 of the theoretical maximum value (given by formula (5) and yielded an uncertainty in Q of 8 - 12 keV, depending upon the settings. Uncertainties in the beam energy of the calibration spectrum contributed from 4.6 to 6.6 keV uncertainty to the individual determinations. A Q-value determination was also performed using the $F^{19}(p, n)Ne^{19}(0.0)$ reaction to calibrate the time scale. A sample calculation for the Q-value obtained from the spectra displayed in Figures 19 and 27 is summarized in Table III. The calculation of the errors in this determination is summarized in Table IV.

Six separate determinations of the Q-value were made. The results are displayed in Table V. Four of these were independent in the sense that they were made on separate days, with independent tuning of the machine. The runs, however, are not independent in the statistical sense because of the possibility of systematic errors due to differing orbits of protons and He^3 ions through the 90^o

analyzing magnet. It is very difficult to estimate the size of such possible errors. We have arbitrarily quoted a error ± 8 keV, rather than ± 3 keV which is the standard deviation of the mean.

It is interesting to note that the spread of the individual determinations is consistent with a beam energy uncertainty of 1/3 the theoretical maximum, rather than the value of 1/2 the maximum that we used.

The excitation energy of the 18.98 MeV state was found by using $B^{11}(p,n)C^{11}(0.0)$ as a calibration reaction, and also from several runs using a standard delay cable to calibrate the time scale as discussed in Section IIIA. The Q-value calculation using the calibration reaction technique is summarized in Table VI and the errors in Table VII. The result is $E_x = 18.985 \pm .026$ MeV. From the data of Figure 26 taken at an incident energy of 12.529 MeV we obtain $E_x = 18.993 \pm .028$ MeV and from data taken at 13.522 MeV, where the precision is poorer, we find $18.952 \pm .039$. For the reasons stated above these determinations are not statistically independent; we combine them to give $E_x = 18.98 \pm .02$ MeV.

The excitation of the 18.44 MeV state was taken from runs at 13.522 MeV using the 18.98 MeV group to calibrate the time scale. The result is $E_x = 18.44 \pm .04$ MeV.

D. Widths

Widths for the 15.07 and 18.98 MeV levels were determined by computing the resolution functions as described in Part IIIC of this thesis. No attempt was made to find the width of the 18.44 MeV state since it was populated quite weakly and was not clearly resolved from nearby structure.

Upper limits on the width of the 15.07 MeV state were obtained from the same spectra used in measuring the excitation energy of this level. Therefore the method of computing resolution functions could be checked by comparing the computed line shape with the shape of the neutron group (corresponding to a level with negligible intrinsic width) in the calibration spectrum. It was found that the computed resolution function gave an intrinsic width of 15 keV for both the N^{13}(15.07) group and the C^{11} ground state group in the calibration spectrum. A fit of the resolution function to the C^{11} group is presented in Figure 2.

An explanation for the underestimate of the observed width of the resolution function is given in Part IIIC of this thesis. We conclude from our data that the width of the 15.07 MeV state is less than 15 keV. This state, however, has subsequently been seen in the elastic scattering of protons by C^{12} (Bredin, et al., 1966) and the width found to be less than 5 keV.

The width of the 18.98 MeV state was obtained from 4 spectra taken at 12.5 MeV incident energy (see Figure 21 for a sample spectrum). Widths of 40 ± 20, 40 ± 20, 53 ± 25, and 33 ± 20 keV are derived from these spectra. Since the three runs are not truly independent, but are sensitive to the computed resolution function, we combine these values to give a width of 40 ± 20 keV. The 18.98 and 18.44 MeV states have subsequently been seen in the scattering of protons by C^{12} (Kuan and Hanna 1966) and the widths found to be less than 20 keV. Our data do not appear to be consistent with such a small width. It is possible that in $B^{11}(He^3, n)$ we are actually seeing an unresolved doublet, of which only one component is seen in proton scattering.

E. Angular Distributions

An angular distribution of neutrons leading to the 15.07 MeV state was taken at 9.0 MeV incident energy. The extraction of peak areas from the spectra was subject to large uncertainties in the background subtraction. The difficulty is shown in Figure 20. Even with as good resolution as was conveniently attainable, the proper background was not obvious. At back angles the errors were mainly statistical (Figure 28). We have presented the data (Figure 29) as follows: At forward angles we have indicated limits of error established by the estimated maximum and minimum possible backgrounds. At back angles the errors are statistical. In addition the points at 0, 15, 20, and 30 degrees have been corrected for contributions from the Ne^{18}(1.88) group. The correction was made using the magnetic spectrometer to compare the yields from the O^{16}(d, p) reaction in the B^{11} target with a tungsten oxide target. Forward angle points were taken with both targets, and the normalization obtained with the (d, p) reaction was used to make the proper subtraction. The curves in Figure 29 are obtained from Newns' plane-wave theory for L = 0, since the level is expected to be $3/2^-$.

In a study of the B^{11}(t, p) reaction (Middleton and Pullen 1964a) the forward peaked angular distributions were well fitted by the plane-wave theory using a cutoff radius of 5f. Our data cannot be fitted with 5f, but is well described using 4f, in good agreement with the results of Hensley and Barnes (1965), and consistent with the L = 0 transition in our study of O^{16}(He^3, n).

DWBA calculations employing the potentials (except for differences in the Coulomb barriers) used in an analysis of C^{12}(t, p) (Glover and Jones 1966b) gave fair fits with L = 0, L = 1, and L = 2,

making it impossible to distinguish L-values. We make two observations concerning the DWBA calculations.

1) There is evidence that optical well depth increases markedly as the incident energy is lowered (Matous, Herling, and Wolicki 1967). The incoming potentials were derived for 12 MeV tritons and may work rather poorly for 9 MeV He^3's.

2) We have found that when the neutron energy is low (1-3 MeV) the DWBA angular distributions are frequently forward peaked and quite similar for L = 0, L = 1, and L = 2. The need for experimental resolution prevented us from obtaining an angular distribution at higher energies, where the distributions of different L-values have characteristically different shapes.

In Figure 30 we present an angular distribution of neutrons corresponding to the unresolved 3.51 and 3.56 MeV states in N^{13}. The smooth curve is an L = 0 fit using the plane-wave theory. We find that the forward peak is well fitted with a cut-off radius of 4.0 f. This confirms our expectation that the $B^{11}(He^3, n)$ reaction should primarily populate $3/2^-$ levels at 3.51 and 15.07 MeV. It is also of interest because the Q-value to the 3.51 MeV level is +6.67 MeV, suggesting that the small radii needed in our L = 0 fits are not due to a Q-value effect of the kind discussed by Middleton and Pullen (1964b).

A partial angular distribution of neutrons corresponding to the 18.98 MeV state was taken at a beam energy of 12.5 MeV. Results are displayed in Figure 31.

F. Conclusions

The (He^3, n) reaction on B^{11} strongly populates narrow levels in N^{13} at 3.51 and 15.068 MeV excitation energy. We suggest that these states consist predominantly of a $B^{11}(0.0)$ core surrounded by two protons in the configuration $(p_{1/2})^2_{\substack{T=1 \\ J=0}}$. The 3.51 MeV state has the total isospin coupled to 1/2, and we identify the upper state as the lowest T = 3/2 level in N^{13}. Angular distributions to both levels are strongly forward peaked. In addition to the lower T = 3/2 level at 15.068 MeV, other levels in N^{13} are observed at excitations of 18.44 and 18.98 MeV, the transition to the 18.98 MeV state being more intense.

Our T = 3/2 assignment for the state in N^{13} at 15.07 MeV is based primarily upon the intensity of the reaction and the proximity of the excitation energy to that expected for the lowest T = 3/2 state. In addition we have found that the width of this state is less than 15 keV, and the angular distribution of neutrons is fitted by L = 0, implying spin and parity $3/2^-$, which are expected for the lowest T = 3/2 level.

This state has been seen subsequently to the present work (Bredin et al., 1966) as a narrow ($\Gamma < 5$ keV) anomaly in the elastic scattering of protons by C^{12}, confirming our T = 3/2 assignment.

Our assignment of T = 3/2 to the levels at 18.44 and 18.98 MeV is likewise based upon the excitation energies, intensities and widths, although the evidence that these states have T = 3/2 is less compelling than for the 15.068 MeV state. The strength of the transitions to these states, especially to the 18.44 MeV level, is

less than to the lowest T = 3/2 level and complete angular distributions could not be obtained.

In Figure 32 we present a mass 13 isobar diagram, showing the results of this work, a related study of C^{13} by Hensley and Barnes (1965, 1966), and a recent determination of the O^{13} mass by Cerny et al., (1966) (who also found the masses of the lowest T = 3/2 levels in C^{13} and N^{13} with less precision than the present work). The correspondence between the (He^3, n) and (He^3, p) results is quite good. This is expected, since for isospin-changing transitions both reactions obey the same double-stripping selection rules.

We identify the 15.07 MeV state in N^{13} and the 15.11 MeV state in C^{13} as the analogs of the ground state of B^{13} and O^{13}. It is tempting to identify the N^{13} "state" at 18.44 MeV as the unresolved analogs of the 3.68 and 3.71 MeV states in B^{13}, and the 18.98 MeV state in N^{13} as the analog of the 4.13 MeV state in B^{13}. The tentative identification of the 18.44 MeV state is supported by evidence from proton scattering that the 18.4 MeV state may be complex, and by the work of Hensley and Barnes who see a partially resolved doublet at approximately 18.68 MeV. This may explain the slight dependence of the measured excitation energy upon neutron angle. This identification as well as the tentative assignment of the 18.98 MeV state as the analog of the 4.13 MeV state in B^{13} is suggested also by a comparison of relative intensities in the B^{11}(He^3, n) and B^{11}(t, p) reactions.

Some of the interest in locating the T = 3/2 levels of the 4n + 1 nuclei lies in the opportunity they provide to check the quadratic mass law for members of an isobaric multiplet (Wilkinson 1964), since there are 4 members of a T = 3/2 multiplet and only

three parameters in the mass law. With the known masses of B^{13}, C^{13} (T = 3/2), N^{13} (T = 3/2) we predict an O^{13} mass excess of 23.11 ± .04 MeV. The mass excess of O^{13} measured by Cerny et al., is 23.11 ± .07 MeV. We conclude that at this level of precision there are no deviations from charge independence other than a first order term which transforms like the Coulomb force under isospin rotations. However, a recent precise check of the mass law in the A = 9 system (Barnes et al., 1966) indicates that small deviations from the quadratic mass law are present, and that such deviations should be expected as higher order quantum electrodynamic effects.

VI. OBSERVATION OF T = 3/2 LEVELS IN F^{17} IN THE REACTION $N^{15}(He^3, n)$

A. Introduction

Prior to this work, and the concurrent study of O^{17} by Hensley and Barnes (1966) experimental information on the A = 17 T = 3/2 isobaric quartet was rather sparse. The delayed neutron emitter N^{17} had received the most attention. Although 21 levels had been observed in N^{17} (Hart, Norbeck, and Carlson 1965), the only spin assignment was $1/2^-$ for the ground state (based on beta decay). No T = 3/2 states had been reported in O^{17}. Two sharp anomalies ($\Gamma < 5$ keV) in the elastic scattering of protons by O^{16} were seen by Hardie, Dangle, and Oppliger (1964), at excitations in F^{17} of 12.522 and 13.039 MeV, and were conjectured to be possible analogs of the first and second or third excited states of N^{17}. No evidence was seen for the lowest T = 3/2 level. Two possible explanations for this were given by Hardie et al: that the level was so narrow it was masked by the 2 keV experimental resolution, in spite of 1% statistics, or else that the unobserved state was very broad due to strong Coulomb mixing with a nearby T = 1/2 level of the same spin and parity. The fourth member of the isobaric quartet, the delayed proton emitter Ne^{17} has been seen (McPherson et al., 1964) although its mass has not been determined.

It is possible to make some simple predictions about the T = 3/2 excited state spectrum in F^{17}. As was pointed out in Section VA, one can estimate the excitation of the lowest T = 3/2 level by expressing the atomic mass of a state belonging to an

isobaric multiplet as

$$M(T_z) = Z(M_e + M_p) + (A - Z)M_n - B + Z(Z - 1)KA^{-1/3} \qquad (8)$$

where B represents the binding energy due to the strong forces. This expression assumes that the Coulomb constant K is the same for all levels of a given nucleus. If K is evaluated from the F^{17} - O^{17} ground state mass difference the N^{17} mass can be used to predict 11.002 MeV as the excitation of the lowest T = 3/2 level in F^{17}. If, on the other hand, one uses the N^{15} - O^{15} ground state mass difference to evaluate K, the predicted excitation is 11.302 MeV. Thus, we expect the lowest T = 3/2 level at an excitation of 11.15 ± 0.15 MeV.

Although the lowest isospin-allowed particle decays of T = 3/2 levels in F^{17} are to N^{15} + 2p (see Figure 42), the lowest isospin-allowed single-particle decays occur via the T = 1 states of O^{16}; thus levels with excitations less than 13.39 MeV are bound with respect to these decays and are expected to be quite narrow, and to have have an appreciable probability for gamma decay. Therefore, in addition to a narrow level at about 11.15 MeV, one would expect a narrow state in F^{17} at about 12.52 MeV, and a pair of sharp states at about 13.03 MeV excitation energy, corresponding to the first, second and third excited states of N^{17}. Analogs of higher levels in N^{17} are unbound with respect to isospin-conserving decays, and are expected to be quite broad.

Although the ground state spin of N^{17} has not been determined unambiguously, observations of the beta-decay branching (Silbert and Hopkins 1964) suggest $1/2^-$. This is consistent with the extreme single-particle shell model which predicts a two-particle - one-hole configuration and thus $J^\pi = 1/2^-$.

Since the N^{15} ground state has most of the $p^{1/2}$-hole strength (Warburton, Parker, and Donovan 1965), one-step diproton stripping on N^{15} is expected to pick out states with the following configurations,

1) one-particle even-parity states ($d_{5/2}$ or $S_{1/2}$) which, of course, are T = 1/2 and necessitate an odd L.

2) two-particle one-hole odd-parity states ($(p_{1/2})^{-1}$ $(d_{5/2})^2$, $(p_{1/2})^{-1}$ $(S_{1/2})^2$, or $(p_{1/2})^{-1}$ $(S_{1/2})$ $(d_{5/2})$), which can be either T = 3/2 or T = 1/2 and which are reached by even L transitions.

It should be noted that even-parity, T = 3/2 levels can only be reached by crossing a major shell-closure and placing a proton in the 1f shell, or via core excitation or higher configurations in the N^{15} ground state.

Extensive calculations by Margolis and de Takacsy (1966) on negative parity states in A = 17 indicate that the two-particle - one-hole configurations are reasonably successful in fitting the low-lying odd-parity T = 1/2 levels. They confirm the simple shell model prediction for the configuration of the lowest T = 3/2 level; 90% of the amplitude is $(p_{1/2})^{-1}$ $(d_{5/2})^2$. They also find that the T = 1/2, J = $1/2^-$ level at 3.10 MeV is also predominantly $(p_{1/2})^{-1}$ $(d_{5/2})^2$.

B. Experiment

All work on the reaction was performed with the gas target chamber shown in Figure 5 containing N^{15} gas with a nominal isotopic purity of 99.9%. Pressures were chosen to give target thicknesses between 14 and 32 keV for the bombarding ions. The

calculated straggling of 5 MeV He^3 ions passing through the 5000 Å nickel entrance foil is 31 keV FWHM, which is less than the resolution of the spectrometer when operated under normal conditions. The energy loss of protons in the foil was determined by measuring the displacement of the narrow 872 keV F^{19} (p, $\alpha\gamma$) resonance when the foil was placed ahead of a thin calcium fluoride target. Results for one particular foil are shown in Figure 33. This proton energy loss was then scaled to He^3 with the tables of Demirlioglu and Whaling (1962). Although neutrons from $O^{16}(He^3, n)$ were detected in some early runs, no significant outgassing occurred once the target had undergone a few hours bombardment, after having been prepared by heating it and maintaining it under vacuum for several days before the run.

The reaction has been studied at He^3 energies up to 11.88 MeV. Zero-degree spectra have been taken at 16 different incident energies between 7.72 and 11.88 MeV and angular distributions obtained at 10.36 and 11.88 MeV.

The time spectra bear a strong qualitative resemblance to those obtained from the reaction $B^{11}(He^3, n)N^{13}$ as can be seen by comparing Figures 21 and 34. In both cases we see:

1) An intense continuum due to the many open multi-particle channels.

2) The ground and first excited states, which in this case must be populated by L = 3 and L = 1 capture of a diproton, are only weakly excited.

3) The lowest lying L = 0 transition, in this case to the $1/2^-$ level at 3.10 MeV, is extremely strong.

4) That the only sharp structure at high excitations consists of prominent peaks at excitations very close to those expected for the T = 3/2 levels.

A spectrum taken at 11.88 MeV incident energy is presented in Figure 35. Previously unobserved narrow groups appear at 11.20, 12.54, and 13.06 MeV. No other sharp structure is seen at excitations up to 14.3 MeV. These levels cannot be attributed to any likely contaminants in the target gas, and empty target runs showed no pronounced structure.

C. Excitation Energies

Excitation energies for the levels at 11.195, 12.540, and 13.059 MeV were measured using the calibration-reaction technique, which permits accurate work with a gas target since any errors in the foil thickness (as well as in the calibration constant of the analyzing magnet) nearly cancel in the derived Q-values.

Two largely independent measurements of the 11.195 MeV state were performed. The measurements were made on different days, using different 5000 Å entrance foils, and different calibration reactions. The calibration reactions selected, $N^{14}(\alpha, n)$ and $N^{15}(\alpha, n)$, are both induced by α particles since there are no suitable (He^3, n) reactions with sufficiently well known, negative Q-values. We feel that by using (α, n) instead of (p, n) calibration reactions, we reduce the possibility of systematic errors due to differing orbits through the analyzing magnet. All measurements were made at zero degrees where $dE/d\theta$ is least, and cross sections are largest. Beam energies were chosen so that in each case neutrons of about 1.1 MeV were produced from the levels of interest.

The $N^{14}(\alpha, n)$ calibration reaction has the advantage that the magnetic rigidity of the α's is within 10% of the rigidity of the He^3's at the energies chosen. However, the energy loss in the foil is 214 keV for the α's, and only 163 keV for the He^3's. On the other hand the choice of $N^{15}(\alpha, n)$ as a calibration has the advantage that the energy loss of α's was 164 keV, compared with 144 keV for the He^3's. Since these two values are so close, any errors in the foil thickness are reduced by a factor of 20 in the derived Q-values.

The measurement using $N^{14}(\alpha, n)$ as a calibration yielded $E_x = 11.200 \pm 0.010$ MeV; using $N^{15}(\alpha, n)$ to calibrate the time scale we get $E_x = 11.190 \pm 0.011$ MeV. The main contributions to the quoted errors are due to uncertainties in the incident beam energy which was taken to be 1/3 of the theoretical maximum allowed by the 0.100 inch object and image slit spacings. Combining these results we arrive at a final value of $E_x = 11.195 \pm 0.007$ MeV. The calculations are summarized in Tables VIII and IX. The $N^{15}(He^3, n)$ and $N^{15}(\alpha, n)$ spectra used in one determination of the excitation of the 11.195 MeV level are shown in Figures 36 and 37.

The excitations of the 12.54 and 13.06 MeV levels were measured using the $N^{15}(\alpha, n)$ reaction at 8.915 MeV as a calibration, and also using a 150 nanosecond calibrated delay cable to measure the neutron energy. The calculations are summarized in Tables X and XI. The errors again are dominated by uncertainties in the incident beam energy. It was checked that the yield of the $N^{15}(He^3, n)$ and $N^{15}(\alpha, n)$ reactions did not vary greatly with a change of $\pm$ 50 keV in incident energy. Our assumption that the mean beam energy loss in the gas is 1/2 of the total energy loss in the gas is therefore justified.

D. Widths

An upper limit for the width of the 11.195 MeV level was obtained by comparing the shape of the neutron group from $N^{15}(He^3, n)$, with that from the particle stable 3.36 MeV level in N^{18}, populated by $O^{16}(He^3, n)$. It was necessary to change the beam energy by only 5% in order to produce reactions of the same energy from both reactions. The gas pressures were chosen so that the energy losses in the N^{15} and O^{16} in the target were nearly equal. Then, if the energy straggle and beam burst duration are assumed not to change with a 5% change in beam energy, the shape of the neutron group from F^{17}(11.195) should be given by the shape of the group for Ne^{15}(3.36) folded into the intrinsic level width of 11.195 MeV state. A Breit-Wigner curve, with flight time as the independent variable, was folded into the shape of the neutrons from Ne^{18}(3.36) and the level width adjusted to give the best fit to the group from F^{17}(11.195). The goodness of fit was determined by a chi-square test, with the calculated and experimental points normalized to the same area, leading to an upper limit of 20 keV for the width of the 11.195 MeV state. However, since this level was not seen by Hardie et al., (1963) its width is probably less than a few keV.

This technique could not be used to establish significant upper limits for widths of the 12.540 and 13.059 MeV levels because the increased beam energy needed to reach these states appreciably reduced the straggle in the foil, causing the F^{17} groups to be narrower than the calibration group from Ne^{18}(3.36).

An estimated upper limit of 25 keV for the width of the 12.540 and 13.059 MeV levels was obtained by assuming that all contributions to the width combine quadratically, and that the straggle in the entrance

foil of the gas cell is described by the formula of Evans (1955). Then we assume the observed width of a level Γ_o be given by

$$\Gamma_o^2 = \Gamma_\gamma^2 + \Gamma_{st}^2 + \Gamma_g^2 + \Gamma_{sc}^2 + \Gamma_i^2 \qquad (9)$$

where Γ_γ, Γ_{st}, Γ_g, and Γ_{sc} are the widths due to the observed gamma group, the straggle in the foil, the energy loss in the gas, and the flight time through the scintillator respectively, and Γ_i is the intrinsic level width. Under these assumptions an upper limit for the widths of the 12.540 and 13.059 MeV levels is 25 keV. However, if these states are identified with the levels seen by Hardie et al., (1963) an upper level of 5 keV can be placed on these widths.

E. Angular Distributions and DWBA Fits

Angular distributions have been taken at 10.36 and 11.88 MeV corrected beam energy. At the lower energy only the two lowest T = 3/2 levels were recorded, while at 11.88 MeV, all three levels were strongly populated. The data are displayed in Figures 38 through 41. The error bars include contributions from counting statistics, uncertainty in the choice of background, and a 5% contribution from the detector efficiency and beam current integration. In addition to the errors denoted by the flags there is an estimated over-all uncertainty in the absolute normalization of ± 10%.

In Figures 39 through 41 the angular distributions taken at E_{He^3} = 11.88 MeV are displayed on a logarithmic scale, together with angular distributions from known L = 0, and L = 2 transitions in the $O^{16}(He^3, n)$ reaction at 10.5 MeV incident energy. The F^{17}

and Ne^{18} distributions are strikingly similar, as one would expect. The smooth curves are DWBA fits using the zero-range optical model code TSALLY. The curves were computed using published potentials (listed in Table XIV) derived from elastic scattering, there are no free parameters except for the normalization. The He^3 potentials are identical to those of Glover and Jones (1966a) derived from the 12 MeV elastic scattering of tritons on O^{16}. The neutron potentials are the proton potentials used by Glover and Jones (1966b) in fitting (t, p) data. Our calculations assumed that only a single radial quantum number was necessary to describe the motion of the diproton about the core. For a more complete discussion of the DWBA calculations see Appendix B.

The L = 0 transitions to F^{17}(11.195) and Ne^{18}(0.0) are both well fitted by the DWBA curves. The F^{17}(12.540) and Ne^{18}(1.88) angular distributions have nearly the same shape, and in both cases the L = 2 DWBA curves fail to reproduce the dip at 0^o, although they do reproduce the data at large angles. This discrepancy, while unfortunate, is not considered serious, in light of the crudeness of the calculation. The strong similarities with known transitions in Ne^{18}, together with the DWBA calculations, lead to unambiguous assignments of L = 0 and L = 2 for the F^{17}(11.195) and F^{17}(12.540) transitions respectively. This limits the spin and parity of the 11.195 MeV state to $1/2^-$, and of the 12.540 MeV state to $3/2^-$ and $5/2^-$. Hensley and Barnes (1966), in studying the analog of this level in $O^{18}(He^3,\alpha)O^{17}$, see an L = 1 transition which restricts the spin of the analog of the 12.544 MeV level to $1/2^-$ or $3/2^-$, leading to a likely spin assignment of $3/2^-$.

The level at 13.059 MeV is unbound with respect to diproton decay, and hence cannot be handled by conventional stripping theory.

Calculations arbitrarily assuming a 100 keV binding energy did not allow one to distinguish between different L-values.

F. Conclusions

The $N^{15}(He^3, n)$ reaction strongly populates three narrow levels at excitation energies of 11.195 ± 0.007 MeV (Γ < 20 keV), 12.540 ± 0.010 MeV (Γ < 25 keV), and 13.059 ± 0.009 MeV (Γ < 25 keV). Double-stripping angular distributions lead to spin-parity assignments of $1/2^-$ for the 11.195 MeV level, and $3/2^-$ or $5/2^-$ for the 12.540 MeV state. These levels are identified as analogs of the ground, first, and second or third excited states of N^{17}. The levels at 12.540 and 13.059 MeV can be associated with the previously reported (Hardie et al., 1963) anomalies in the elastic scattering of protons by O^{16}, leading to an upper limit of 5 keV for width of these states. Since the 11.195 MeV level was not seen by Hardie et al., its width is probably less than a few keV. The T = 3/2 assignment of these three states is based upon the excitation energies, the spins, the narrow widths, and the intensities of the transitions.

The $1/2^-$ levels at 3.10 and 11.195 MeV are both intensely populated in the $N^{15}(He^3, n)$ reaction indicating that these levels look very much like an N^{15} core surrounded by two closely correlated protons. These results are consistent with the calculations of Margolis and deTakascy (1966).

The angular distributions to the T = 3/2 levels are reasonably well described by DWBA double-stripping theory, confirming that two-nucleon stripping is the dominant mechanism in these transitions.

An isobar diagram of the T = 3/2 levels in the A = 17 nuclei is presented in Figure 42. It summarizes the present work and

includes the T = 3/2 levels in O^{17} found by Hensley (Barnes et al., 1966) using the reactions $O^{18}(He^3,\alpha)$ and $N^{15}(He^3, p)$. The correspondence between the (He^3, n) and (He^3, p) results is quite good, as one would expect, since for isospin changing transitions the two reactions obey the same selection rules. The $O^{18}(He^3,\alpha)$ reaction populates analogs of the three T = 3/2 states seen in the present work as well as two other states not seen in $N^{15}(He^3, p)$ or $N^{15}(He^3, n)$. A comparison with Hensley's work suggests that the 13.059 MeV state in F^{17} is the analog of the third excited state in N^{17}.

Subsequently to the present work, a narrow ($\Gamma < 1.8$ keV) anomaly has been observed in the inelastic scattering of protons to the 6.13 and 7.12 MeV states of O^{16} (Patterson, Winkler, and Zaidens, 1967) at $E_p = 11.277 \pm .015$ MeV. This corresponds to an excitation energy in F^{17} of $11.203 \pm .015$ MeV. Since the lowest T = 3/2 state in F^{17} has a configuration which is predominantly two particle - one hole, one would expect that the state should decay primarily to one particle - one hole states in O^{16}. This may explain why no anomaly corresponding to the lowest T = 3/2 level in F^{17} has been seen in the elastic scattering of protons by O^{16}, and why anomalies are seen in the inelastic scattering to the lowest negative-parity states in O^{16}.

VII. OBSERVATION OF THE LOWEST T = 2 STATE IN Ne^{20} IN THE REACTION $O^{18}(He^3, n)$

A. Introduction

The first experimental observation of states with $T = T_z + 2$ was made by Garvey, Cerny, and Pehl (1964) who used the (p, t) pickup reaction on T = 1 targets to populate levels in the residual nucleus with T = 0, T = 1, and T = 2. Garvey, et al., bombarded targets of Mg^{26}, Ti^{46}, and Fe^{54} with 39 MeV protons, and identified the lowest T = 2 states in Mg^{24}, Ti^{44}, and Fe^{52} in the triton spectra. Subsequently, Cerny, Pehl, and Garvey (1964) found the two lowest T = 2 levels in both O^{16} and Ne^{20}, by bombarding O^{18} and Ne^{22} with 44 MeV protons. The identification of the T = 2 levels in the above work rested partly upon angular distributions and the proximity of the observed levels to the expected positions of these states. The most important evidence for the T = 2 character of these states, however, lay in the intensity of the transition. Garvey, et al., (1964) pointed out that (p, t) pickup should selectively populate the lowest T = 2 levels in the nuclei studied and pick them out of the dense background of T = 0, and T = 1 levels. In the present work we report upon the observation and accurate determination of the excitation energy of the lowest T = 2 state in Ne^{20} using the reaction $O^{18}(He^3, n)Ne^{20}$. We thus demonstrate that two nucleon stripping, as well as pickup, can selectively populate low-lying T = 2 states.

Before discussing the experiment we make some observations concerning T = 2 structure in Ne^{20}, and some characteristics of the $O^{18}(He^3, n)$ reaction. We can employ the relation

$$M(T_z) = Z(M_e + M_p) + (A - Z)M_n - B + Z(Z-1)kA^{-1/3} \qquad (8)$$

to predict the excitation energy of the lowest T = 2 level in Ne^{20}. We use the mass difference between F^{20}(0.0) and its known analog in Ne^{20} (at 10.27 MeV excitation) to evaluate the Coulomb constant K, and then use K to compute the Coulomb energy difference between O^{20} and Ne^{20}(T = 2). The formula predicts an excitation of 16.87 MeV. The lowest isospin-allowed particle decay of Ne^{20} occurs at an excitation of 20.27 MeV via F^{19}(T = 3/2) + p. O^{20} has a 2^+ state at 1.67 MeV excitation and a 4^+ state at 3.57 MeV. Therefore, in Ne^{20} we would expect a narrow T = 2, O^+ state at 16.9 MeV, a T = 2, 2^+ state at 18.5 MeV, and possibly a T = 2, 4^+ state close to 20.4 MeV, which may be shifted enough so that it falls below the isospin-allowed particle decay threshold. Other T = 2 states should be above this threshold and are expected to be quite broad. Cerny et al., find T = 2 states in Ne^{20} at 16.8 ± 0.1 and 18.5 MeV excitation energy. The 16.8 MeV state is quite prominent in their published spectrum; to distinguish the 18.5 MeV level in the published data requires considerably more talent.

The simplest theoretical treatment of the sharp isospin quintuplets in the A = 20 nuclei (Loncke and Pradal, 1966) treats these states as spherical four-particle states composed mainly of the ($1d_{5/2}$, $1d_{3/2}$, and $2s_{1/2}$) configurations. The dominant component of the lowest T = 2 level in this framework is $(1d^2_{5/2})_{\substack{T=1\\J=0}}$ $(1d^2_{5/2})_{\substack{T=1\\J=0}}$. This configuration can readily be reached with (He^3, n) or (t, p) stripping by O^{18} (which is predominantly $(1d^2_{5/2})_{\substack{T=1\\J=0}}$. The reaction O^{18}(t, p) has been studied by Middleton and Pullen (1964b)

who find an intense transition to the ground state of O^{20}, leading us to expect that the transition to the analog state in Ne^{20} should likewise be intense. On the other hand, the large number of highly excited levels with T = 0 and T = 1 which lie in the neighborhood of the lowest T = 2 state should be populated only weakly by the (He^3, n) reaction, since they most likely have complicated configurations which have a small overlap with $O^{18}(0.0)$ plus two closely correlated protons.

B. Experiment

The reaction $O^{18}(He^3, n)Ne^{20}$ has been studied at 11 different incident energies between 4.7 and 9.0 MeV covering excitations in Ne^{20} up to 20 MeV. Angular distributions have been taken at E_{He^3} = 5.70 and 7.33 MeV. Two different targets were employed. Initial runs and some of the width determinations were made using a target of nickel which had been oxidized some years ago by R. E. Brown in an atmosphere containing 71.7% O^{18}. The thickness of this target was not well defined or known, nor was much confidence placed in its present isotopic composition. Spectra taken with this target were dominated by the O^{16} "contaminant", which obscured the region of excitation in Ne^{20} around 16.4 MeV (due to $Ne^{18}(0.0)$) and around 18.3 MeV (due to $Ne^{18}(1.88)$). To avoid this problem the gas target of Figure 5 containing O^{18} gas with a nominal isotopic purity of 99.56% was used for most of this work. Some difficulty was experienced with outgassing of O^{16}, making it necessary to recharge the cell with fresh O^{18} gas periodically. The energy loss of protons in the 5000 Å entrance foil was determined by measuring the displacement of the 872 keV $F^{19}(p,\alpha\gamma)$ resonance. The energy loss of He^3's was then scaled by using the tables of Demirlioglu and Whaling (1962), as discussed in Section VIC.

Zero-degree time spectra taken at incident energies of 5.2, 5.7, 6.5 and 9.0 MeV are shown in Figures 43, 44, 45 and 46. The spectra are characterized by an intense continuum due to the three-body channels, $O^{16} + \alpha + n$ and $F^{19} + p + n$, which open at excitations of 4.730 and 12.844 MeV respectively. The continuum becomes much stronger as the beam energy is raised, at 9.0 MeV it nearly obscures the sharp groups at excitations between 11 and 15.5 MeV which were so prominent in the 5 MeV spectra (see Figures 43 and 46). At excitation energies in Ne^{20} greater than 15.5 MeV no pronounced structure is seen except for a single prominent group at 16.73 MeV, which we identify as the T = 2 level observed by Cerny et al., at 16.8 ± 0.1 MeV. There are indications of possible weak neutron groups corresponding to levels in Ne^{20} at excitation energies of about 17.3 and 17.6 MeV. The 17.3 MeV group can be seen in the time spectrum presented in Figure 45.

That the neutron group which we claim corresponds to the lowest T = 2 level in Ne^{20} is actually produced in the reaction $O^{18}(He^3, n)Ne^{20}$ is shown by the following checks. The measured kinematic shift in neutron energy with laboratory angle is consistent with targets between A = 16 and A = 26 as is shown in Figure 47. These limits could unfortunately not be improved in this way because the strongly forward-peaked angular distribution prevented measurements from being made at $\theta_L > 30^\circ$. Empty target runs showed no structure except for neutron groups corresponding to $O^{14}(0.0)$ and $Ne^{18}(0.0)$; therefore, the target material must be gaseous. It cannot be CO_2, N_2, N_2^{15}, O_2, Ne^{20}, or Ne^{22} since we have investigated the (He^3, n) reactions on these targets. Since the nominal purity of the gas used is 99.56%, we conclude the level is indeed in Ne^{20}.

It should be noted that there is no evidence in our data for the state at 18.5 MeV reported by Cerny et al. Such a state would appear in the spectrum of Figure 46 at the spot marked A. The "absence" of this state in our spectra is not unexpected, since in the $O^{18}(t, p)O^{20}$ reaction the maximum differential cross section of the analogous state is only 1/6 of the zero-degree cross section of the ground state.

C. Excitation Energy of the Lowest T = 2 State

The excitation energy of the lowest T = 2 state was found by comparing Q-values with the $O^{16}(He^3, n)Ne^{18}(0.0)$ transition. This reaction was chosen because it produces neutrons of nearly the same energy as the reaction of interest. This greatly reduces errors due to uncertainties in the foil thickness and calibration constant of the beam analyzing magnet. The chief disadvantage of this reaction as a calibration is the large ($\pm$ 5 keV) uncertainty in its Q-value. We therefore express our result in a manner which will permit it to be corrected should a better value for the $O^{16}(He^3, n)Ne^{18}(0.0)$ Q-value become available. [In this work, the Q-value has been taken as -3.196 MeV.]

Six separate determinations of the excitation energy of the lowest T = 2 state were performed, three with the solid target and three with the gas cell. Each target had its disadvantages. With the solid target there were no foil corrections, but the thickness of this target was not well-known. In addition, the distributions of O^{16} and O^{18} throughout the target were not necessarily the same, which could give rise to an error in the Q-value since the mean beam energy in the target might be different for the two reactions. With a

gas target these uncertainties are removed at the expense of an additional error due to the uncertainty in the foil thickness.

Two methods were used to calibrate the time scale.

1) A spectrum of $O^{18}(He^3, n)Ne^{20}$ was calibrated against another spectrum containing the $Ne^{18}(0.0)$ group with the beam energy adjusted to give neutrons of the same energy as from $Ne^{20}(T = 2)$. Systematic errors due to the time-of-flight spectrometer vanish in this case.

2) A spectrum in which both O^{16} and O^{18} were present in the target was calibrated on the $O^{16}(He^3, n)Ne^{18}(0.0)$ group. With this method errors in the resulting excitation due to uncertainties in the beam energy were reduced by a factor of 8 over Method 1. However, systematic errors in the spectrometer are not entirely cancelled. Such errors are believed to be very small in the present reaction. A spectrum from which one of the Q-value measurements was taken is shown in Figure 43.

The mean excitation obtained from the six measurements is $16.730 \pm .006$ MeV. There does not appear to be any significant difference between values obtained from the gas and solid targets. The standard deviation of the mean of six determinations is only 2.3 keV. The quoted error is largely systematic, due to the uncertainty in the $O^{16}(He^3, n)Ne^{18}(0.0)$ Q-value. The dependence of our excitation upon this Q-value is given by

$$\frac{\partial Ex(Ne^{20})}{\partial Q} = -1.0 \quad . \tag{10}$$

The calculation of excitations and of the errors are summarized in Tables XII and XIII.

D. Width of the Lowest T = 2 Level in Ne^{20}

An upper limit on the width of the lowest T = 2 level in Ne^{20} was obtained from the gas target runs by the same procedure as used for the 11.195 MeV state in F^{17}. The shape of the Ne^{20}(16.730) group in a spectrum taken at 5.204 MeV was compared with the Ne^{18}(0.0) group in a 4.798 MeV spectrum. The gas pressures were the same in both runs, and these beam energies produced neutrons of nearly the same flight times in both cases. A Breit-Wigner curve, transformed to have flight time as the independent variable, was then numerically folded into the Ne^{18}(0.0) shape. The intrinsic level width, Γ, of the Breit-Wigner expression was increased from zero until a good fit could no longer be obtained. The goodness of fit was evaluated by a chi-square test with the calculated and experimental points normalized to the same area. The curve of chi-square as a function of Γ, and the best fit, are presented in Figure 48. This method yields an upper limit of 20 keV for the width of the 16.730 MeV state.

A similar limit for the width was obtained from the solid target runs with the technique used to find the width of the 15.068 MeV state in N^{13}. The nickel oxide target was somewhat arbitrarily assumed to be 10 keV thick for these calculations.

E. Angular Distributions

Angular distributions were taken at E_{He^3} = 5.70 and 7.33 MeV. Since the neutron group from the T = 2 state rests upon an intense background due to the continuum, and possibly other states with T = 0 and T = 1, the choice of background is necessarily

somewhat arbitrary. In Figure 44 we have indicated a background subtraction typical of those used to obtain the 5.7 MeV angular distribution. At other angles similar backgrounds were chosen. The range of subjectively acceptible backgrounds for the 7.33 MeV spectra was not as great as it is in Figure 44. The angular distributions are presented in Figures 49 and 50. The error bars are due to counting statistics, a 5% uncertainty in beam integration and relative detector efficiency, and a subjective estimate of the uncertainty in the mean position of an assumed linear background. In addition to the errors denoted by the flags there is an estimated uncertainty of $\pm$ 10% in the absolute normalization. The smooth curves are DWBA calculations, with only the normalization adjusted. The computations were performed as described in Appendix B using the potentials presented in Table XV. The He^3, O^{18} potentials were obtained from studies of the elastic scattering of He^3 from F^{19} at 8.0 MeV (Matous, Herling, and Wolicki 1966). These potentials were chosen since the target nucleus and bombarding energy most closely approximate the present case. The exit channel potentials are those used in the (t, p) analysis of Glover and Jones (1966b). It is seen that the theoretical angular distributions are quite sensitive to the L-value, and that the observed angular distribution is clearly L = 0. One should note that in one-step stripping, L = 1 can only occur via impurities in the O^{18} wave function (for example two-particle - two-hole) or by placing a proton in the 1f shell.

VIII. CONCLUSION

We have used (He^3, n) reactions on T = 1/2 and T = 1 targets to identify higher isobaric spin states in several light nuclei. The (He^3, n) selection rules imposed by a double-stripping reaction mechanism have now been used to find T = 3/2 levels in B^9 (Dietrich, 1964), N^{13} and F^{17}, and T = 2 levels in Ne^{20} and Mg^{24} (Adelberger and McDonald, 1967). Because of the apparent success of identifications based upon the selection rules, and the reasonable quality of distorted wave fits to the measured angular distributions, it appears that the double-stripping process provides a good description of those (He^3, n) transitions having large cross sections.

It is interesting to speculate on the possibilities for continuing this program of (He^3, n) reactions to heavier nuclei. Two difficulties arise:

1) The Coulomb barrier increases roughly as $A^{2/3}$, necessitating higher beam energies to maintain reasonable counting rates.

2) The excitation energy of the higher T states becomes systematically lower with increasing A. (This must be true since heavy nuclei have a neutron excess).

These two effects are displayed in Figure 51, where the He^3 Coulomb barriers and excitation energies of higher T states of several nuclei are displayed. We are thus faced with having to use increasingly high beam energies to measure Q-values which are becoming less negative. Since the energy resolution of the time-of-flight spectrometer is greatest for low energy neutrons, the effective resolution will be greatly reduced.

A very promising field for further work, however, lies in studying the decays of these highly excited T = 3/2 and T = 2 levels. Particle decay modes can be investigated via elastic and inelastic scattering, and both particle and gamma-ray decays can be studied in coincidence experiments. Such experiments, which reveal important details of nuclear structure, are only beginning to be exploited in this and other laboratories.

APPENDIX A. THE PHASE STABILIZER

The phase stabilizer compensates for time-dependent variations in the injected beam energy by electronically adjusting the phase of the bunching wave form. It has two components - a phase detector and an electronic phase shifter which is driven by the detector.

The phase of the bunches arriving at the deflector is determined simply by measuring the difference in current hitting the two chopping slits. If the buncher is properly phased so that the current maxima occur just as the beam passes between the slits the currents striking the two slits should be equal. Figure 52 shows how the time-averaged difference current, i_{diff}, and the time-averaged beam current, i_{pulsed}, vary as a function of phase. As long as the fluctuations in injection energy are small enough so that the phase of the bursts is between φ_1 and φ_2, i_{diff} provides a good measure of the phase of the arriving ions. The range of phase angles over which the device stabilizes is sufficient to obviate the need for an energy regulator on the injector, and allows the beam energy to be changed without manual phase adjustment.

The phase changing circuit (Figure 53) is a variation of the impedance bridge with three back-biased silicon diodes used as a variable capacitor.

The difference current is detected by a sensitive differential amplifier similar to the one used to regulate the tandem accelerator. The output of this vacuum tube circuit when fed into the phase changing circuit is sufficient to provide a variation of about 40^{o}. A block diagram of the phase stabilizer appears in Figure 1.

It is interesting to note that the phase detection principle has other applications. Since the phase stabilized beam pulsing system was designed to avoid some very stringent requirements on energy regulation, it could just as well be used as a simple way of providing very precise energy regulation. For instance, it would be possible to use a phase detector in conjunction with a buncher and chopper separated by a long flight path to provide a means of detecting very small time-dependent variations in beam energy. The output of the phase detector could then be used, for example, to control the electrostatic potential of the target to compensate for these variations.

APPENDIX B. CALCULATION OF DWBA DOUBLE-STRIPPING CROSS SECTIONS

In this section we describe a scheme for computing DWBA double-stripping differential cross sections using the code TSALLY, (Bassel, Drisko, and Satchler 1962). Our treatment can be thought of as an approximation to the general distorted-wave double-stripping theory of Glendenning (1965). The calculations differ from a previous discussion of (He^3, n) double stripping (Henley and Wu 1964) primarily in that we use the zero range approximation and a more realistic wave function for the residual nucleus.

TSALLY computes cross sections derived from a DWBA transition amplitude for the reaction A(a, b)B

$$T = \int d\vec{r}_{aA} \int d\vec{r}_{bB}\, \Phi^{*}_{bB}(k_b, \vec{r}_{bB}) \langle bB | V | aA \rangle\, \Phi_{aA}(k_a, \vec{r}_{aA}). \qquad (11)$$

The Φ's are elastic scattering waves which satisfy

$$[\nabla^2 + k^2 - \frac{2\mu}{\hbar^2}(U(r) + V_c(r))]\ \Phi(k, r) = 0 \qquad (12)$$

where $\mu = m_1 m_2/(m_1 + m_2)$

and $V_c(r)$ is the Coulomb potential of a uniformly charged sphere of radius r_c having total charge $z_1 z_2$.

In our case the optical potential U(r) has the form

$$U(r) = -\frac{U}{e^{y} + 1} - i\frac{V}{e^{y'} + 1} \qquad (13)$$

where

$$y = \frac{r - r_u A^{1/3}}{a_u}$$

and

$$y' = \frac{r - r_v A^{1/3}}{a_v} \quad .$$

$\langle aA|\, V|\, aA\rangle$ is taken between internal states of a, A, b and B. In stripping theories we make the approximations that $a = b + x$, $B = A + x$, and $V = V_{bx}(r_{bx})$. For (He^3, n) stripping, b is a neutron, and x is a composite object, the diproton. After some simplification the matrix element becomes

$$\langle bB|\, V|\, aA\rangle = \sum_{N,n,\ell} C \int \varphi'_x(\tau)\varphi_x^{n\ell}(\tau)\, d\tau\; V_{bx}\, \psi_{bx}\, \psi_{Ax}^{NL} \quad , \tag{14}$$

where φ'_x is the relative wave function of the protons in He^3,

$\varphi_x^{n\ell}$ is the relative wave function of the diproton in the residual nucleus. n and ℓ are the radial and orbital quantum numbers of the relative motion,

ψ_{bx} is the orbital wave function describing the motion of the neutron and diproton in the He^3,

ψ_{Ax}^{NL} is the orbital wave function (with radial and orbital quantum numbers N and L) describing the motion of the diproton about the target in the final nucleus,

τ represents the internal coordinates of the diproton, and

C depends upon all the summed quantities.

The zero range approximation $V_{bx}(r_{bx})\psi_{bx}(r_{bx}) \propto \delta(r_{bx})$ leads to

$$\langle bB|\, V|\, aA\rangle \propto \sum_{N,n,\ell} C\, \psi_{Ax}^{NL}(r_{Ax})\, \delta(r_{bx}) \int \varphi_x'(\tau)\, \varphi_x^{n\ell}(\tau)\, d\tau \ . \qquad (15)$$

We further simplify this expression by demonstrating that all but one of the terms in the cross section can be neglected. The wave function of the residual nucleus, B, can be expressed as a core, A, surrounded by two nucleons in single particle shell model orbits φ_ℓ^n

$$\varphi_{J_B} = \varphi_{J_A}\, \varphi_{\ell_1}^{n_1}\, \varphi_{\ell_2}^{n_2}\, \chi_{1/2}\, \chi_{1/2} \qquad (16)$$

$\varphi_{\ell_1}^{n_1}$ and $\varphi_{\ell_2}^{n_2}$ coupled to L; $\chi_{1/2}$ and $\chi_{1/2}$ coupled to S; L and S coupled to J_x; φ_{J_A} and J_x coupled to J_B.

where the $\chi_{1/2}$ are spinors.

We are using a notation where the brackets under the wave functions imply angular momentum coupling.

This wave function, where the quantum numbers n_1, n_2, ℓ_1, and ℓ_2 are given by the shell model, can be expanded as a sum of wave functions of the type used in obtaining equation (B4), where the core is surrounded by a composite object x

$$\varphi_{J_B} = \sum_{N,n,\ell} c_{N,n,L,\ell,S}\, \varphi_{J_A}\, \psi_{Ax}^{NL'}\, \psi_x^{n\ell}\, \chi_{1/2}\, \chi_{1/2} \quad . \tag{17}$$

L ($\psi_{Ax}^{NL'}$ with $\chi_{1/2}$), S ($\chi_{1/2}\,\chi_{1/2}$); J_x (L with S); J_B (φ_{J_A} with J_x)

The general transformation between the descriptions (16) and (17) involves a six-dimensional integral and is impractical. However, if the single particle orbits φ_ℓ^n are harmonic oscillator wave functions, the transformations are soluble analytically (see for example Balashov and Eltekov 1960). N. deTakacsy (1966) has calculated the overlap integrals

$$\int \varphi_x'(\tau)\, \varphi_x^{n\ell}(\tau)\, d\tau \quad , \tag{17}$$

where φ_x' was taken from a realistic proton wave function for He^3 (Henley and Yu 1965) and the $\varphi_x^{n\ell}$ were taken from the transformations of Balashov and Eltekov. He finds that the overlap is almost entirely concentrated in the relative harmonic oscillator state with $n = 1$, $\ell = 0$. If we neglect all terms except those with

$n = 1$, $\ell = 0$, the sum reduces to a single term, and the matrix element becomes

$$\langle bB|\, V|\, aA\rangle \;\propto\; \psi_{Ax}^{NL}(r_{Ax})\;\delta(r_{bx}) \quad . \tag{19}$$

The bound state function, ψ_{Ax}, is just as important as the elastic scattering waves, Φ, in a DWBA calculation (Austern 1964). It has been pointed out that oscillator wave functions are inadequate for DWBA two-nucleon stripping, since the calculations are sensitive to the tails of the wave functions (Drisko and Rybicki 1966). We have therefore taken the N and L values given by oscillator eigenfunctions, and used these quantum numbers to calculate φ_{Ax}^{NL} from a Schrodinger equation

$$\left(\frac{\hbar^2}{2\mu_{Ax}}\nabla^2 - U(r_{Ax}) - V_c(r_{Ax}) - E_B\right)\varphi_{Ax}^{NL}(r_{Ax}) = 0, \tag{20}$$

where $\mu_{Ax} = m_A mx/(m_A + mx)$

$$U(r) = -\frac{U_o}{e^y + 1} \qquad y = \frac{r - R_o A^{1/3}}{a_o}$$

$V_c(r)$ = is the Coulomb potential of a uniformly charged sphere of radius R_c and total charge $Z_A Z_x$

E_B = is the binding energy of x and A in B.

The well depth U_o is adjusted to give the correct binding energy E_B. φ_{Ax} can be computed once m_A, m_x, $Z_A Z_x$, R_c, R_o, a_o, E_B, and the radial and orbital quantum numbers N and L are specified. L, of course, is just the transferred orbital angular momentum, and hopefully can be inferred from the shape of the angular distribution. Terms with different L are incoherent in the cross section. In our calculations we have somewhat arbitrarily taken $R_c = 1.25f$, $R_o = 1.25f$, $a_o = 0.65f$; and assumed that E_B was given by the energy required to separate two protons from the final nucleus.

Except for the optical potentials, we have specified all the quantities needed by TSALLY to perform the DWBA calculations. Very few studies of the elastic scattering of He^3 by light nuclei have been analyzed to give up-to-date optical model parameters. Most work had been done with potentials which are too shallow by modern standards. We have therefore taken some of our He^3 potentials from a recent and thorough study of 12 MeV triton scattering from several light elements by Glover and Jones (1966a). They see the usual ambiguities, finding four sets of potentials with real parts approximately 50, 100, 150 and 200 MeV deep which fit the scattering equally well. They then (Glover and Jones 1966b) tried to fit (t, p) reactions with their potentials, and found that only the 150 MeV set of potentials described both the scattering and the reaction. We have, without any modification except to the Coulomb barriers, adopted their potentials, in both the incident and outgoing channels. While fits could doubtless be considerably improved by varying the potentials (this was tried for a set of He^3 potentials with a real depth of 50 MeV) we prefer the approach of using no free

parameters except for normalization, since any deficiencies in the theory cannot be covered up by compensating adjustments in the potentials. The potentials used in our work are presented in Tables XIV and XV.

REFERENCES

Adelberger, E. G. and A. B. McDonald 1967, to be submitted to Physics Letters.

Austern, N. 1964, Nuclear Spectroscopy with Direct Reactions II. p. 1, edited by F. E. Throw, Argonne National Laboratory Report No. ANL-6878 (unpublished).

Balashov, V. V. and V. A. Eltekov 1960, Nuc. Phys. 16, 423.

Barnes, C. A., E. G. Adelberger, D. C. Hensley and A. B. McDonald 1966, Proceedings of the International Conference on Nuclear Physics, Gatlinburg, Tenn. 1966, (to be published).

Barton, R., R. McPherson, R. E. Bell, W. R. Frisken, W. T. Link and R. B. Moore 1963, Canad. Jour. Phys. 41, 2007.

Bassel, R. H., D. H. Drisko and G. R. Satchler 1962, Oak Ridge National Laboratory Report ORNL-3240 (unpublished).

Boyarkina, A. N. 1964, Akademia Nauk SSSR,English translation of the Bulletin of the Academy of Sciences of the USSR Physical Sciences 28, 255.

Brafman, H. 1965, Nuc. Inst. and Meth, 34, 239.

Broude, C., T. K. Alexander and A. E. Litherland 1963, Bull. of Am. Phys. Soc., Vol. 8, p. 26.

Bredin, D. J., O. Hansen, G. M. Temmer and R. Van Bree 1966, Isobaric Spin in Nuclear Physics p. 472, edited by John D. Fox and Donald Robson Academic Press, New York.

Brown, G. E. and A. M. Green 1966, Nuc. Phys. 75, 401.

Cerny, J., R. H. Pehl and G. T. Garvey 1964, Phys. Lett. 12, 234.

Cerny, J., R. H. Pehl, G. Butler, D. G. Fleming, C. Maples and C. Detraz 1966, Phys. Lett. 20, 35.

Demirliuglu, D. and W. Whaling 1962, unpublished.

de Takacsy, N. B. 1966, private communication.

Dietrich, Frank S. 1964, Ph. D. Thesis, California Institute of Technology (unpublished).

Dietrich, Frank S. 1965, Nuc. Phys. 69, 49.

Domingo, J. J. 1963, Ph. D. Thesis,California Institute of Technology (unpublished).

Drisko, R. M. and F. Rybicki 1966, Phys. Rev. Lett. 16, 275.

Evans, R. D. 1955, The Atomic Nucleus, p. 662, McGraw-Hill, New York.

Flerov, N. N. and E. A. Tamanov 1957, Atomnaya Energ. 3, 44, translated in Soviet J. Atomic Energy 3, 776,1957.

Gale, N. H., J. B. Garg and K. Ramavataram 1961, Nuc. Phys. 22, 500.

Garvey, G. T., J. Cerny and R. H. Pehl 1964, Phys. Rev. Lett. 12, 726.

Glendenning, Norman K. 1965, Phys. Rev. 137, B102.

Glover, R. N. and A. D. W. Jones 1966a, Nuc. Phys. 81, 268.

Glover, R. N. and A. D. W. Jones 1966b, Nuc. Phys. 81, 277.

Goldberg, M. D., J. D. Anderson, J. P. Stoering and C. Wong 1961, Phys. Rev. 122, 1510.

Goldberg, M. D. and J. M. LeBlanc 1960, Phys. Rev. 119, 1992.

Hardie, G., R. L. Dangle and L. D. Oppliger 1963, Phys. Rev. 129, 353.

Hart, Vincent P., E. Norbeck and R. R. Carlson 1965, Phys. Rev. 137, B17.

Henley, E. M. and D. U. L. Wu 1964, Phys. Rev. 133, B1445.

Hensley, D. C. and C. A. Barnes 1965, Bull. Am. Phys. Soc. 10, 1194.

Hensley, D. C. and C. A. Barnes 1966, private communication.

Krick, Merlyn and G. J. F. Legge 1966, Bull. Am. Phys. Soc. 11, 44.

Kuan, H. M. and S. S. Hanna 1966, Bull. Am. Phys. Soc. 11, 904.

Lauritsen, T. and F. Ajzenberg-Selove 1962, Nuclear Data Sheets, Sets 5 and 6, 1961 (NRC, NAS, Washington, D. C. 1962).

Litherland, A. E., R. Batchelor, A. J. Ferguson and H. E. Gove 1961, Canad. Journ. Phys. 39, 276.

Loncke, P. and J. Pradal 1966, Phys. Lett. 22, 320.

Lynch, B., G. M. Griffiths and T. Lauritsen 1965, Nuc. Phys. 65, 641.

Margolis, B. and N. deTakacsy 1966, Canad. Jour. Phys. 44, 1431.

Matous, G. M., G. H. Herling and E. A. Wolicki 1966, Phys. Rev. 152, 908.

McPherson, R., J. C. Hardy, R. E. Bell 1964, Phys. Lett. 11, 65.

McPherson, R., R. A. Esterlund, A. M. Poskanzer and P. L. Reeder 1965, Phys. Rev. 140, B1513.

Middleton, R. and D. J. Pullen 1964a, Nuc. Phys. 51, 50.

Middleton, R. and D. J. Pullen 1964b, Nuc. Phys. 51, 63.

Newns, H. C. 1960, Proc. Phys. Soc. London 76, 489.

Ollerhead, R. W., J. S. Lopes, A. R. Poletti, M. F. Thomas and E. K. Warburton 1965, Nuc. Phys. 66, 161.

Patterson, J. R., H. C. Winkler and C. S. Zaidens 1967, private communication.

Pearson, J. D. 1963, Ph. D. Thesis, California Institute of Technology, unpublished.

Satchler, G. R. 1964, Nuclear Spectroscopy with Direct Reactions II. p. 23, edited by F. E. Throw, Argonne National Laboratory Report No. ANL-6878 (unpublished).

Segel, R. E., P. P. Singh, R. G. Allas and S. S. Hanna 1963, Phys. Rev. Lett., Vol. 10, p. 345.

Silbert, M. G. and J. C. Hopkins 1964, Phys. Rev. 134, B16.

Talmi, I. and I. Unna 1960, Phys. Rev. Lett. 4, 469.

Towle, J. H. and B. E. F. Macefield 1961, Proc. Phys. Soc. London 77, 399.

Warburton, E. K., P. D. Parker and P. F. Donovan 1965, Phys. Lett. 19, 397.

Wilkinson, D. H. 1964, Phys. Rev. Lett. 13, 571.

Wilson, W. E., R. L. Walter and D. B. Fossan 1961, Nuc. Phys. 27, 421.

Winkler, H. 1966, private communication.

Zeidman, B. and T. H. Braid 1965, Phys. Lett. 16, 139.

TABLE I

Sample Calculation of Ne^{18} Q-Values
(see page 29)

I. Calculation of Incident Energies

ion	Nominal Energy (MeV)	Corrections (MeV) due to target thickness[a]	Calib. Const.[b]	Corrected Energy (MeV)
p	3.840	- .004	+ .004	3.840
p	4.200	- .004	+ .004	4.200
He^3	9.900	- .020	+ .010	9.890
He^3	10.850	- .019	+ .011	10.842

II. Calculation of Q-Value of 4.55 MeV State Using $B^{11}(p, n)$ as Calibration

E_1(MeV)	$X_{n-\gamma}$(ch)	Q(MeV)	
3.840	120.5	-2.7632	
9.890	116.3	?	? = -7.739 MeV

III. Calculation of Q-Value of 5.14 MeV State Using $B^{11}(p, n)$ as Calibration

E_1(MeV)	$X_{n-\gamma}$(ch)	Q(MeV)	
4.200	101.1	-2.7632	
10.842	102.4	?	? = 8.339 MeV

a. the mean energy loss in the target was taken to be 1/2 δE where δE is the total energy loss.

b. taken to be +1 keV/MeV (Winkler 1966).

TABLE II

(see page 29)

I. Errors in Excitation of 4.55 MeV State of Ne^{18}

	Uncertainty	Resulting Error in E_x (keV)
E_1[a] (calib)	± 5.8 keV	3.5
E_1[a] (data)	± 15 keV	13
$X_{n-\gamma}$ (calib)	± 0.2 ch	3
$X_{n-\gamma}$ (data)	± 0.6 ch	8
	Total	16.0 keV

II. Errors in Excitation of 5.14 MeV State of Ne^{18}

	Uncertainty	Resulting Error in E_x (keV)
E_1[a] (calib)	± 6.3 keV	5
E_1[a] (data)	± 16 keV	13
$X_{n-\gamma}$ (calib)	± 0.2 ch	4
$X_{n-\gamma}$ (data)	± 0.7 ch	13
	Total	19.5 keV

a. taken to be 1/2 of theoretical maximum allowed by slits
(see page 30)

TABLE III

Sample Calculation of the Excitation Energy of the 15.068 MeV State in N^{13}

(see page 45)

I. Calculation of Incident Energies

q ion	Nominal Energy (MeV)	Corrections (MeV) due to target thickness[a]	calib. const.[b]	Corrected Energy (MeV)
p	4.000	- .004	+ .004	4.000
He^3	7.001	- .024	+ .007	6.984

II. Calculation of Q-Values Using $B^{11}(p, n)$ as Calibration

E_1(MeV)	$X_{n-\gamma}$ (ch)	Q (MeV)	
4.000	143.7	-2.7632	
6.984	143.6	?	? = -4.878

corresponds to E_x = 15.061 MeV

a. the mean energy loss was assumed to be 1/2 δE where δE is the total energy loss.

b. taken to be + 1 keV/MeV (Winkler, 1966).

TABLE IV

Sample Calculation of Errors in the Excitation Energy of the 15.068 MeV State in N^{13}

(see page 45)

	Uncertainty	Resulting Error in E_x (keV)
E_1[a] (calib)	8.8 keV	7
E_1[a] (data)	15.3 keV	12
$X_{n-\gamma}$ (calib)	0.2 ch	2.4
$X_{n-\gamma}$ (data)	0.2 ch	2.4
	Total	± 14.5 keV

a. taken to be 1/2 of the theoretical maximum allowed by the slits (see page 30)

TABLE V

Mean Excitation Energy of 15.068 MeV State in N^{13}

(see page 45)

Individual Determinations of E_x (MeV)

15.075
15.067
15.075
15.069
15.059
15.061

Mean = 15.068 MeV

S.D. of Individual Determinations = .007 MeV

S.D. of Mean = .0029 MeV

TABLE VI

Excitation Energy of the 18.98 MeV State in N^{13}

(see page 46)

I. Calculation of Incident Energies

ion	Nominal Energy (MeV)	Corrections (MeV) due to target thickness[a]	calib. const.[b]	Corrected Energy (MeV)
p	4.800	- .002	+ .005	4.803
He^3	12.504	- .010	+ .013	12.507

II. Calculation of Q-Value Using $B^{11}(p, n)$ as Calibration

E_1 (MeV)	$X_{n-\gamma}$ (ch)	Q (MeV)	
4.803	135.8	-2.7632	
12.507	135.9	?	? = -8.802

corresponds to E_x = 18.985 MeV

a. the mean energy loss in the target was taken to be 1/2 δE where δE is the total energy loss.

b. taken to be +1 keV/MeV (Winkler 1966).

TABLE VII

Calculation of Errors in the Excitation Energy of the 18.98 MeV State in N^{13}

(see page 46)

	Uncertainty	Resulting Error in E_x (keV)
E_1[a] (calib)	10.6 keV	8
E_1[a] (data)	27.5 keV	22.6
$X_{n-\gamma}$ (calib)	0.1 ch	2
$X_{n-\gamma}$ (data)	0.5 ch	10
	Total	± 26 keV

a. taken to be 1/2 of the theoretical maximum allowed by the slits (see page 30)

TABLE VIII

Excitation Energy of 11.195 MeV State in F^{17}
(see page 58)

I. Calculation of Incident Energies

ion	Nominal Energy (MeV)	Corrections (MeV) due to foil	gas	calib. const. [c]	Corrected Energy (MeV)
He^3	8.401	-0.163[a]	-0.007	+0.008	8.239
α	7.100	-0.214[a]	-0.008	+0.007	6.885
He^3	8.400	-0.144[b]	-0.008	+0.008	8.256
α	9.080	-0.164[b]	-0.010	+0.009	8.915

II. Calculation of Q-Values

A. Using $N^{14}(\alpha, n)F^{17}$(0.0 as Calibration

E_1(MeV)	$X_{n-\gamma}$(ch)	Q (MeV)	
6.885	147.6	-4.7349	
8.239	145.8	?	? = -6.192 ± 0.010 MeV

B. Using $N^{15}(\alpha, n)F^{18}$(0.0) as Calibration

E_1(MeV)	$X_{n-\gamma}$(ch)	Q (MeV)	
8.915	156.4	-6.4187	
8.256	155.6	?	? = -6.182 ± 0.011 MeV

C. Final Value

$Q = -6.187 \pm .007$ MeV or $E_x = 11.195 \pm .007$ MeV

a. foil #1 b. foil #2 c. assumed to be +1 keV/MeV (Winkler 1966).

TABLE IX

Errors in Excitation Energy of 11.195 MeV State in F^{17}
(see page 58)

I. Using $N^{14}(\alpha, n)F^{17}(0.0)$ as Calibration

	Uncertainty	Resulting Error in E_x(keV)
E_1[a] (calib)	6.9 keV	6.0
E_1[a] (data)	8.2 keV	7.0
$X_{n-\gamma}$ (calib)	0.2 ch	2.4
$X_{n-\gamma}$ (data)	0.2 ch	2.4
Q (calib)	0.7 keV	0.7
	Total	10

II. Using $N^{15}(\alpha, n)F^{17}(0.0)$ as Calibration

	Uncertainty	Resulting Error in E_x(keV)
E_1[a] (calib)	8.9 keV	7.5
E_1[a] (data)	8.3 keV	7.2
$X_{n-\gamma}$ (calib)	0.2 ch	2.2
$X_{n-\gamma}$ (data)	0.2 ch	2.2
Q (calib)	1.2 keV	1.2
	Total	11

a. taken to be 1/3 of theoretical maximum allowed by the slits (see Pearson 1963).

TABLE X

Excitation Energy of 12.540 MeV State in F^{17}

(see page 58)

I. Calculation of Incident Energies

ion	Nominal Energy (MeV)	Corrections (MeV) due to foil[a]	gas	calib. const.[b]	Corrected Energy (MeV)
He^3	10.240	-0.127	-0.007	+.010	10.116
He^3	10.180	-0.127	-0.007	+.010	10.056
α	9.080	-0.164	-0.010	+.009	8.915

II. Calculation of Q-Values Using $N^{15}(\alpha, n)F^{18}(0.0)$ as Calibration

E_1(MeV)	$X_{n-\gamma}$(ch)	Q(MeV)	
8.915	156.4	-6.4187	
10.056	140.8	?	? = -7.532 ± .013 MeV
10.116	137.2	?	? = -7.525 ± .013 MeV

III. Q-Value Obtained Using 150 ns Delay Cable as Calibration

? = -7.540 ± .016 MeV

IV. Final Q-Value

Q = -7.532 ± .010 corresponds to E_x = 12.540 ± .010 MeV

a. foil #2

b. assumed to be +1 keV/MeV (Winkler 1966)

TABLE XI

Excitation Energy of 13.059 MeV State in F^{17}

(see page 58)

I. Calculation of Incident Energies

ion	Nominal Energy (MeV)	Corrections (MeV) due to foil[a]	gas	calib. const.[b]	Corrected Energy (MeV)
He^3	10.620	-0.121	-0.007	+.011	10.503
He^3	10.560	-0.121	-0.007	+.011	10.443
α	9.080	-0.164	-0.010	+.009	8.915

II. Calculation of Q-Values Using $N^{15}(\alpha, n)F^{18}(0.0)$ as Calibration

E_1(MeV)	$X_{n-\gamma}$(ch)	Q(MeV)	
8.915	156.4	-6.4187	
10.443	155.1	?	? = -8.053 ± .012 MeV
10.503	150.4	?	? = -8.047 ± .012 MeV

III. Q-Value Obtained Using 150 ns Delay Cable as Calibration

$$Q = -8.056 \pm .016 \text{ MeV}$$

IV. Final Q-Value

$$Q = -8.051 \pm .009 \text{ MeV} \quad \text{corresponds to } E_x = 13.059 \pm .009 \text{ MeV}$$

a. foil #2

b. assumed to be +1 keV/MeV (Winkler 1966).

TABLE XII

Calculation of Excitation Energy of the 16.730 MeV State in Ne^{20}

(see page 69)

I. Sample Calculation of Incident Energies

ion	Nominal Energy (MeV)	Corrections (MeV) due to foil	gas[a]	calib. const.[b]	Corrected Energy (MeV)
He^3	5.000	-.190	-.018	+.005	4.797
He^3	5.400	-.182	-.017	+.005	5.206

II. Sample Calculation of Q-Value Using $O^{16}(He^3, n)Ne^{18}(0.0)$ as Calibration

E_1(MeV)	$X_{n-\gamma}$(ch)	Q(MeV)	
4.797	151.1	-3.196	
5.206	151.2	?	? = -3.616 ± .0

III. Summary of Excitation Energies

A. Solid Target

16.728 ± .006
16.731 ± .012
16.719 ± .012

B. Gas Target

16.730 ± .011
16.733 ± .005
16.733 ± .011

C. Mean Value = 16.730

D. Standard Deviation of Individual Runs About Mean = 5 keV.

a. taken to be 1/2 of total energy loss

b. taken to be +1 keV/MeV (Winkler 1966)

TABLE XIII

Sample Calculation of Errors in the Excitation Energy of 16.730 MeV State in Ne^{20}

(see page 69)

	Uncertainty	Resulting Error in E_x(keV)
E_1[a] (calib)	7.5 keV	6.6
E_1[a] (data)	8.1 keV	7.1
$X_{n-\gamma}$ (calib)	0.2 ch	2.6
$X_{n-\gamma}$ (data)	0.2 ch	2.6
Q (calib)	5 keV	5
	Total	11.5 keV

a. taken to be 1/2 of theoretical maximum allowed by the slits (see page

TABLE XIV

Distorted wave potentials taken from an analysis of the $O^{16}(t, p)$ reaction (Glover and Jones 1966b). For the analytic form of the optical potentials see Appendix B. The incoming potentials were derived from the elastic scattering of 12 MeV tritons from O^{16}. These parameters were used without modification to fit angular distributions from the reactions $O^{16}(He^3, n)$ and $N^{15}(He^3, n)$. See pages 34 and 61.

I. Incoming Channel

U	V	r_c	r_u	r_v	a_u	a_v
146.8 MeV	18.9 MeV	1.25f	1.40f	1.40f	0.55f	0.55f

II. Outgoing Channel

U	V	r_c	r_u	r_v	a_u	a_v
54.4 MeV	20.0 MeV	1.25f	1.20f	1.20f	0.51f	0.30f

TABLE XV

Distorted wave potentials used in the analysis of an angular distribution of neutrons from the $O^{18}(He^3, n)$ reaction at 7.33 MeV incident energy. The incoming potentials were derived from the elastic scattering of 8.0 MeV He^3 from F^{19} (Matous, Herling, and Wolicki 1967). The outgoing potentials were taken from an analysis of the (t, p) reaction on several light nuclei (Glover and Jones 1966b). See page 71.

I. Incoming Channel

U	V	r_c	r_u	r_v	a_u	a_v
183.31 MeV	23.23 MeV	1.25f	1.05f	1.81f	0.829f	0.592f

II. Outgoing Channel

U	V	r_c	r_u	r_v	a_u	a_v
54.4 MeV	20.0 MeV	1.25f	1.20f	1.20f	0.51f	0.30f

Figure 1

Schematic diagram of the beam-pulsing system for the CIT/ONR tandem accelerator. The items enclosed within the dotted line are located in the control room. The chopping slits are used to define the beam burst duration and are usually set at $\pm$ .125". For simplicity the chopping slits are drawn as if they were horizontal. In practice the beam is swept vertically to avoid interfering with the energy regulation of the tandem accelerator. The beam pulsing system is discussed on page 7 and the phase stabilizer on page 74.

BEAM PULSING SYSTEM FOR CIT/ONR TANDEM

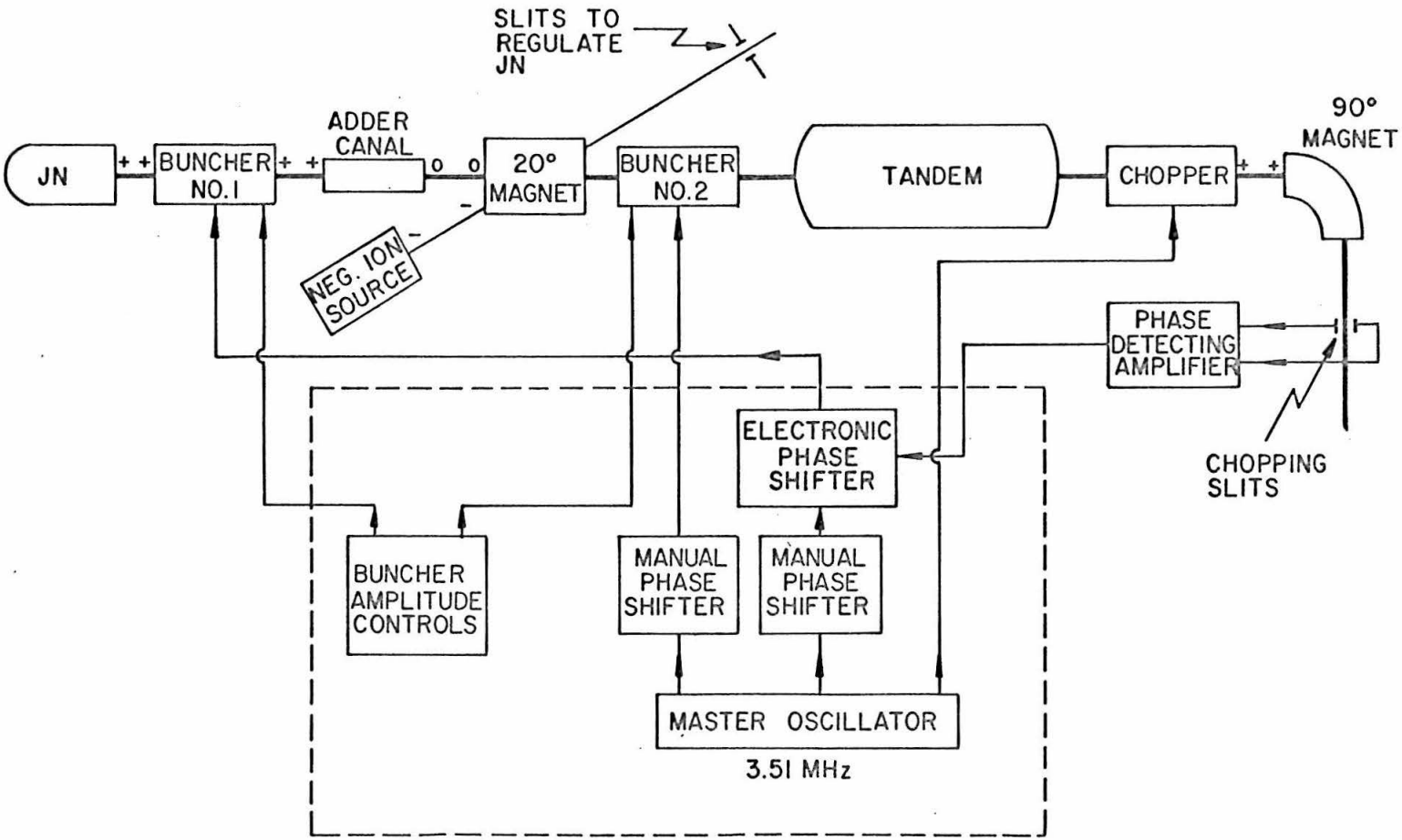

Figure 2

The experimental line shape for 1 MeV neutrons as produced by the $B^{11}(p, n)C^{11}$ reaction. The smooth curve is a computed resolution function which includes effects due to finite scintillator thickness, energy losses in the target, electronic resolving time, and beam burst duration. The "tail" on the low energy side of the neutron group is due to the collimator and shielding. It, of course, is not reproduced by the computed resolution function. (see pages 23 and 47).

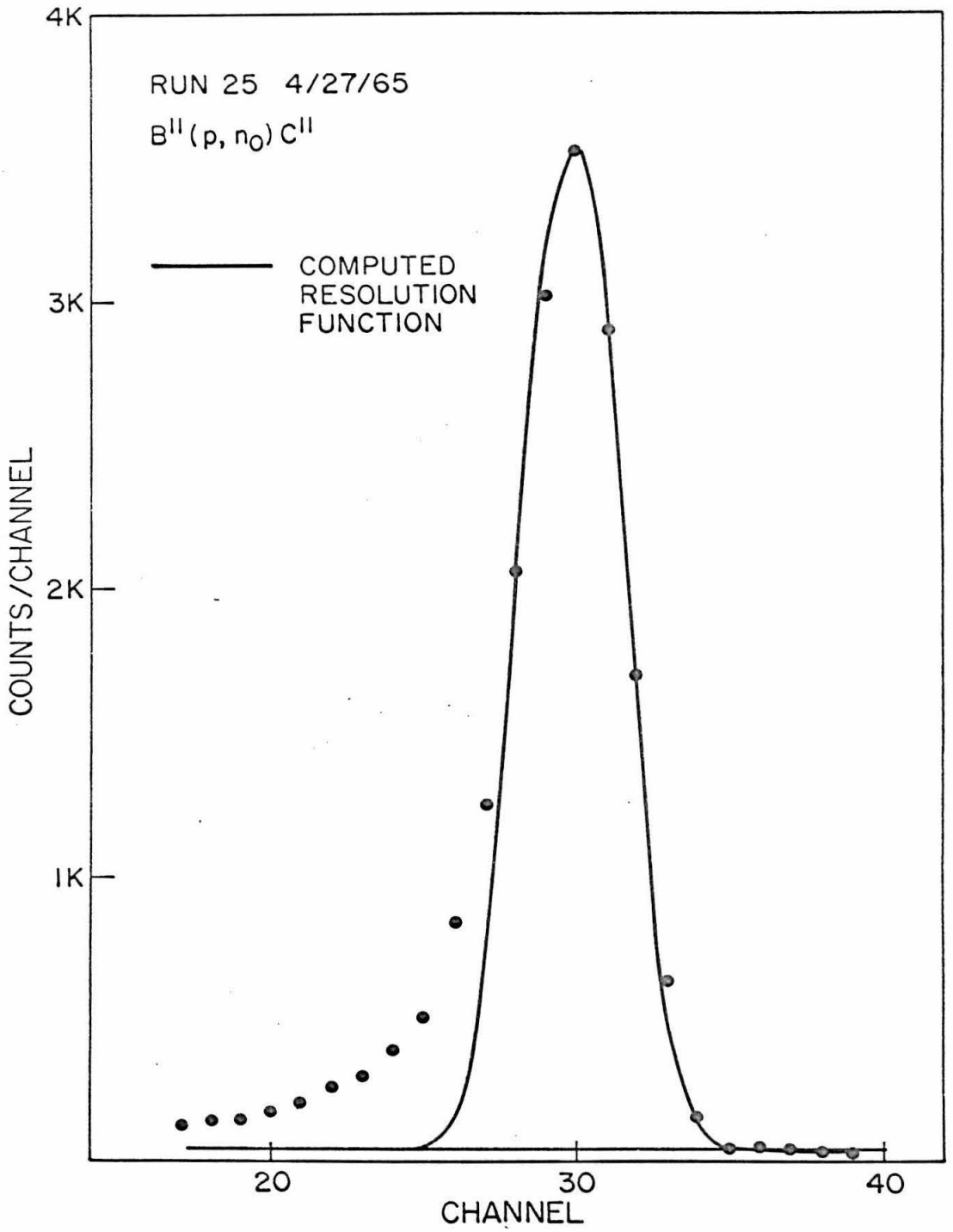
4K
3K
2K
1K
RUN 25 4/27/65
$B^{11}(p, n_0)C^{11}$
COMPUTED
RESOLUTION
FUNCTION
COUNTS/CHANNEL
20
30
40
CHANNEL

Figure 3

Block diagram of the electronic circuitry directly associated with the measurement of flight times. The commercially available instruments symbolized by the boxes are:

1) zero crossing discriminator - Tektronix Type 661 Sampling Oscilloscope.
2) time-to-pulse height converter - Ortec Model 263.
3) amplifier - Tennelec Model TC200.
4) amplifier-discriminator - Hamner Model N328.
5) fast amp #1 - Hewlett-Packard Model 460BR.
6) fast amp #2 - Nanosecond Systems Model 281.
7) fast discriminator - Nanosecond Systems Model 205FG.
8) multi-channel analyzer - RIDL 400-channel.

The circuitry is discussed on page 14.

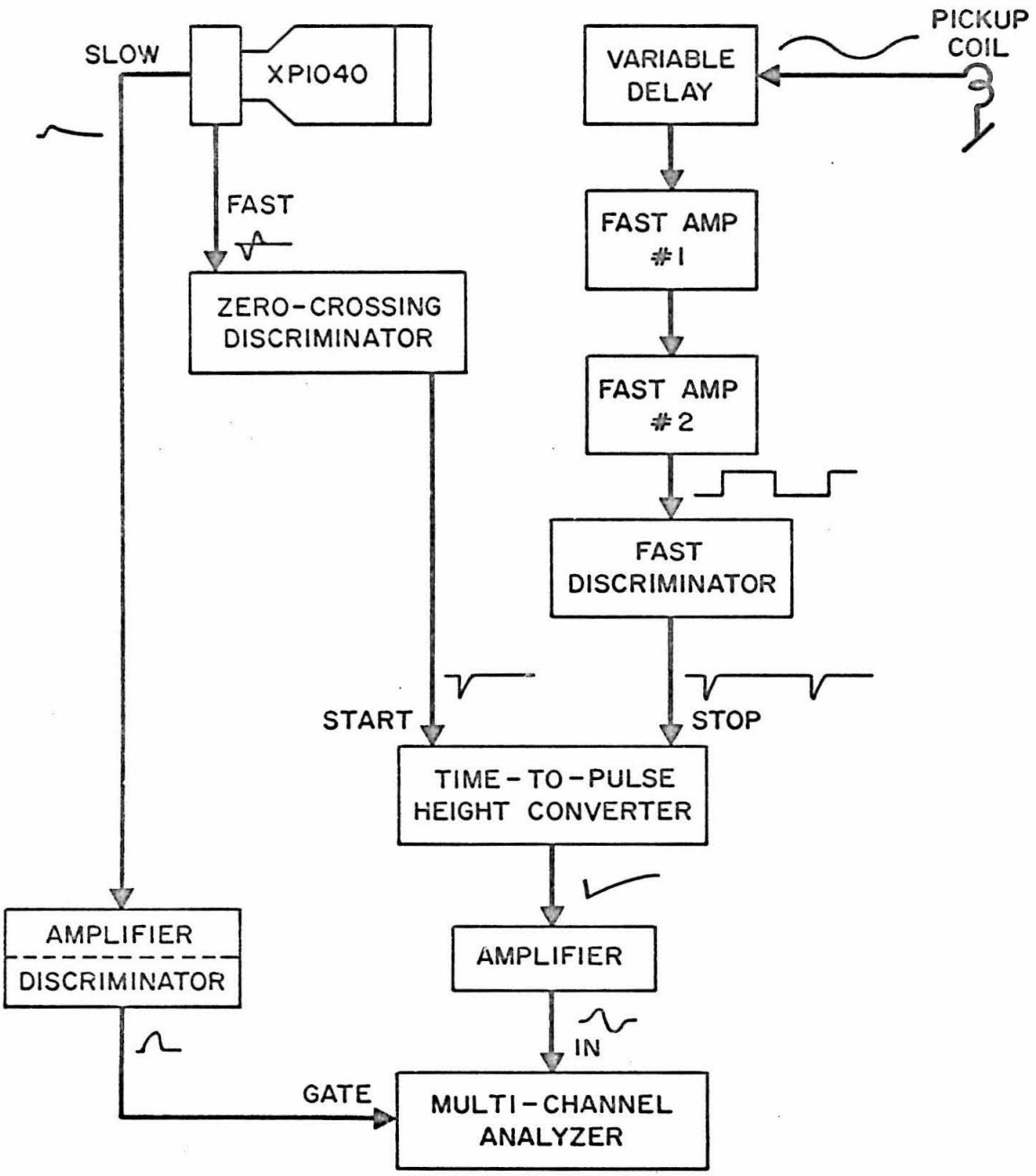
SLOW
XP1040
FAST
ZERO-CROSSING DISCRIMINATOR
VARIABLE DELAY
PICKUP COIL
FAST AMP #1
FAST AMP #2
FAST DISCRIMINATOR
START
STOP
TIME-TO-PULSE HEIGHT CONVERTER
AMPLIFIER
AMPLIFIER
DISCRIMINATOR
IN
GATE
MULTI-CHANNEL ANALYZER

Figure 4

Block diagram of γ-γ coincidence apparatus used to test the performance of the counter and fast electronic circuitry. Na^{22} was used as a source of coincident 511 keV gamma rays. The source was viewed by two scintillation counters both using XP1040 tubes. The phototube, scintillator and fast electronics in one channel were those used in the time-of-flight work. The other channel used similar apparatus. The measurement of resolving time is discussed on page 15.

γ-γ COINCIDENCE APPARATUS

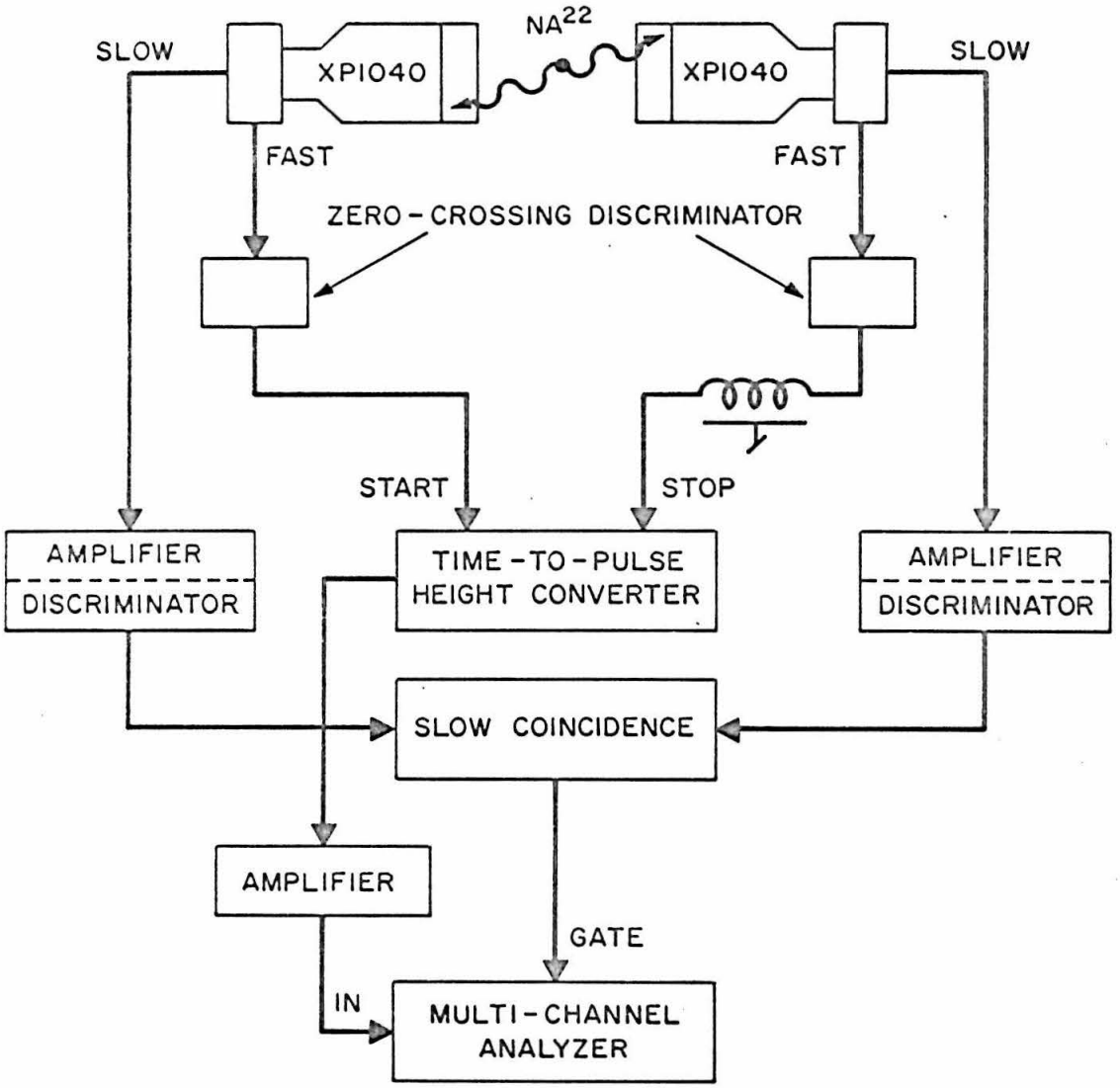

Figure 5

The gas target cell and filling system. Beam ions enter from the left and pass through a collimator, suppressor electrode, and 5000 Å nickel entrance foil before reaching the gas. The drawing is to scale. The collimator restricts the beam to a diameter of 3/8", and the gas cell is 1.54 cm long. (see pages 16, 27, 55, and 66).

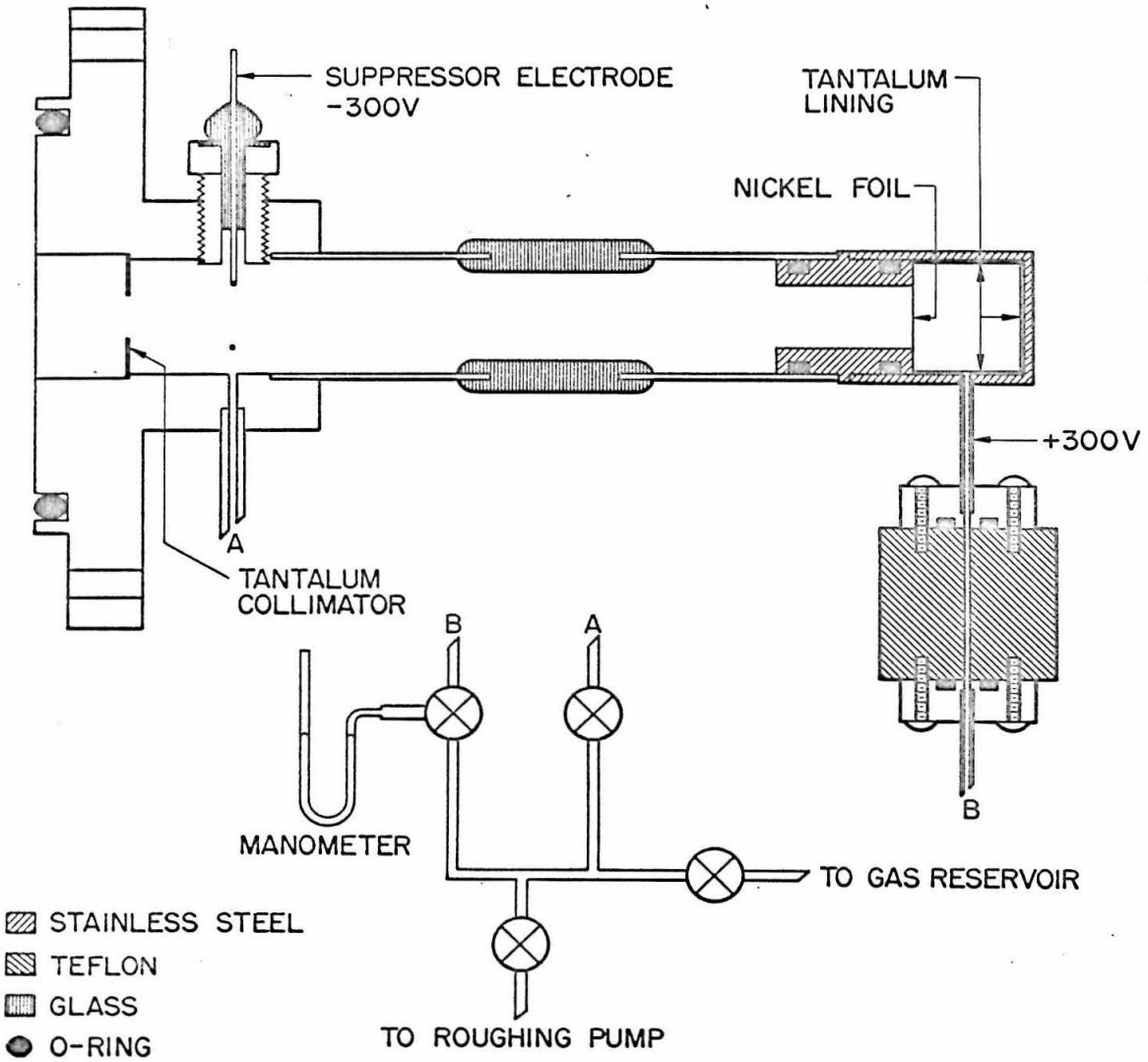
SUPPRESSOR ELECTRODE
-300V
TANTALUM
LINING
NICKEL FOIL
+300V
A
TANTALUM
COLLIMATOR
B
A
MANOMETER
TO GAS RESERVOIR
B
TO ROUGHING PUMP
STAINLESS STEEL
TEFLON
GLASS
O-RING

Figure 6

A linearity spectrum used in establishing the time scale. The time converter was started by radiation from a Cs^{137} source and stopped by RF clock pulses. The time intervals are therefore random and would produce a flat spectrum if the time scale were truly linear. The data analysis program uses such spectra to correct for any non-linearities in the time scale. (see page 18). Note that the nonlinearity in channels 180 through 199, is well outside the $\pm$ 0.3% statistics. This nonlinearity is not in the multichannel analyzer.

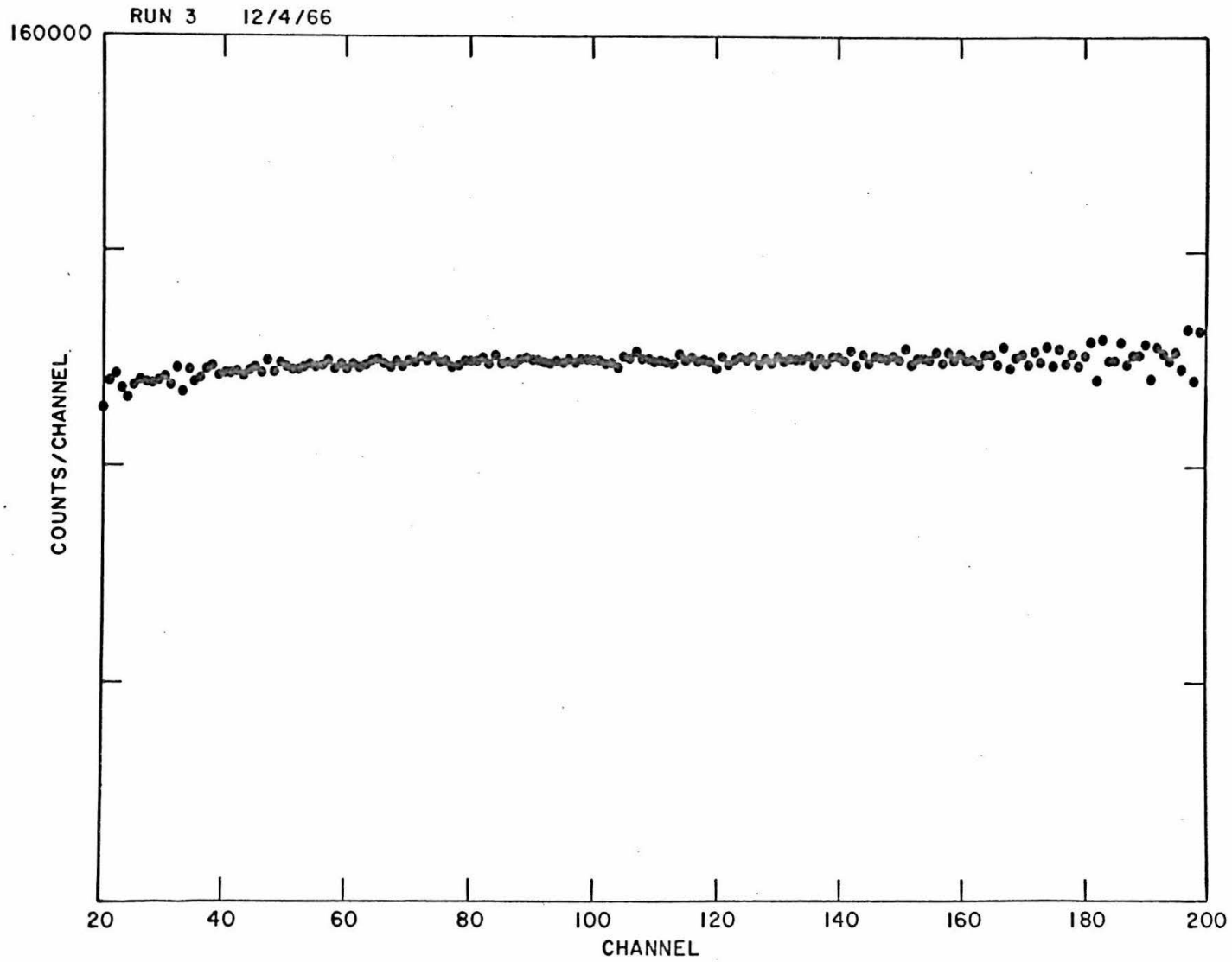
RUN 3 12/4/66
160000
COUNTS/CHANNEL
20
40
60
80
100
120
140
160
180
200
CHANNEL

Figure 7

Relative efficiency of the neutron detector. The smooth curve is computed by neglecting multiple scattering, scattering from carbon, and scattering and absorption in the shield and collimator. The curve is computed by assuming that the side channel discriminator bias is set at 450 keV proton energy. (see discussion on page 21).

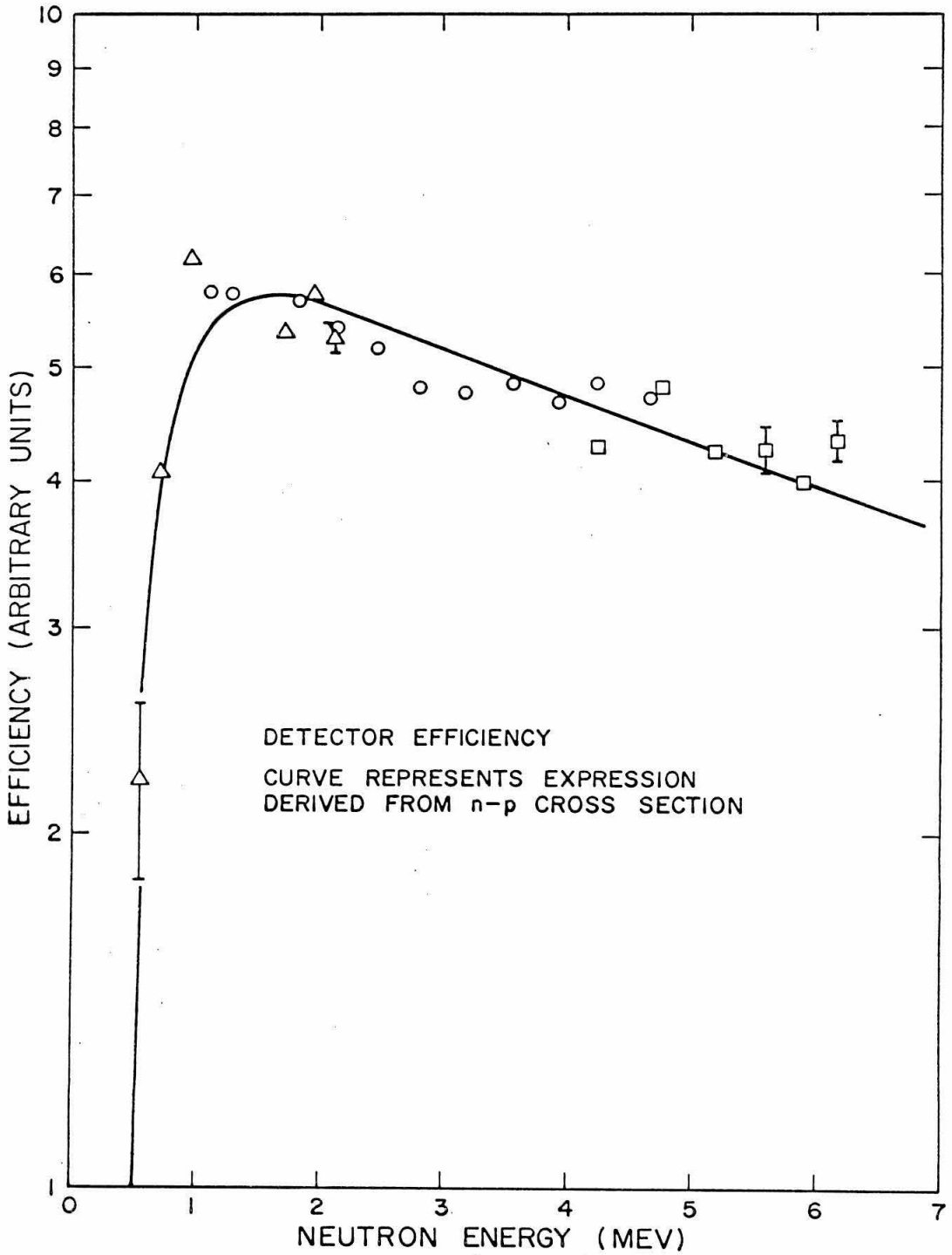
EFFICIENCY (ARBITRARY UNITS)
NEUTRON ENERGY (MEV)
DETECTOR EFFICIENCY
CURVE REPRESENTS EXPRESSION
DERIVED FROM n-p CROSS SECTION

Figure 8

Neutron time spectrum from the reaction $O^{16}(He^3, n)Ne^{18}$ at 9.0 MeV incident energy. The intense peak at the extreme right is caused by prompt gamma rays. The lines under the peaks indicate the mean background subtraction used in obtaining the angular distributions displayed in Figure 13. The two lines under the $Ne^{18}(1.88)$ peak indicate the range of mean backgrounds. This contributes to the errors computed in the differential cross sections. The background is due primarily to phototube noise and room radiation (mostly from β^+ decays). See pages 27 and 31 . The time scale is approximately one ns/ch.

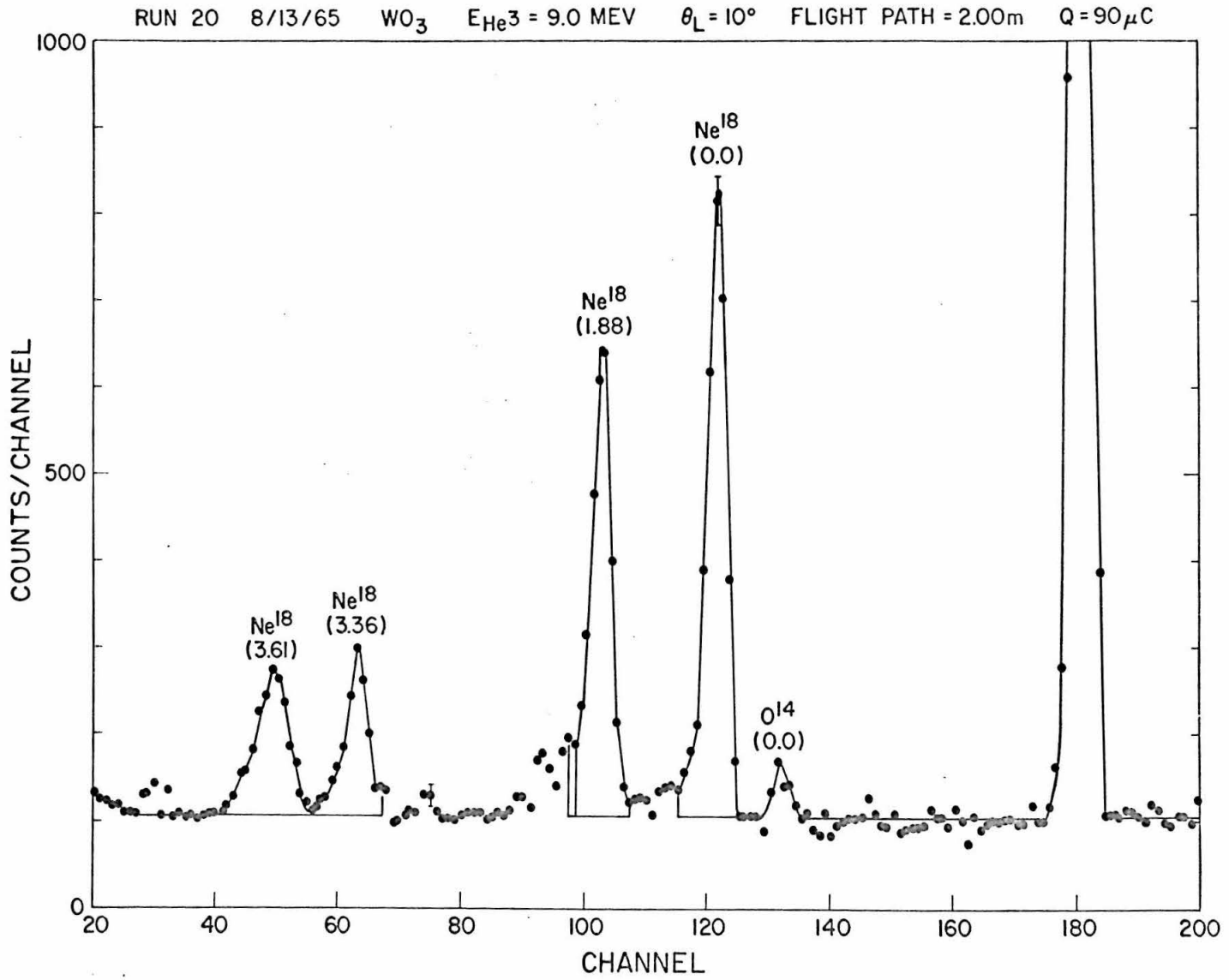
RUN 20 8/13/65 WO_3 E_{He3} = 9.0 MEV θ_L = 10° FLIGHT PATH = 2.00m Q = 90μC
COUNTS/CHANNEL
CHANNEL
0
500
1000
20
40
60
80
100
120
140
160
180
200
Ne^{18} (3.61)
Ne^{18} (3.36)
Ne^{18} (1.88)
Ne^{18} (0.0)
O^{14} (0.0)

Figure 9

Time spectrum from the $O^{16}(He^3, n)Ne^{18}$ reaction at 12.52 MeV incident energy. The intense peak to the extreme right is due to prompt gamma rays; the small peak to the left marked γ is due to prompt gamma rays from the out-of-phase beam burst. The lines under the peaks indicate the background subtraction used in obtaining the angular distributions presented in Figure 15. In addition to the time independent background, at excitations in Ne^{18} above 3.92 MeV there is a weak continuum from multibody decays. See pages 27 and 34. The time scale is approximately 1 ns/ch.

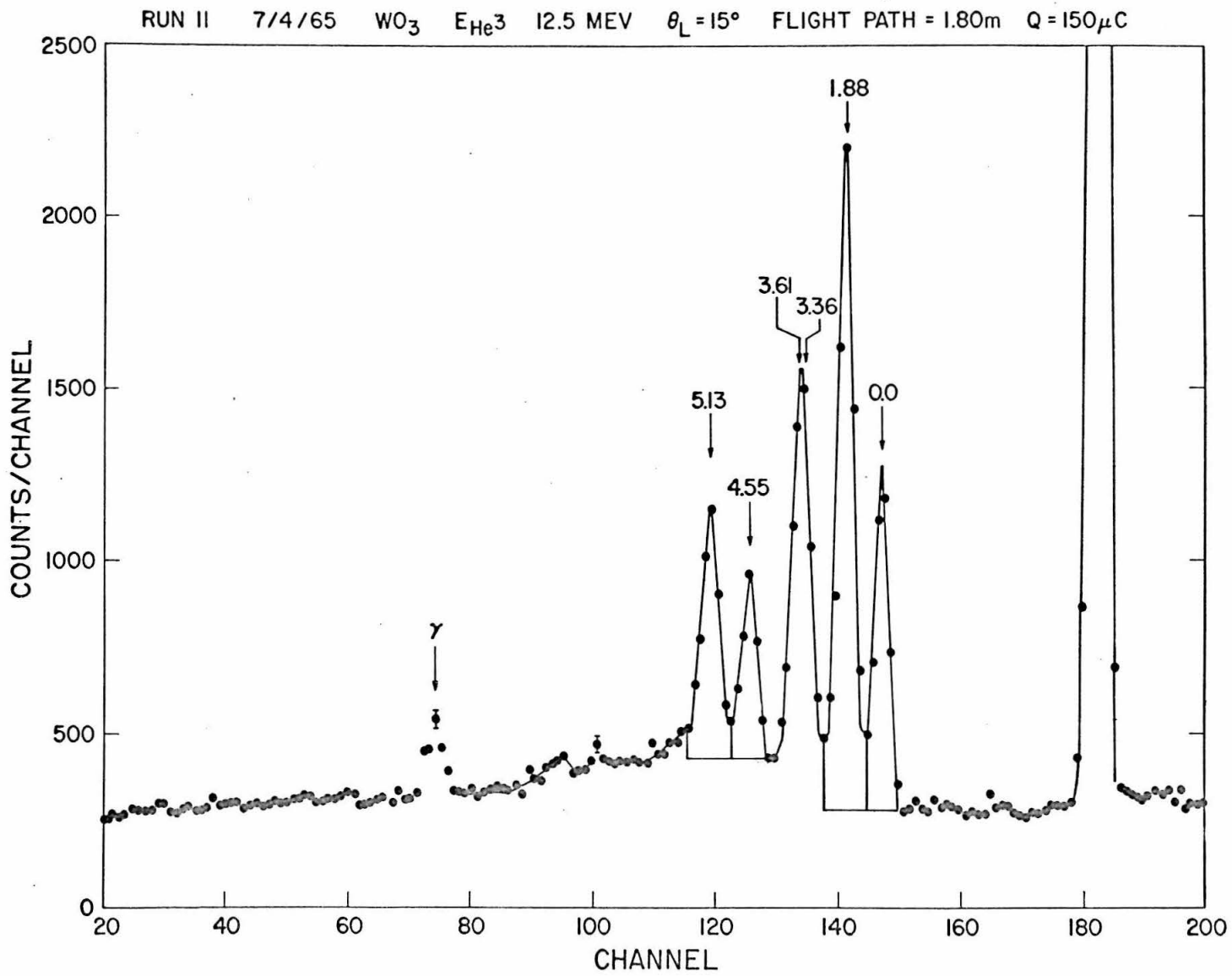
RUN II 7/4/65 WO_3 E_{He^3} 12.5 MEV θ_L = 15° FLIGHT PATH = 1.80m Q = 150μC
COUNTS/CHANNEL
CHANNEL
0
500
1000
1500
2000
2500
20
40
60
80
100
120
140
160
180
200
γ
5.13
4.55
3.61
3.36
1.88
0.0

Figure 10

Time spectrum from the $O^{16}(He^3, n)Ne^{18}$ reaction at 13.53 MeV incident energy. The peak to the left indicated by γ is due to prompt gamma rays from the out-of-phase beam burst. See page 27. The time scale is approximately 1 ns/ch.

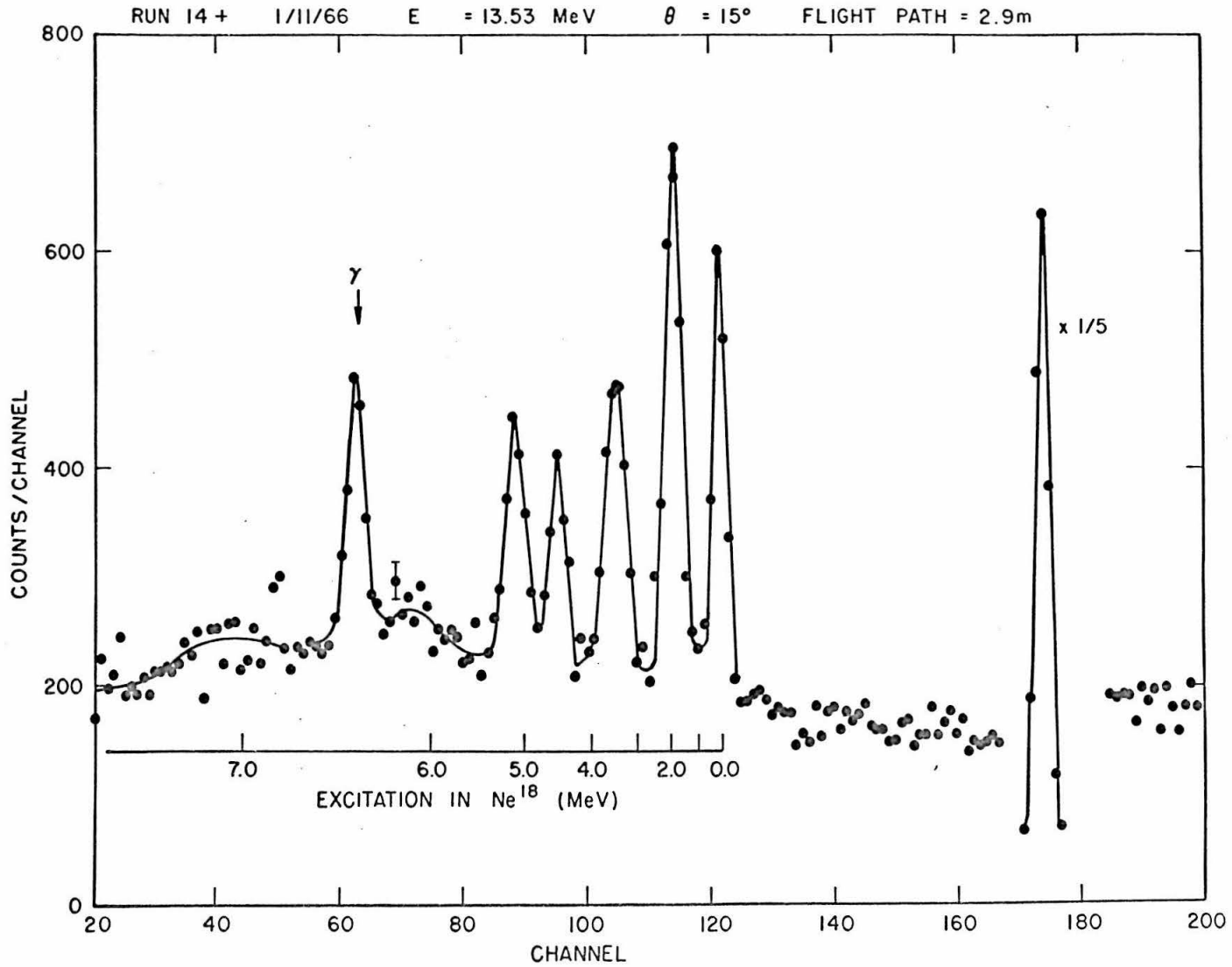
RUN 14 + 1/11/66 E = 13.53 MeV θ = 15° FLIGHT PATH = 2.9m
800
600
400
200
0
COUNTS / CHANNEL
γ
x 1/5
7.0
6.0
5.0
4.0
2.0
0.0
EXCITATION IN Ne18 (MeV)
20
40
60
80
100
120
140
160
180
200
CHANNEL

Figure 11

Demonstration that previously unobserved neutron groups correspond to levels in Ne^{18}. The measured Q-value for the (He^3, n) reaction at laboratory angles between 0^o and 150^o is plotted versus laboratory angle. The data were taken at an incident energy of 12.5 MeV. Q-values were computed assuming targets of N^{14}, O^{16}, O^{17}, and O^{18}. The best fits to a single Q-value for both the 4.55 MeV state (plotted on the left) and for the 5.14 MeV state (plotted on the right) are obtained with an O^{16} target. (See page 28.) The error bars are derived from estimates of the energy uncertainty and are not statistical. Hence the quantity "chi-square", while a measure of relative goodness of fit, has no interpretation in terms of probabilities.

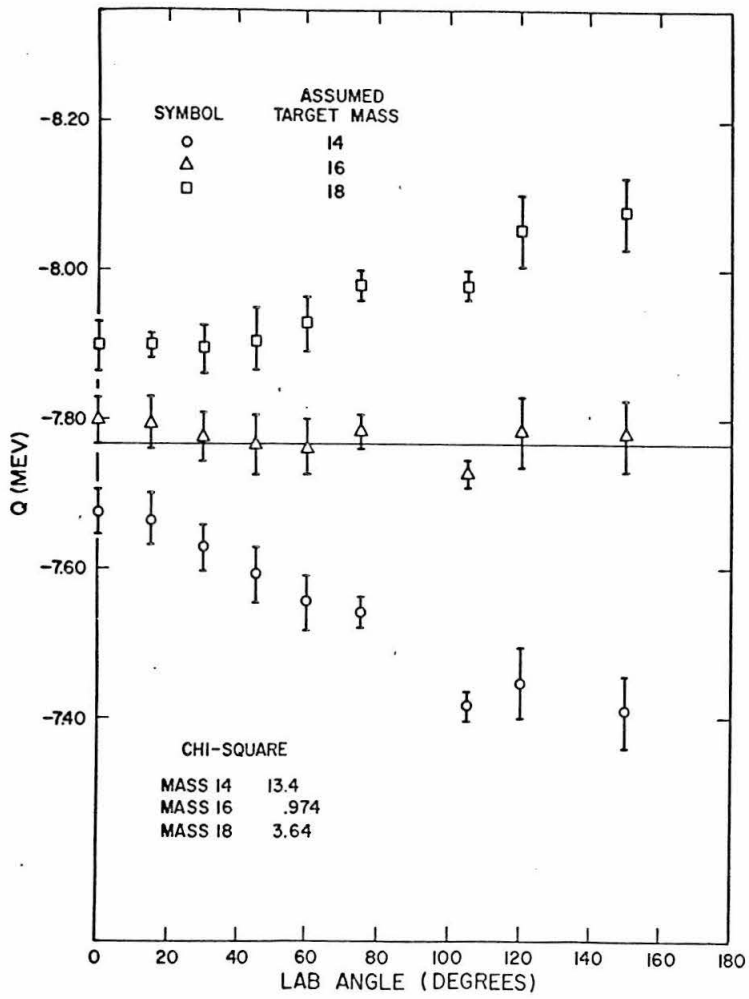
SYMBOL
ASSUMED TARGET MASS
14
16
18
-8.20
-8.00
-7.80
-7.60
-7.40
Q (MEV)
CHI-SQUARE
MASS 14 13.4
MASS 16 .974
MASS 18 3.64
0 20 40 60 80 100 120 140 160 180
LAB ANGLE (DEGREES)

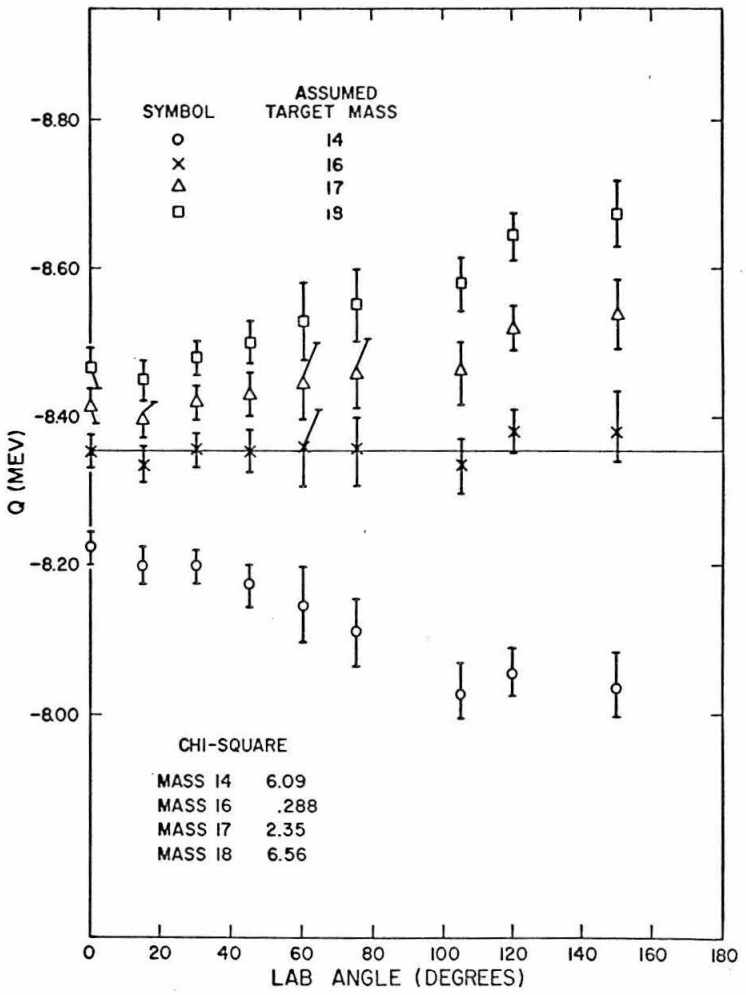
SYMBOL
ASSUMED TARGET MASS
14
16
17
18
-8.80
-8.60
-8.40
-8.20
-8.00
Q (MEV)
CHI-SQUARE
MASS 14 6.09
MASS 16 .288
MASS 17 2.35
MASS 18 6.56
0 20 40 60 80 100 120 140 160 180
LAB ANGLE (DEGREES)

Figure 12

Time spectrum used in a measurement of the Q-value of the $O^{16}(He^3, n)Ne^{18}$ (4.55) reaction. The time scale is about 1 ns/ch and was calibrated using the $B^{11}(p, n)C^{11}(0.0)$ reaction. Note that the 1.88 MeV state is very weakly populated in this spectrum. (see pages 30 and 35).

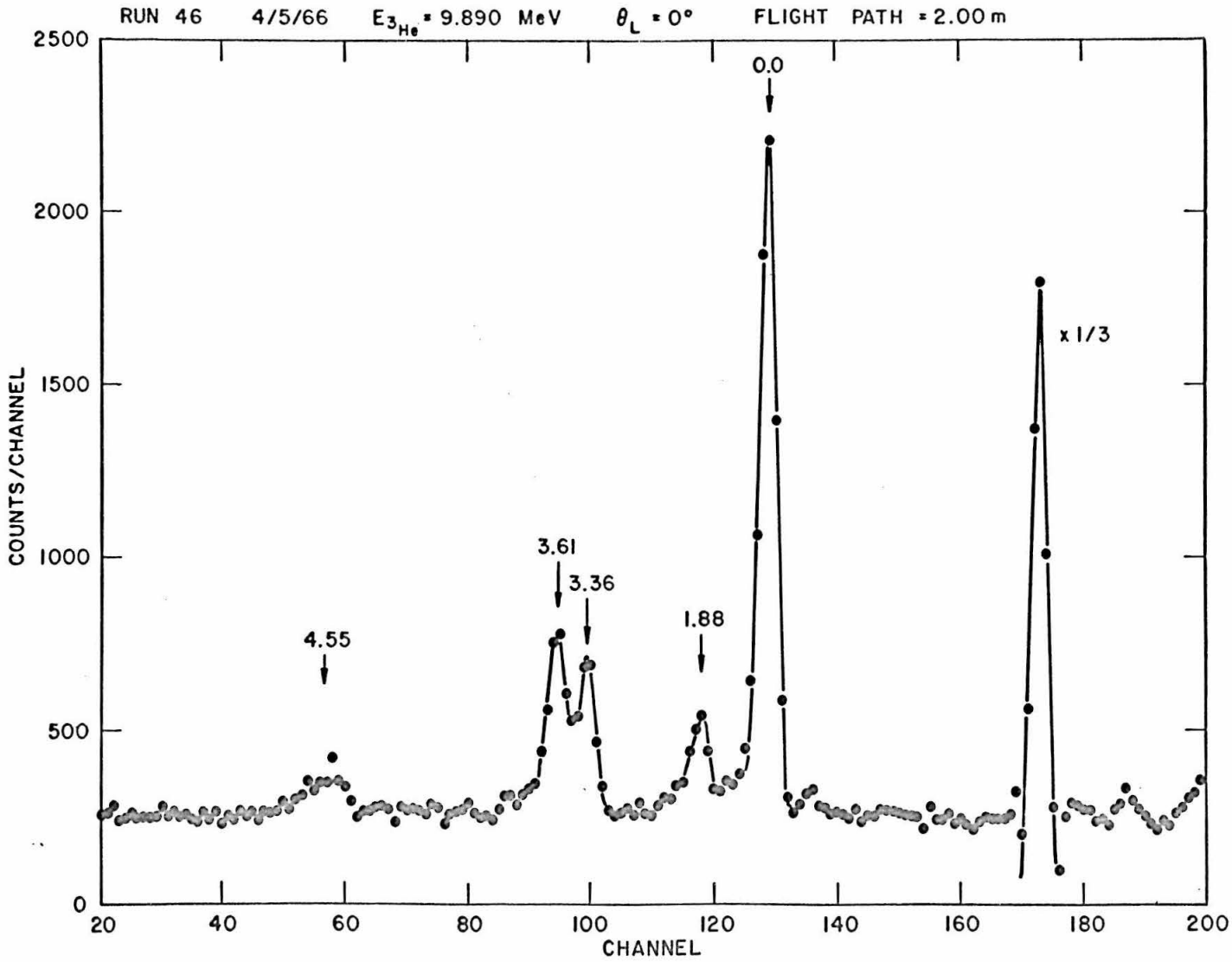
RUN 46 4/5/66 $E_{^3He}$ = 9.890 MeV θ_L = 0° FLIGHT PATH = 2.00 m
COUNTS/CHANNEL
CHANNEL
0.0
x 1/3
3.61
3.36
1.88
4.55
0
500
1000
1500
2000
2500
20
40
60
80
100
120
140
160
180
200

Figure 13

Angular distributions of neutrons from the $O^{16}(He^3, n)$ reaction at 9.0 MeV incident energy. The error bars include contributions from counting statistics, and uncertainties in mean background, detector efficiency and beam current integration. The smooth curves are fits using the plane wave theory of Newns (1960) with the cutoff radius, r, and normalization treated as free parameters. (See pages 31, 33, and 35). The 3.36 and 3.61 MeV states were not fitted since they did not appear to be populated primarily by direct reactions at this energy. 100 arbitrary units of differential cross section correspond to 1.4 ± 0.3 mb/sr.

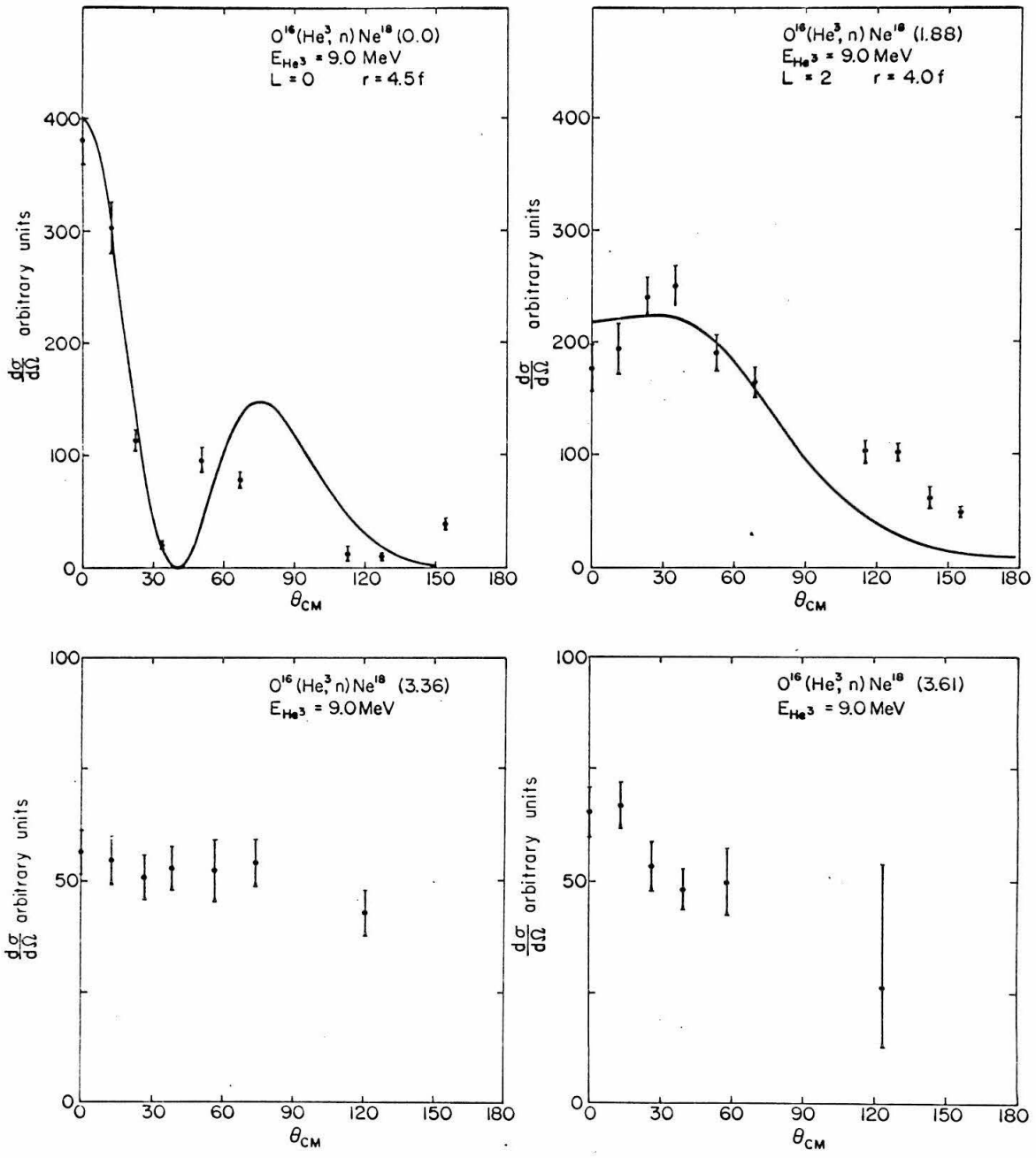
O16(He3, n) Ne18 (0.0)
EHe3 = 9.0 MeV
L = 0 r = 4.5f
O16(He3, n) Ne18 (1.88)
EHe3 = 9.0 MeV
L = 2 r = 4.0f
O16 (He3 n) Ne18 (3.36)
EHe3 = 9.0MeV
O16 (He3, n) Ne18 (3.61)
EHe3 = 9.0 MeV
dσ/dΩ arbitrary units
θCM
0
30
60
90
120
150
180
100
200
300
400
50

Figure 14

Angular distributions of neutrons from the $O^{16}(He^3, n)$ reaction at 10.5 MeV incident energy. The error bars include contributions from counting statistics and uncertainties in the mean background, detector efficiency, and beam current integration. In addition to the errors denoted by the flags there is an estimated uncertainty of $\pm$ 10% in the absolute normalization. The smooth curves are DWBA calculations with only the normalization treated as a free parameter. Fits to the angular distributions of the 3.36 and 3.61 MeV states were attempted for L = 0, 1, 2, 3, and 4. The 3.36 MeV state is fitted by L = 2, the next best fit (which is much poorer over the main peak) is found for L = 0. The 3.61 MeV state has been fitted with a mixture of L = 0 and L = 4 since it is suspected that this "level" may be an unresolved doublet. The percentage refers to the ratio of normalizing constants needed to obtain the fit. The configurations of the residual nuclei indicated in this figure and in Figures 17, 38, 39, 40, 41, and 50 are believed to represent important components of the wave functions. However, the calculations do not distinguish between configurations which have the same values of $2n + \ell$; for example, between 1d and 2s or 2p and 1f. (See pages 31 and 34.)

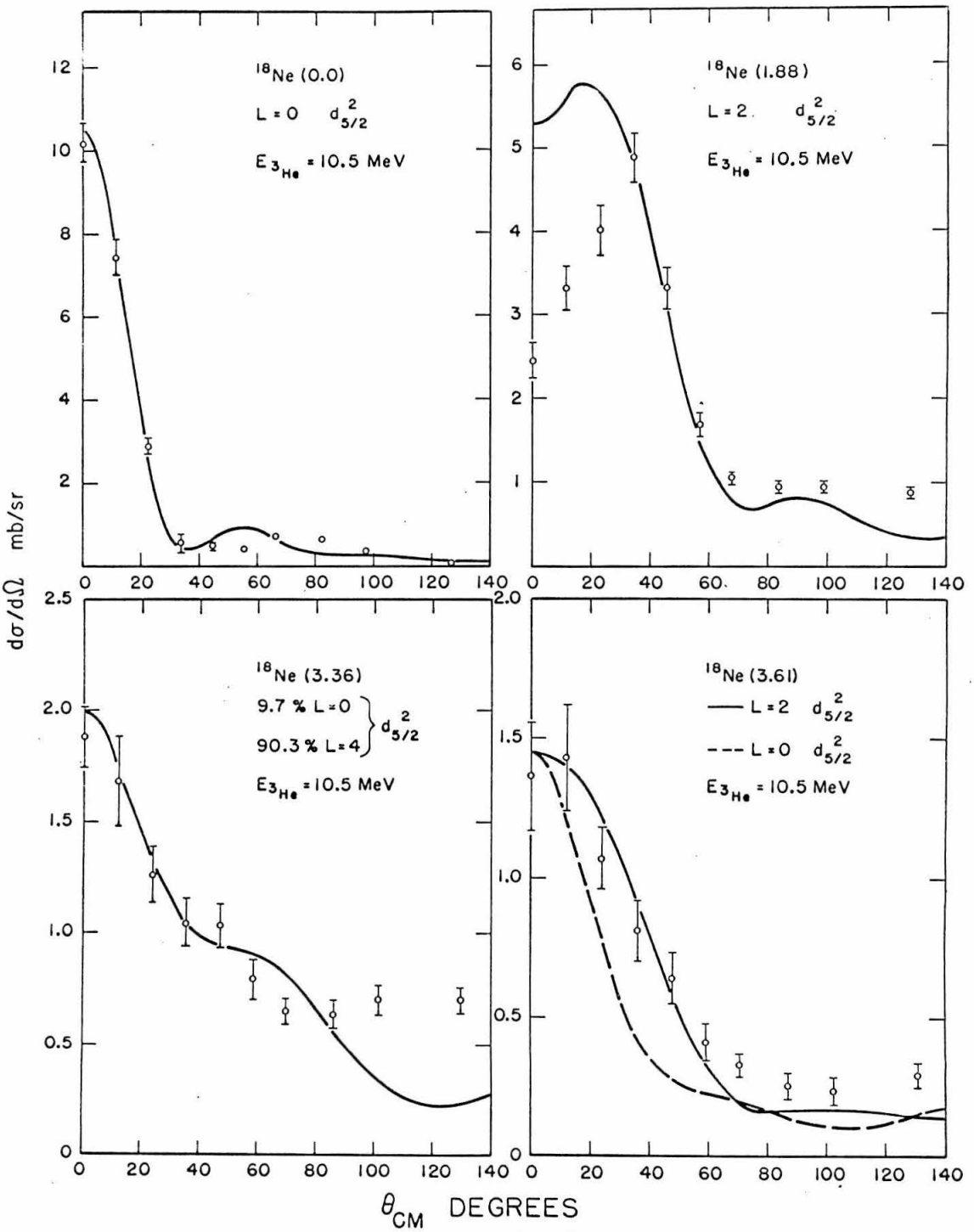
^{18}Ne (0.0)
L = 0 $d^2_{5/2}$
$E_{^3He}$ = 10.5 MeV
^{18}Ne (1.88)
L = 2 $d^2_{5/2}$
$E_{^3He}$ = 10.5 MeV
^{18}Ne (3.36)
9.7 % L = 0
90.3 % L = 4
$d^2_{5/2}$
$E_{^3He}$ = 10.5 MeV
^{18}Ne (3.61)
— L = 2 $d^2_{5/2}$
--- L = 0 $d^2_{5/2}$
$E_{^3He}$ = 10.5 MeV
dσ/dΩ mb/sr
θ_{CM} DEGREES

Figure 15

Angular distributions of neutrons from the $O^{16}(He^3, n)$ reaction at 12.5 MeV incident energy. The error bars include contributions from counting statistics, and uncertainties in mean background, detector efficiency and beam current integration. The smooth curves are fits using the plane wave theory of Newns (1960) with the cutoff radius, r, and the normalization treated as free parameters. Note the unexpectedly strong L = 1 transition to the 4.55 MeV state. 100 arbitrary units of differential cross section correspond to 1.4 ± 0.3 mb/sr. (See pages 31 and 35)

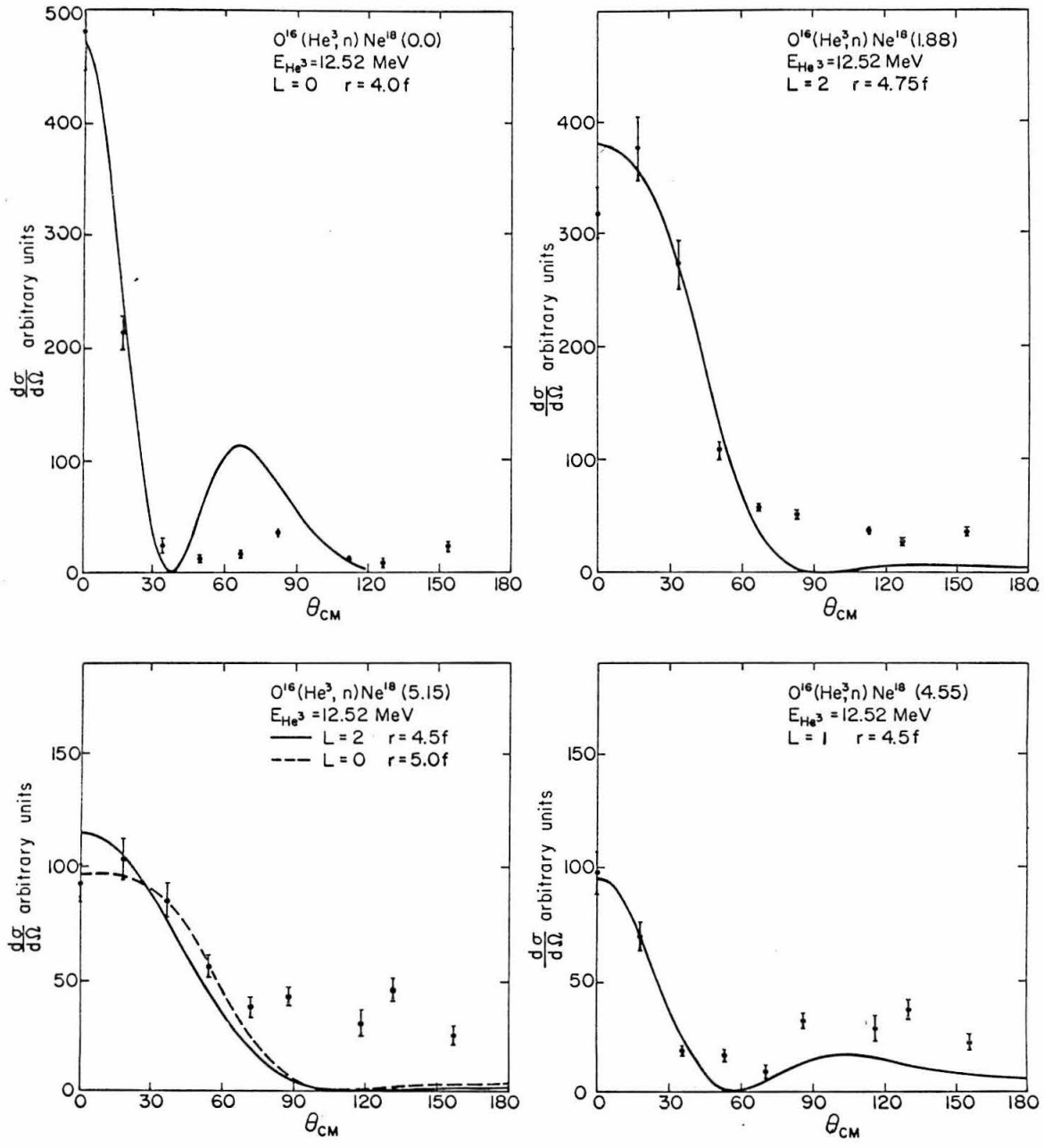
O16(He3, n) Ne18 (0.0)
EHe3 = 12.52 MeV
L = 0 r = 4.0f
O16(He3,n) Ne18 (1.88)
EHe3 = 12.52 MeV
L = 2 r = 4.75f
O16(He3, n)Ne18 (5.15)
EHe3 = 12.52 MeV
L = 2 r = 4.5f
L = 0 r = 5.0f
O16(He3,n) Ne18 (4.55)
EHe3 = 12.52 MeV
L = 1 r = 4.5f
dσ/dΩ arbitrary units
θCM

Figure 16

Angular distribution of protons from the $O^{16}(t, p)$ reaction at 10.0 MeV incident energy (Middleton and Pullen 1964b). The curves are calculated from the plane wave theory (Newns 1960) using a cutoff radius a = 5.5f, except for the 5.33 MeV state which requires a = 5.0f. Compare with angular distributions of the $O^{16}(He^3, n)$ reaction presented in Figure 15. For a discussion of difficulties arising from this comparison see pages 33 - 38.

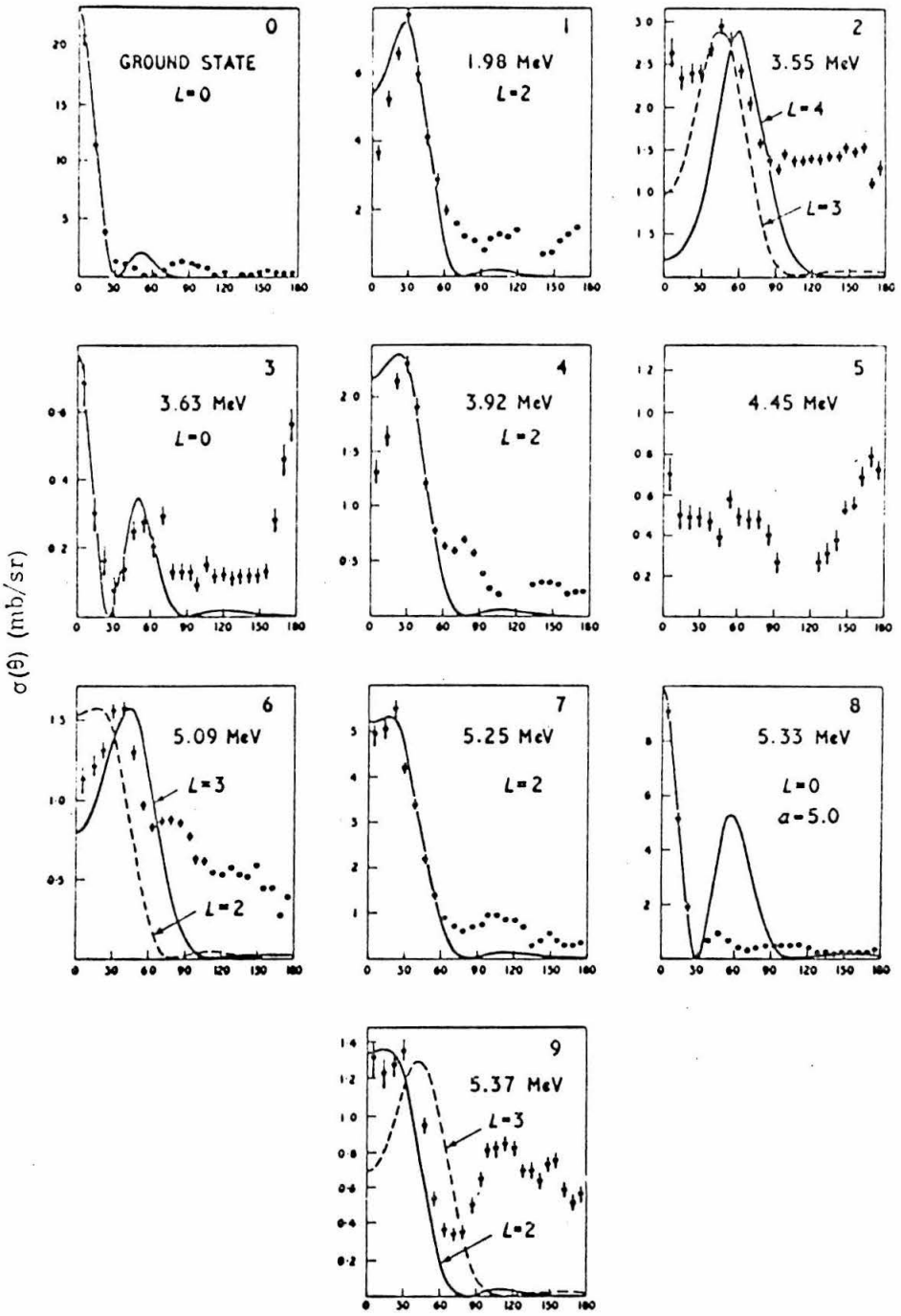
0
GROUND STATE
L=0
1
1.98 MeV
L=2
2
3.55 MeV
L=4
L=3
3
3.63 MeV
L=0
4
3.92 MeV
L=2
5
4.45 MeV
6
5.09 MeV
L=3
L=2
7
5.25 MeV
L=2
8
5.33 MeV
L=0
a=5.0
9
5.37 MeV
L=3
L=2
σ(θ) (mb/sr)
Angle (c.m.) (deg)

Figure 17

Angular distributions of neutrons from the $O^{16}(He^3, n)$ reaction at 12.5 MeV incident energy. The smooth curves are DWBA calculations with only the normalization treated as a free parameter. Compare with plane wave fits to the same data presented in Figure 15. (See page 34)

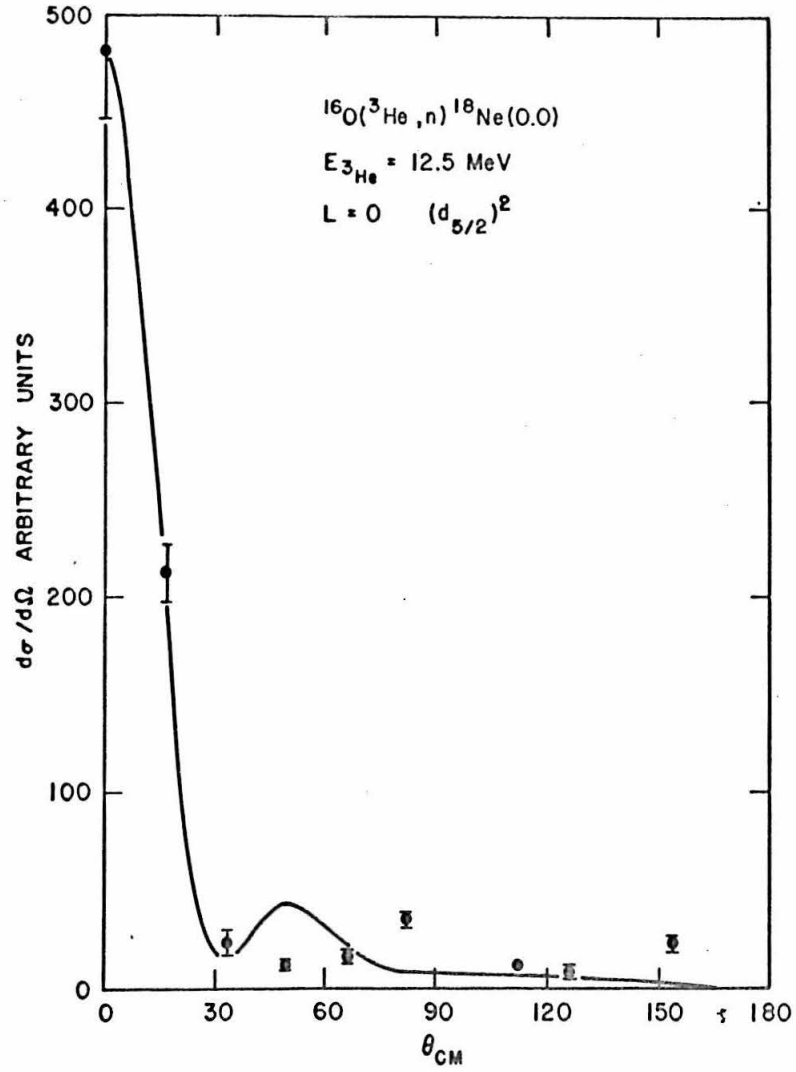
$^{16}O(^3He,n)^{18}Ne(0.0)$
$E_{^3He}$ = 12.5 MeV
L = 0 $(d_{5/2})^2$
$d\sigma/d\Omega$ ARBITRARY UNITS
θ_{CM}
0
30
60
90
120
150
180
100
200
300
400
500

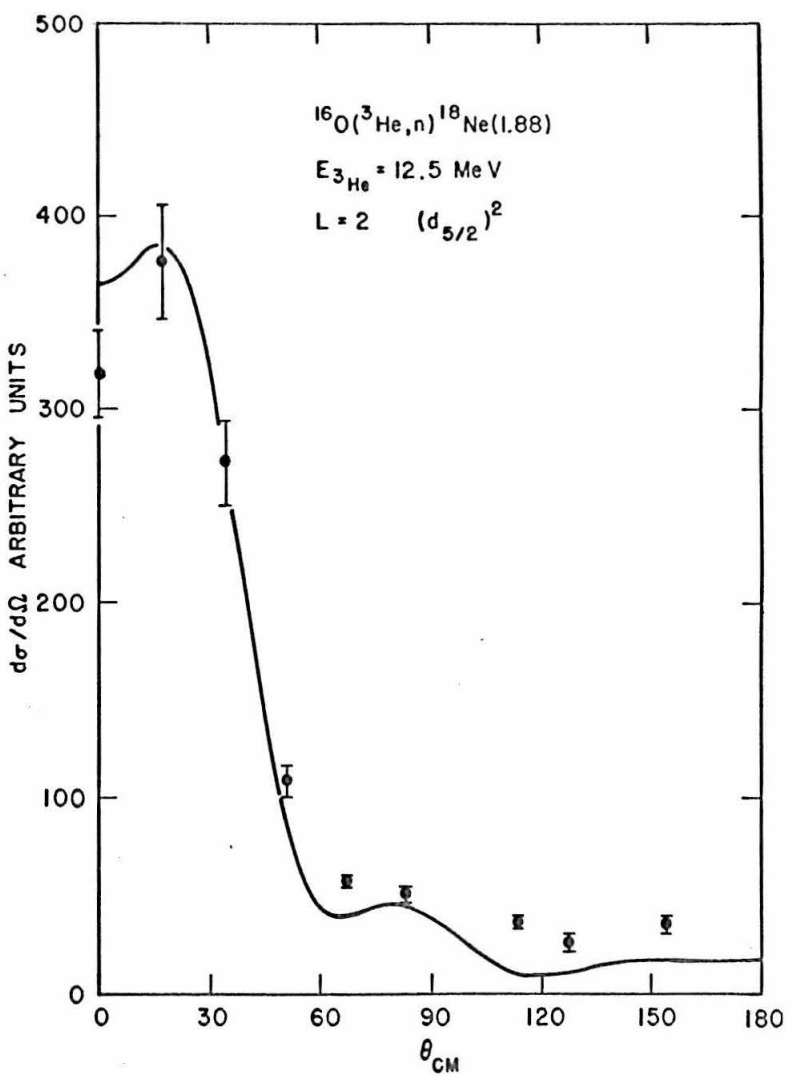
$^{16}O(^3He,n)^{18}Ne(1.88)$
$E_{^3He}$ = 12.5 MeV
L = 2 $(d_{5/2})^2$
$d\sigma/d\Omega$ ARBITRARY UNITS
θ_{CM}
0
30
60
90
120
150
180
100
200
300
400
500

Figure 18

Isobar diagram of low-lying levels in the A = 18 nuclei. This diagram was obtained by adding the information on Ne^{18} presented here to a diagram comparing the low-lying levels of O^{18} and F^{18} (Ollerhead et al., 1965). T = 0 levels in F^{18} (except for the ground state) have been eliminated for clarity. The energy scales have been shifted to account for Coulomb energies and the neutron proton mass difference. Coulomb energies were calculated from the formula (Lauritsen and Ajzenberg-Selove 1966) $E_c = 0.60\ Z(Z-1)A^{-1/3}$ (MeV). Decay thresholds are shown, but reactions leading to the nuclei under consideration have been omitted for simplicity. Spins and parities which are considered reasonably well established are indicated on the levels; values which are uncertain are enclosed in parenthesis. Isobaric analogs are connected by straight lines. Those which are considered well established are denoted by solid lines, tentative identifications are dotted. We suggest that the 3.36 MeV "state" in Ne^{18} may be a 0^+, 4^+ doublet. Ollerhead et al., argue that the 5.59 and 5.66 MeV states in F^{18} may be strongly mixed between T = 0, and T = 1. The identification of the 4.55 MeV state in Ne^{18} as the analog of the 4.45 MeV state in O^{18} is especially uncertain. If correct, isospin conservation is blatantly violated. For a discussion see pages 35 through 37.

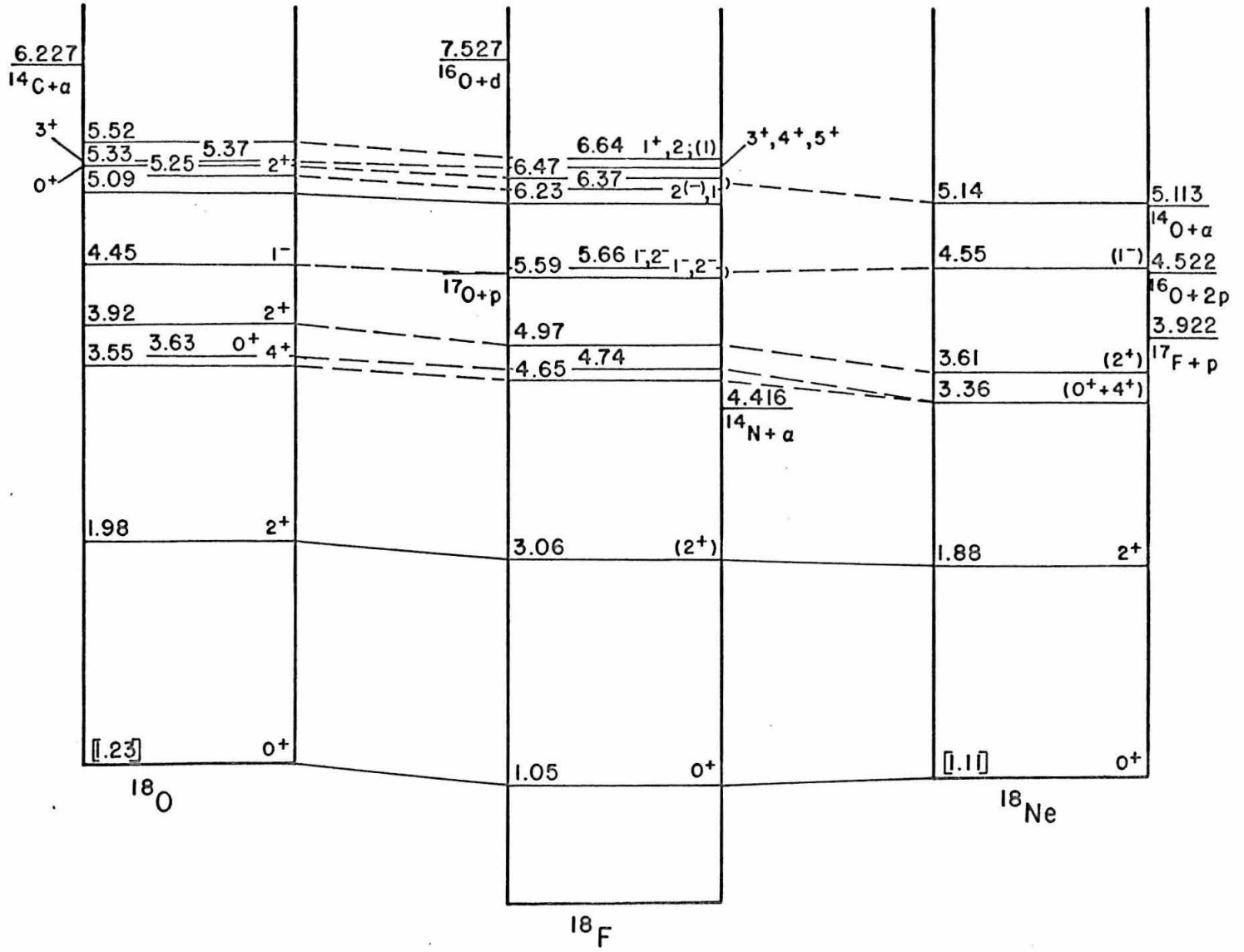
6.227
14C+α
3+
0+
5.52
5.33
5.25
5.37
2+
5.09
4.45
1−
3.92
2+
3.55
3.63
0+
4+
1.98
2+
[1.23]
0+
18O
7.527
16O+d
6.64
1+,2;(1)
6.47
6.37
6.23
2(−),1−
5.59
5.66
1−,2−
1−,2−
17O+p
4.97
4.65
4.74
3.06
(2+)
1.05
0+
18F
3+,4+,5+
4.416
14N+α
5.14
4.55
(1−)
3.61
(2+)
3.36
(0++4+)
1.88
2+
[1.11]
0+
18Ne
5.113
14O+α
4.522
16O+2p
3.922
17F+p

Figure 19

Time spectrum of neutrons from the $B^{11}(He^3, n)$ reaction at an incident energy of 7.0 MeV. The excitation energies indicated above the neutron peaks correspond to some of the known states in N^{13}. The prominent peak labelled 15.07 corresponds to the lowest T = 3/2 state in N^{13}. Neutron groups arising from C^{12} and O^{16} contaminants are labelled by the residual nucleus. This spectrum was used in the determination of the excitation energy of the lowest T = 3/2 state. The time scale is about 1 ns/ch. (See pages 42 and 44)

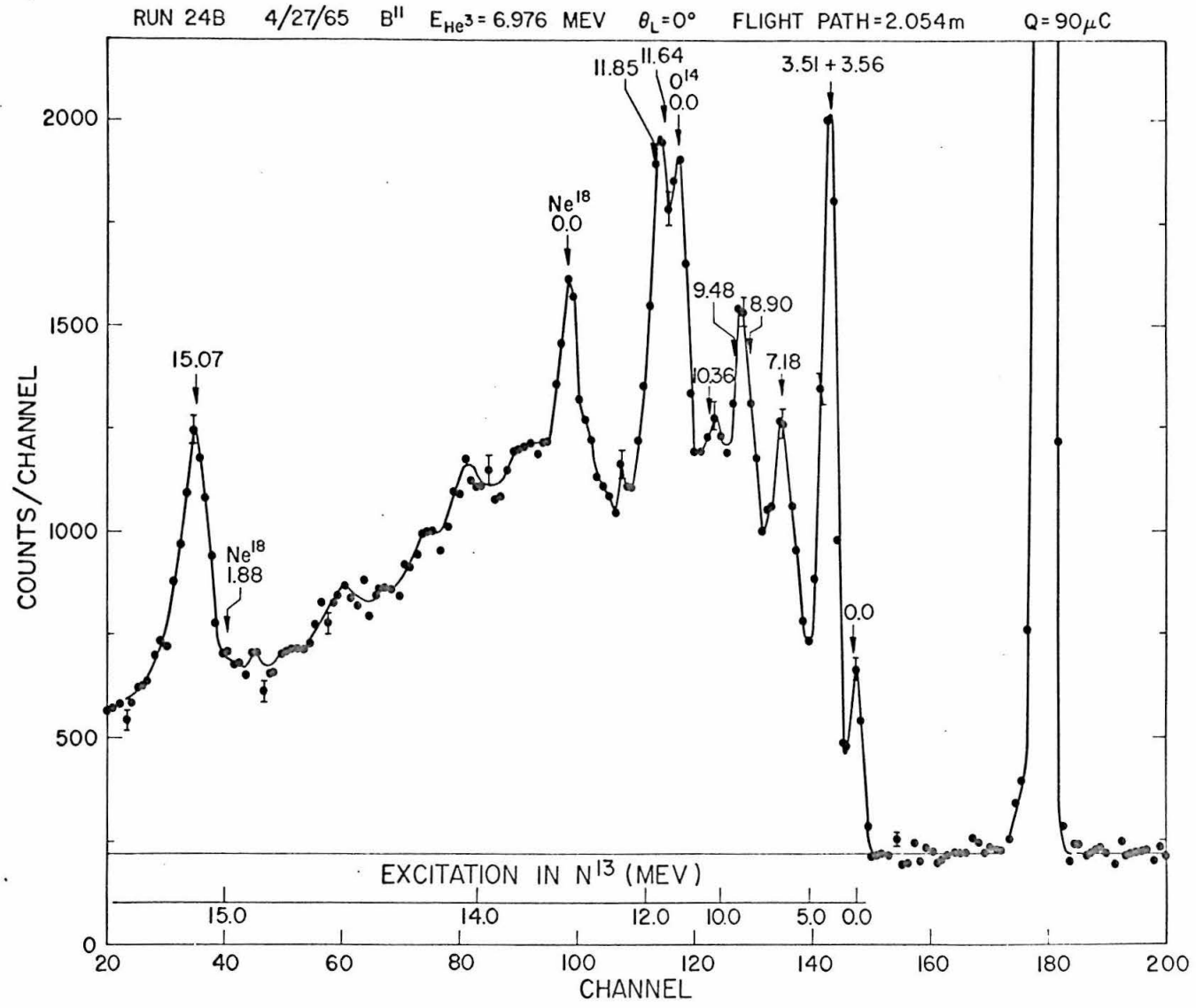
RUN 24B 4/27/65 B11 E_He3 = 6.976 MEV θ_L = 0° FLIGHT PATH = 2.054 m Q = 90 μC
11.85
11.64
O14
0.0
3.51 + 3.56
Ne18
0.0
9.48
8.90
10.36
7.18
15.07
Ne18
1.88
0.0
COUNTS/CHANNEL
EXCITATION IN N13 (MEV)
15.0
14.0
12.0
10.0
5.0
0.0
CHANNEL

Figure 20

Time spectrum of neutrons from the $B^{11}(He^3, n)$ reaction at 9.00 MeV incident energy. Numbers above the peaks correspond to excitation energies of some known states in N^{13}. The positions of neutron groups arising from C^{12} or O^{16} contaminants are labeled by the residual nucleus. The lines under the 3.5 and 15.07 MeV groups indicate typical background subtractions used in computing the angular distributions shown in Figures 29 and 30. A small correction was made to the peak area for a contribution from Ne^{18}(1.88). The time scale is 1 ns/ch.
(See pages 42 and 48.)

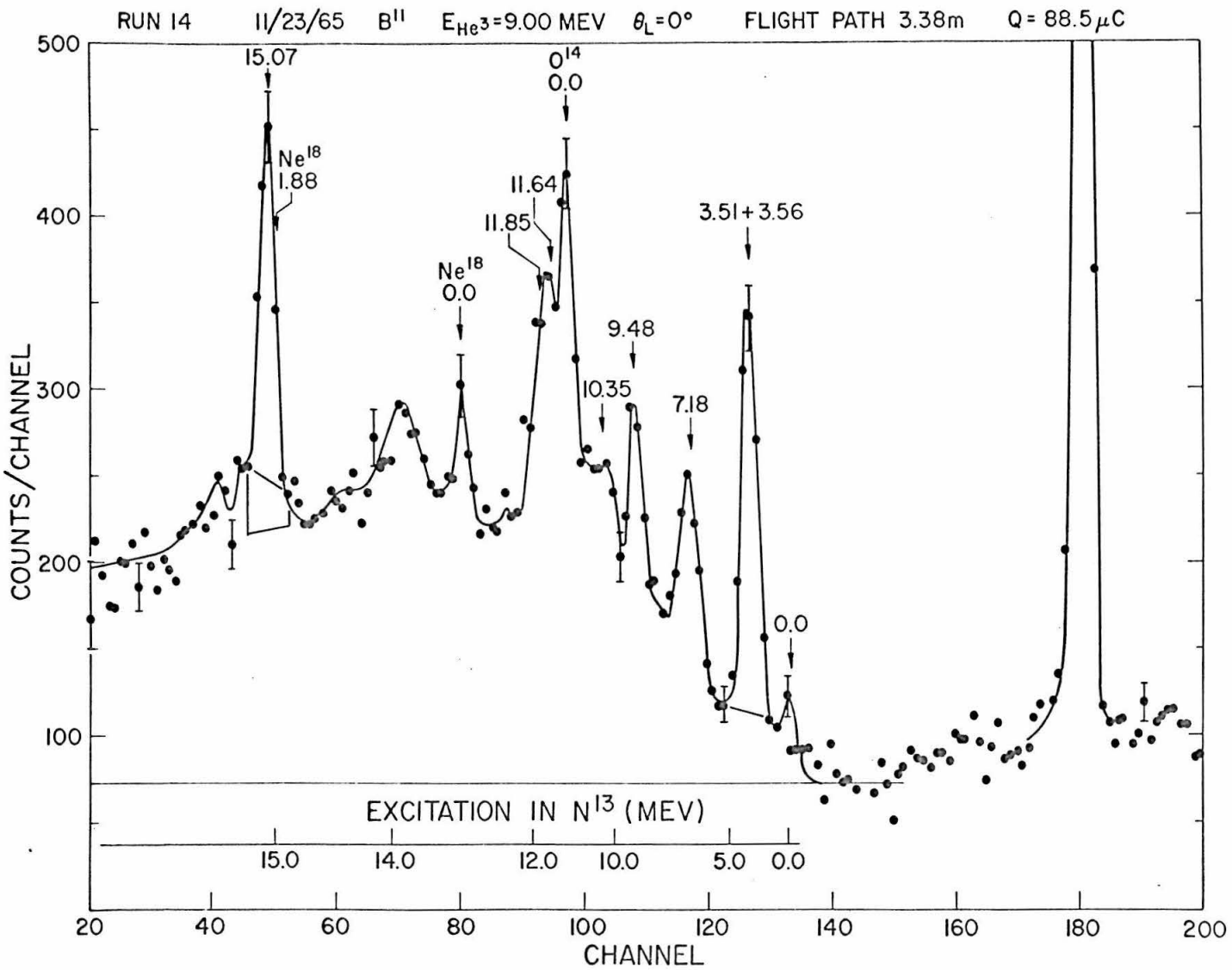
RUN 14 11/23/65 B11 E$_{He^3}$=9.00 MEV θ_L=0° FLIGHT PATH 3.38m Q = 88.5 μC
COUNTS/CHANNEL
CHANNEL
15.07
Ne18 1.88
O14 0.0
11.64
11.85
Ne18 0.0
9.48
10.35
7.18
3.51+3.56
0.0
EXCITATION IN N13 (MEV)
15.0
14.0
12.0
10.0
5.0
0.0
500
400
300
200
100
20
40
60
80
100
120
140
160
180
200

Figure 21

Time spectrum of neutrons from the $B^{11}(He^3, n)$ reaction at 12.5 MeV incident energy. T = 3/2 levels in N^{13} are labelled by their excitation energy. The 18.98 MeV state is clearly visible in this spectrum, which was used in a determination of the width of this level. A weak gamma ray peak from the out-of-phase beam burst is superimposed upon the neutron group from the 18.44 MeV state. Gamma ray peaks are identified by measuring the change in flight time caused by a small change in flight path. The time scale is approximately 1 ns/ch. (See pages 42 and 56)

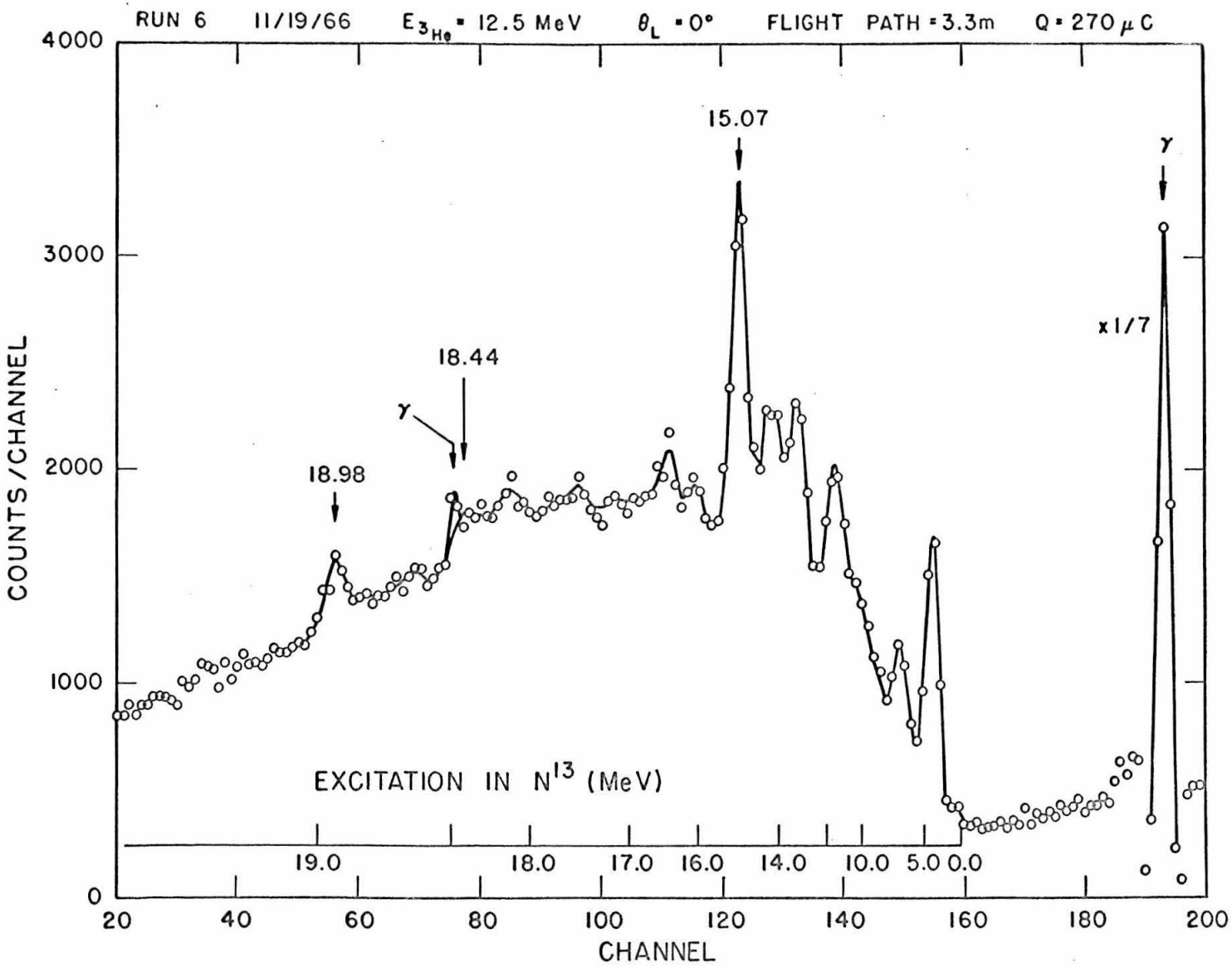
RUN 6 11/19/66 $E_{^3He}$ = 12.5 MeV θ_L = 0° FLIGHT PATH = 3.3m Q = 270 μC
COUNTS/CHANNEL
CHANNEL
15.07
γ
18.44
γ
18.98
x1/7
EXCITATION IN N^{13} (MeV)
19.0
18.0
17.0
16.0
14.0
10.0
5.0
0.0
0
1000
2000
3000
4000
20
40
60
80
100
120
140
160
180
200

Figure 22

Time spectrum of the $B^{11}(He^3, n)$ reaction at 13.52 MeV incident energy. The T = 3/2 levels are indicated by their excitation energies. The peaks labelled γ are due to gamma rays. The peak on the left is caused by the out-of-phase beam burst; the one to the right is due to the beam striking a slit. Gamma rays are identified by observing the time shift caused by a small change in flight path. (See page 42)

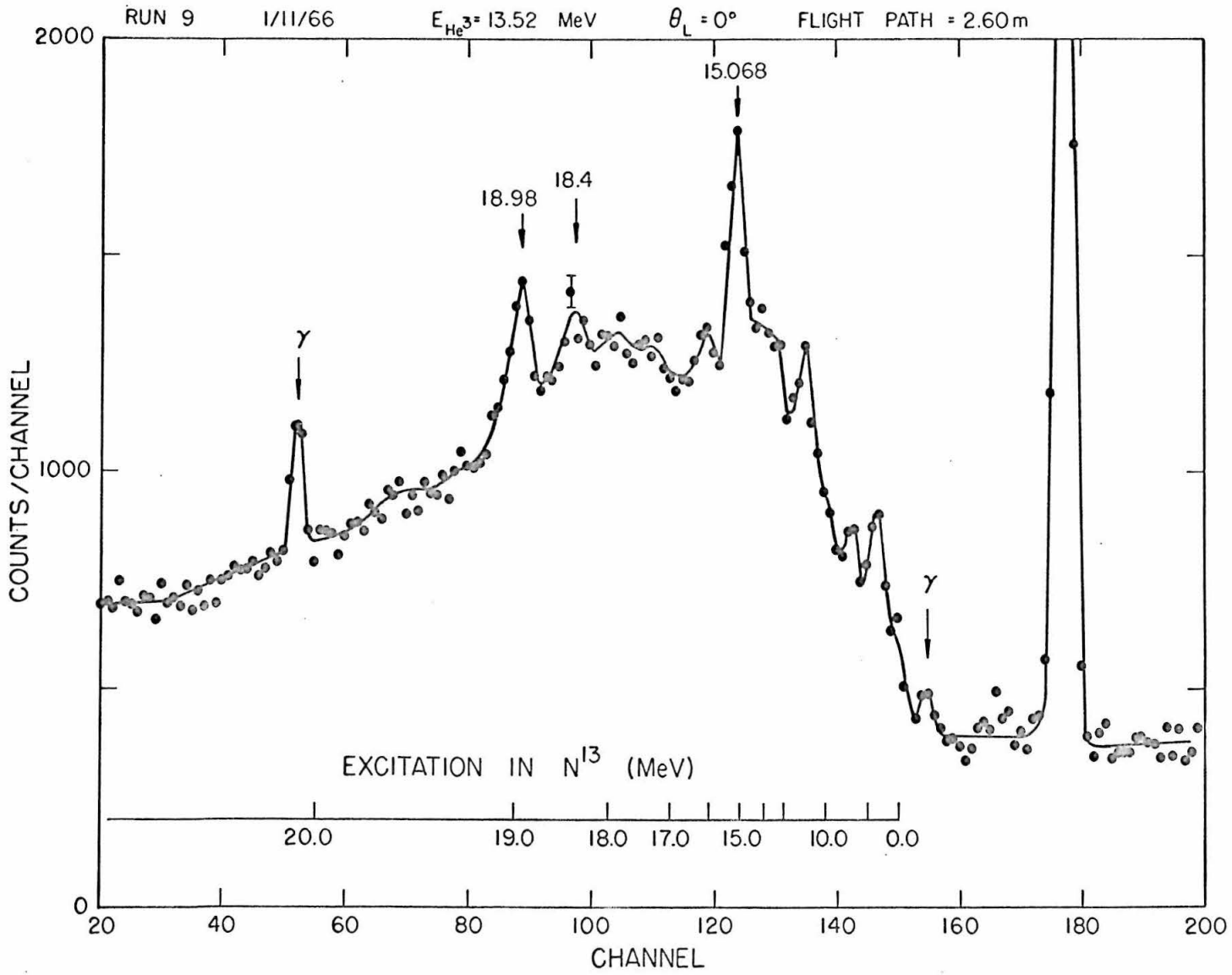
RUN 9 1/11/66 E_{He^3} = 13.52 MeV θ_L = 0° FLIGHT PATH = 2.60 m
15.068
18.98
18.4
γ
γ
COUNTS/CHANNEL
2000
1000
0
EXCITATION IN N^{13} (MeV)
20.0
19.0
18.0
17.0
15.0
10.0
0.0
20
40
60
80
100
120
140
160
180
200
CHANNEL

Figure 23

Demonstration that the previously unobserved neutron group corresponds to a state in N^{13}. The measured Q-value for the (He^3, n) reaction at laboratory angles between 0^o and 135^o is plotted versus laboratory angle. The data were taken at an incident energy of 9.0 MeV and were computed assuming targets of B^{10}, B^{11}, and C^{12}. The data can be fitted with a single Q-value only by assuming a B^{11} target. The error bars are derived from estimates of the energy uncertainty, and not statistical. Hence the tabulated quantity "chi-squared", while a relative measure of the goodness of fit, has no interpretation in terms of probabilities. (See page 43)

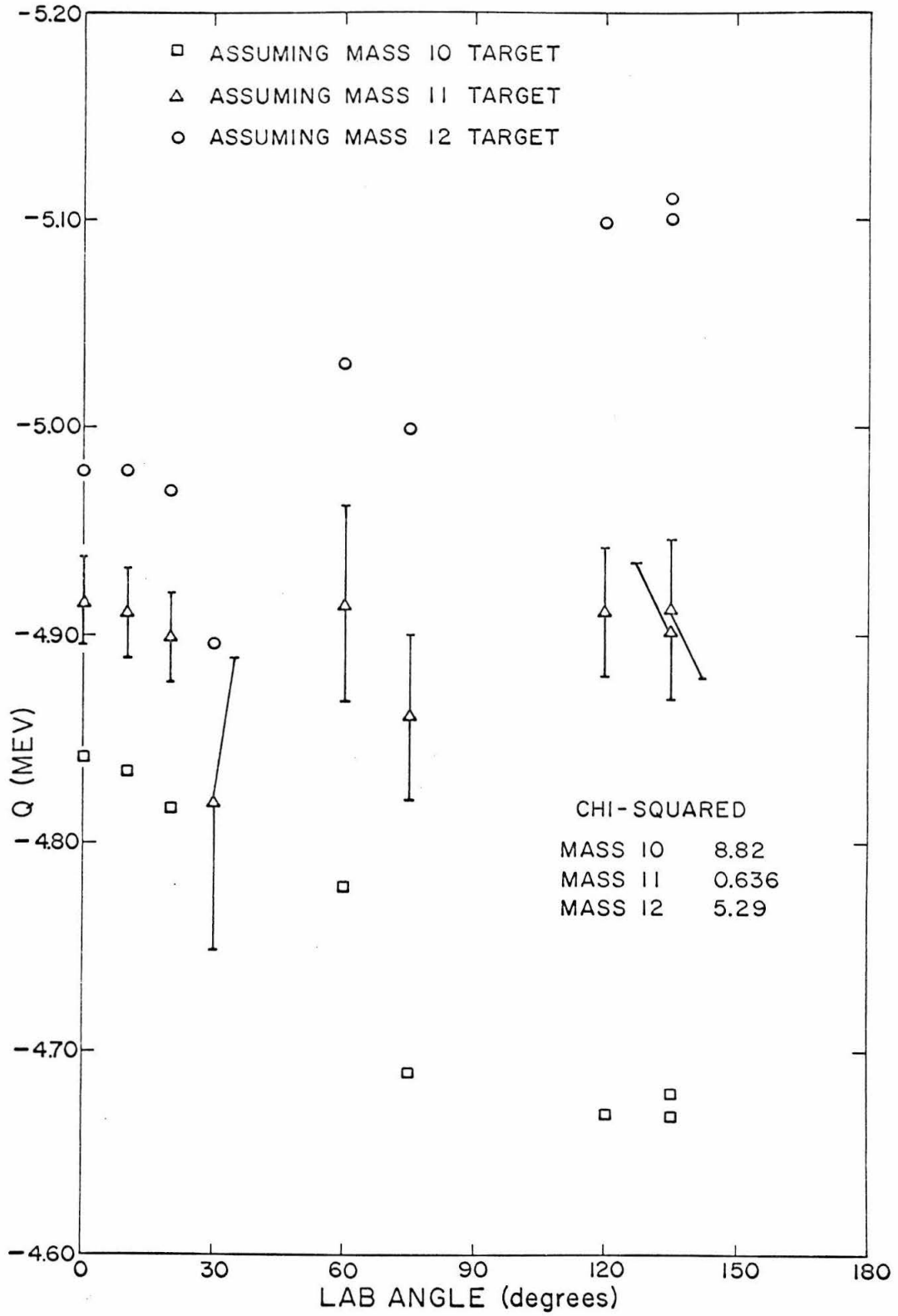
□ ASSUMING MASS 10 TARGET
△ ASSUMING MASS 11 TARGET
○ ASSUMING MASS 12 TARGET
-5.20
-5.10
-5.00
-4.90
-4.80
-4.70
-4.60
Q (MEV)
0
30
60
90
120
150
180
LAB ANGLE (degrees)
CHI-SQUARED
MASS 10 8.82
MASS 11 0.636
MASS 12 5.29

Figure 24

Comparison of spectra taken with targets of B^{11} and natural carbon. The spectra were taken at the same beam energy and detector geometry. The prompt gamma peaks in both spectra have been superimposed. By using the 6.59 MeV state in O^{14} to normalize the amount of carbon in the B^{11} spectrum one can readily see that the 18.44 and 18.98 MeV states cannot be attributed to a carbon contaminant. (See page 43)

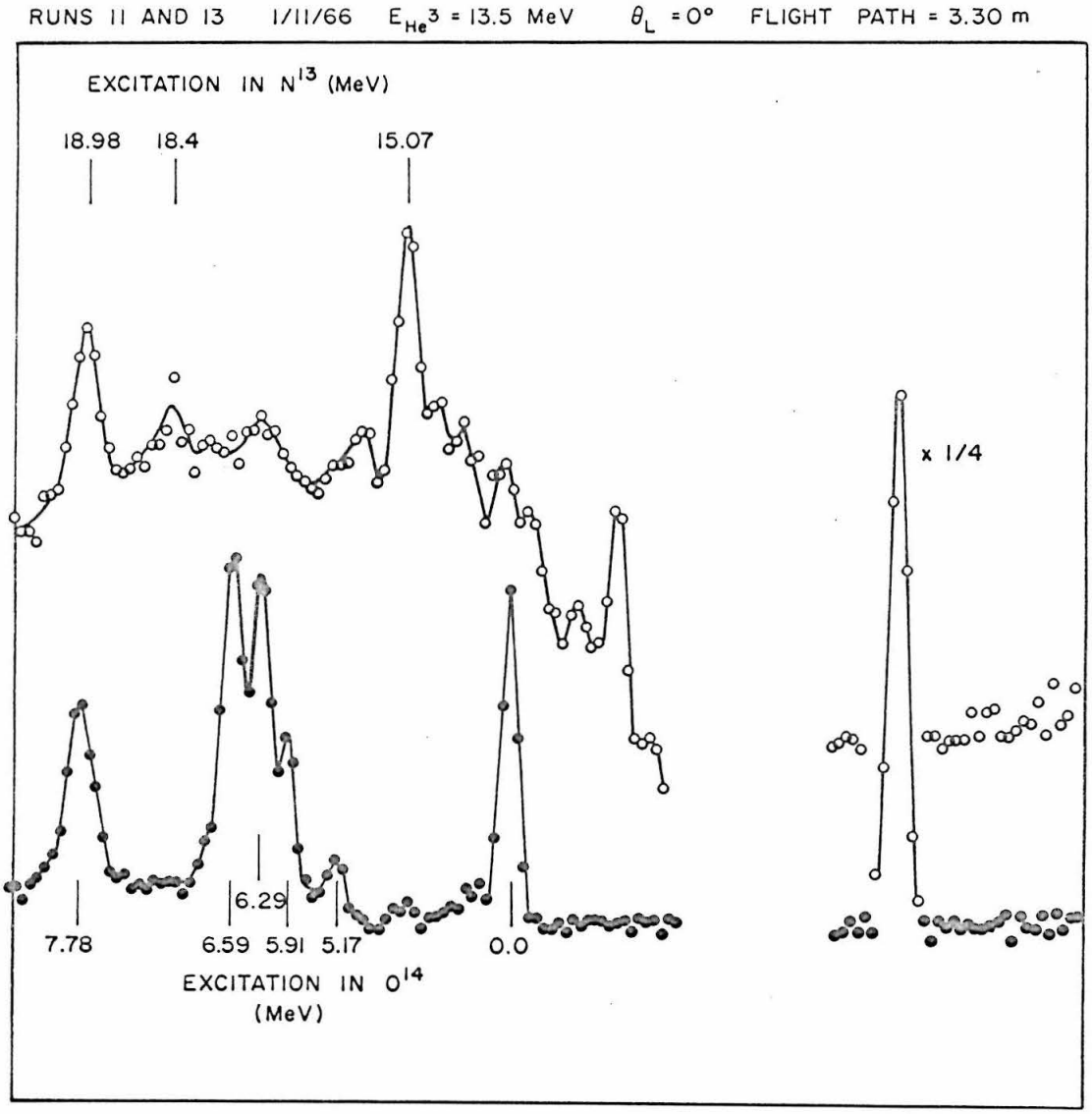
RUNS 11 AND 13 1/11/66 E_{He^3} = 13.5 MeV θ_L = 0° FLIGHT PATH = 3.30 m
EXCITATION IN N^{13} (MeV)
18.98
18.4
15.07
x 1/4
7.78
6.59
6.29
5.91
5.17
0.0
EXCITATION IN O^{14} (MeV)

Figure 25

Comparison of spectra taken with targets of B^{11} and tungsten oxide. The spectra were taken at the same beam energy and detector geometry. The prompt gamma peaks in both spectra have been superimposed. It is readily seen that the 18.44 and 18.98 MeV states could not be produced by oxygen. (See page 43)

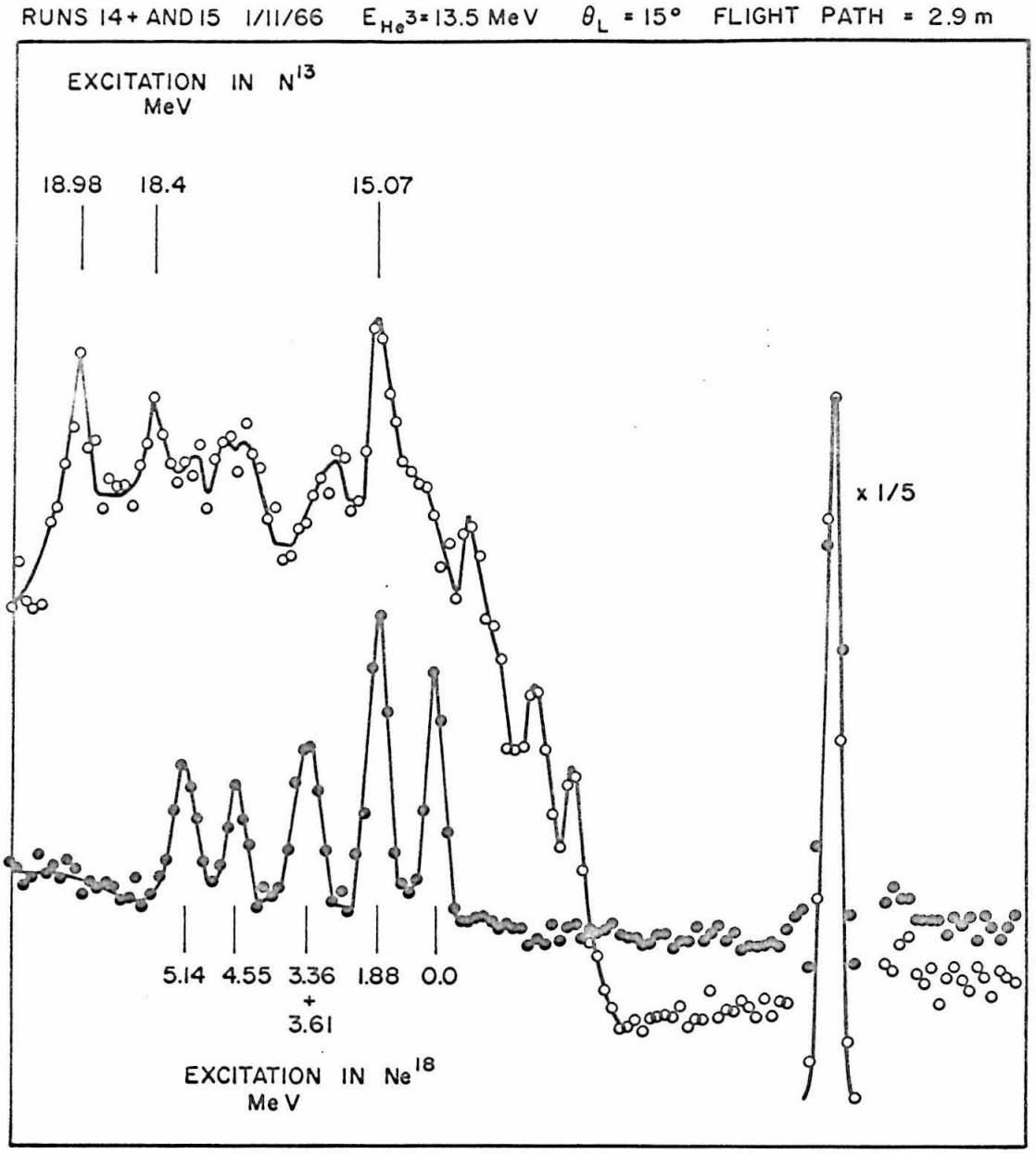
RUNS 14+ AND 15 1/11/66 E_{He^3}=13.5 MeV θ_L = 15° FLIGHT PATH = 2.9 m
EXCITATION IN N^{13} MeV
18.98
18.4
15.07
x 1/5
5.14
4.55
3.36
+
3.61
1.88
0.0
EXCITATION IN Ne^{18} MeV

Figure 26

Demonstration that the 18.98 MeV state is produced in the $B^{11}(He^3, n)$ reaction. In the upper part of this figure we have plotted the chi-square for fits of the experimental Q-value determined at $\theta_L = 0^o$, 15^o, and 30^o to a constant. The graph displays chi-square as a function of assumed target mass. The data is best fitted by an A = 11 target. In the bottom part of the figure we have plotted the best fit of the experimental Q-value (MeV) versus laboratory neutron angle (degrees). The error bars are derived from an estimate of the energy uncertainty and are not purely statistical. Hence the "chi-square" displayed above has no interpretation in terms of probability, but is only a measure of relative goodness of fit. The best-fit value of Q was used in determining the excitation energy of the 18.98 MeV state. (See page 44)

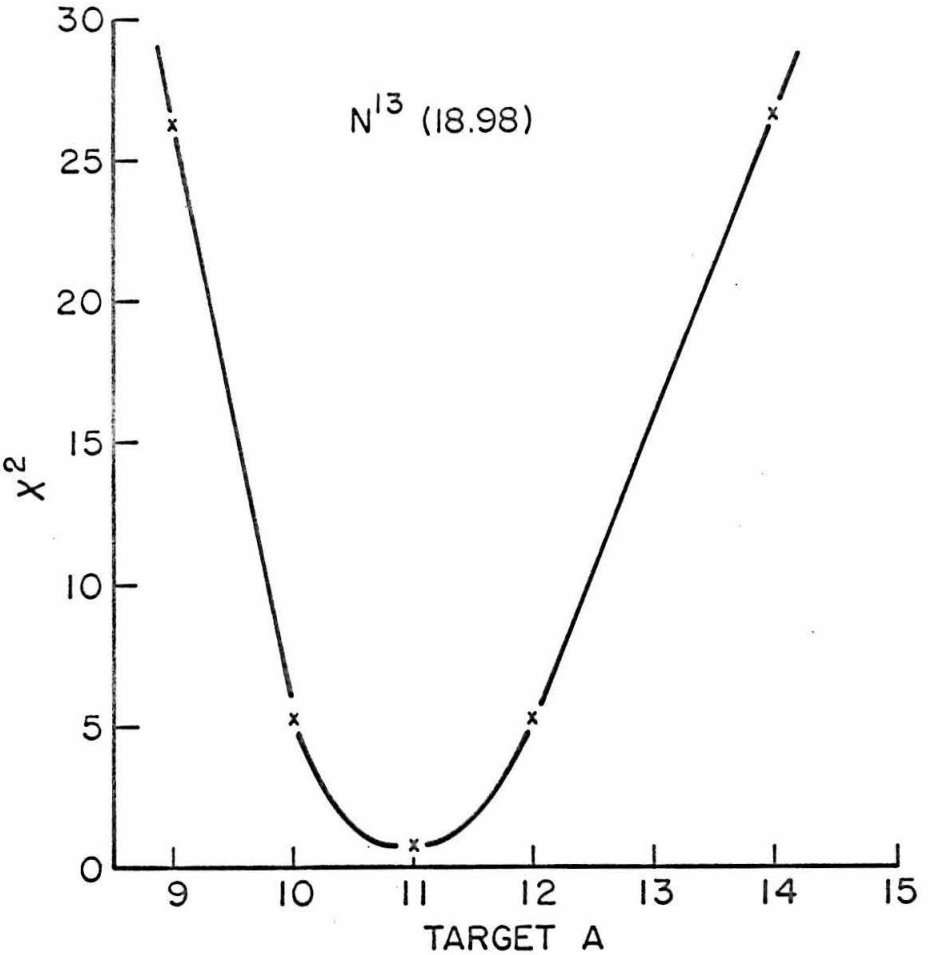
N^{13} (18.98)
χ^2
TARGET A

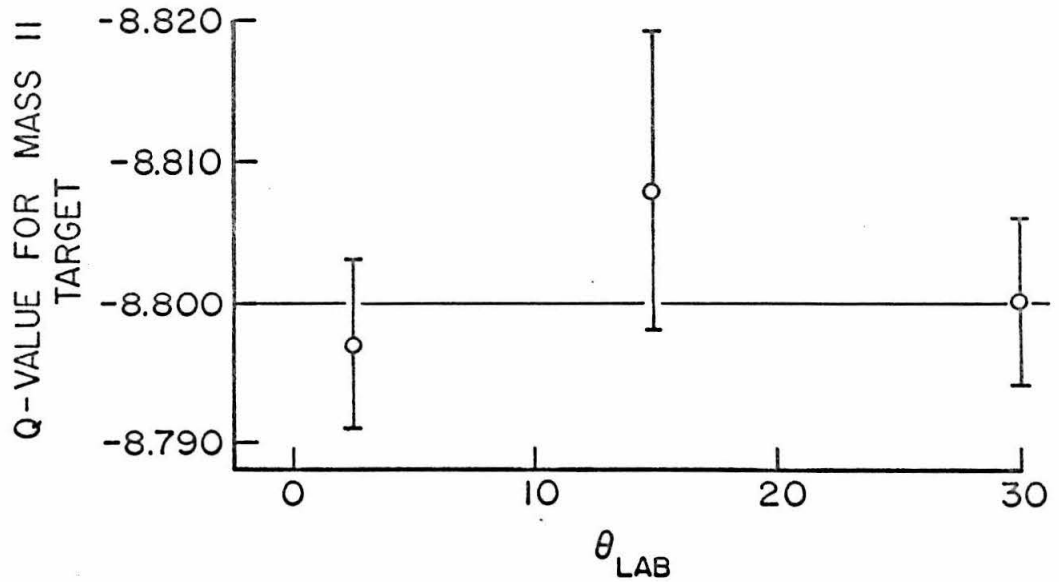
Q-VALUE FOR MASS 11 TARGET
θ_{LAB}

Figure 27

Time spectrum from the reaction $B^{11}(p, n)$ at an incident energy of 4 MeV. This spectrum was used to calibrate the time scale in Figure 19. The time scale is about 1 ns/ch. (See pages 13 and 44.)

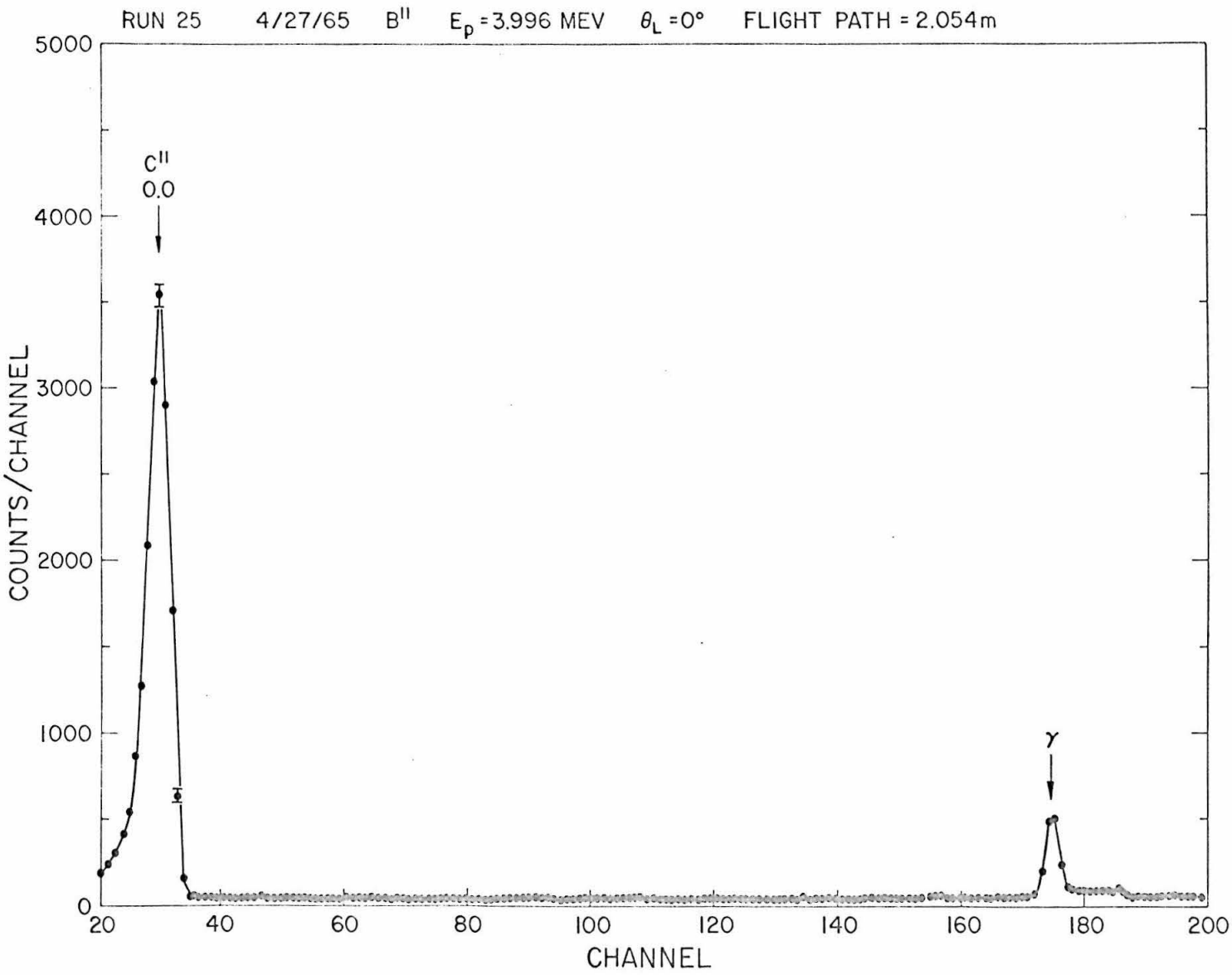
RUN 25 4/27/65 B11 Ep = 3.996 MEV θL = 0° FLIGHT PATH = 2.054m
C11
0.0
γ
COUNTS/CHANNEL
CHANNEL
0
1000
2000
3000
4000
5000
20
40
60
80
100
120
140
160
180
200

Figure 28

Time spectrum of neutrons from the $B^{11}(He^3, n)$ reaction at $E_{He^3} = 9.0$ MeV, $\theta_{lab} = 120^{o}$. This spectrum was used in obtaining the angular distribution presented in Figure 29. (See page 48)

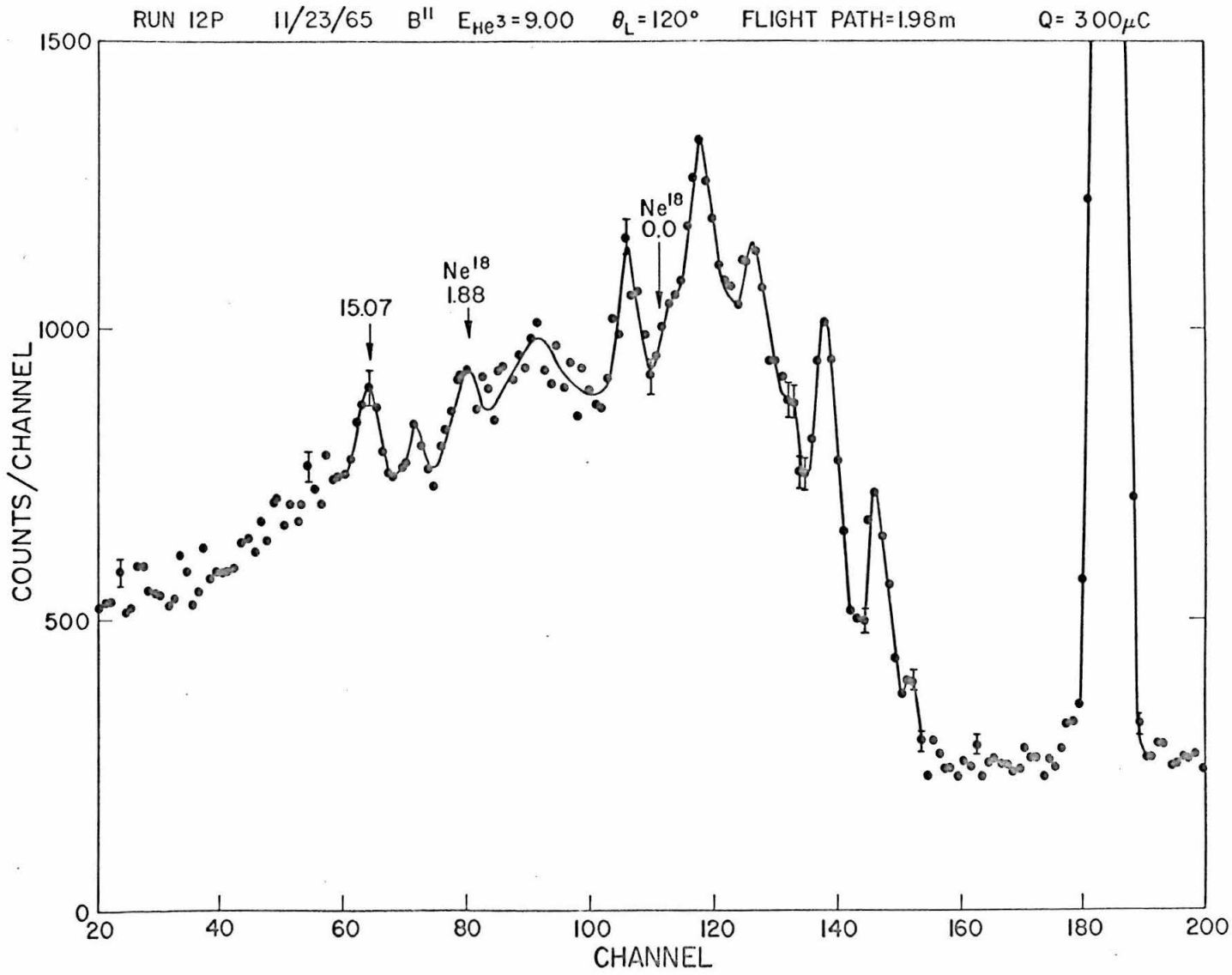
RUN 12P 11/23/65 B11 E_He3 = 9.00 θ_L = 120° FLIGHT PATH = 1.98m Q = 300μC
COUNTS/CHANNEL
CHANNEL
15.07
Ne18 1.88
Ne18 0.0
0
500
1000
1500
20
40
60
80
100
120
140
160
180
200

Figure 29

Angular distribution of neutrons from the $B^{11}(He^3, n)$ reaction leading to the lowest T = 3/2 level in N^{13}. The error bars for points at $\theta_{CM} < 60^{o}$ denote limits of error imposed by background subtraction. For other points the errors are statistical. The smooth curves are calculated using the plane wave theory of Newns (1960). The cutoff radius r = 5.0 f was used in a successful fit of the $B^{11}(t, p)$ reaction (Middleton and Pullen 1964a). Our data require r = 3.75 - 4.0 f. The sensitivity of the plane wave theory to the cutoff radius is graphically demonstrated.
(See page 48)

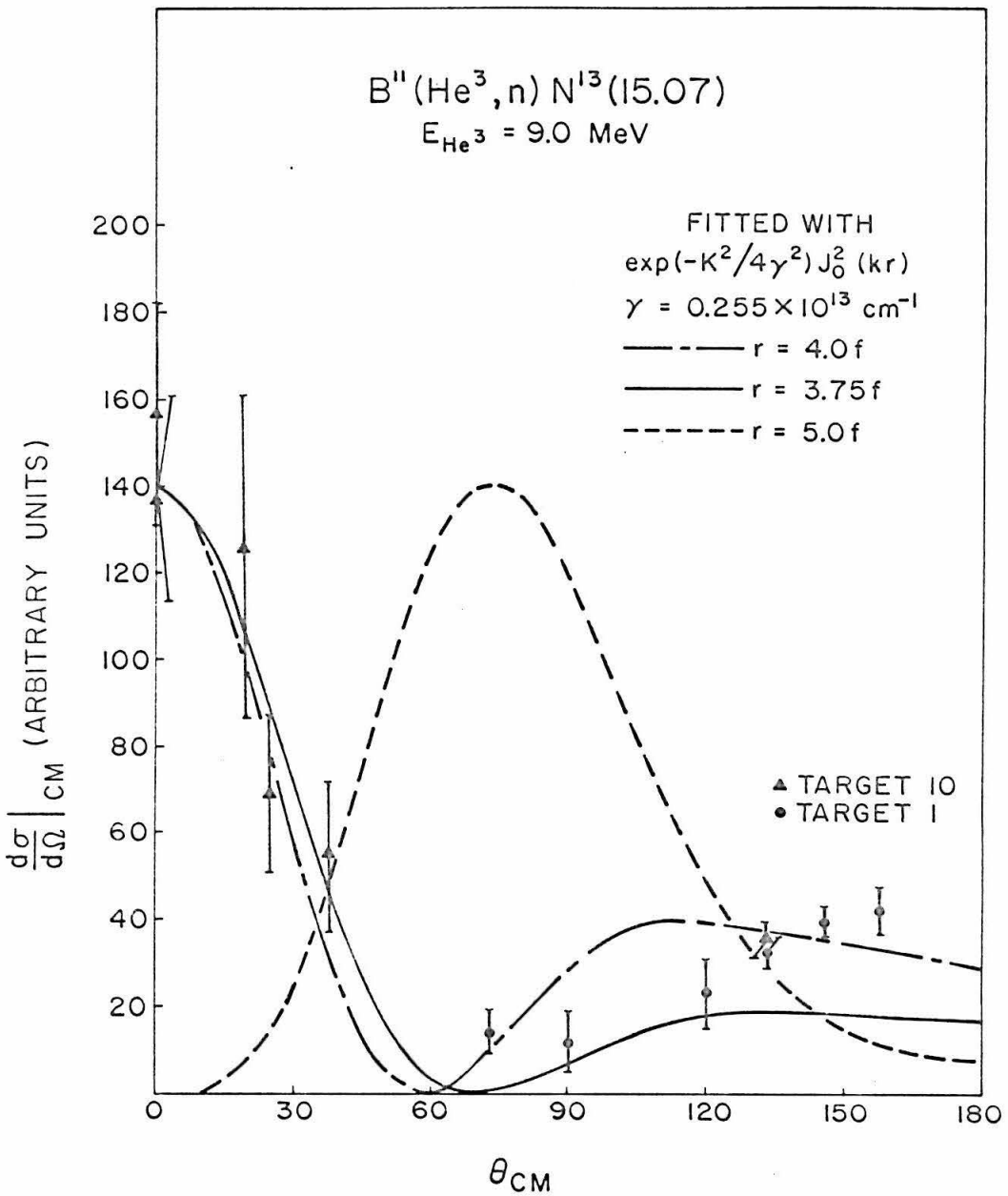
B¹¹(He³, n) N¹³(15.07)
E_He3 = 9.0 MeV
FITTED WITH
exp(-K²/4γ²) J₀² (kr)
γ = 0.255×10¹³ cm⁻¹
r = 4.0f
r = 3.75f
r = 5.0f
▲ TARGET 10
● TARGET 1
dσ/dΩ | CM (ARBITRARY UNITS)
θ CM
0
30
60
90
120
150
180
20
40
60
80
100
120
140
160
180
200

Figure 30

Angular distributions of neutrons corresponding to the unresolved 3.51 and 3.56 MeV states in N^{13}, taken at 9.0 MeV incident energy. Error bars have been omitted because the dominant uncertainty is due to a highly subjective background subtraction. Rather than make a totally arbitrary and meaningless estimate of the background uncertainty, we refer the reader to Figure 19, where he may form his own opinion of our taste in backgrounds. The smooth curve is an L = 0 fit using the same cutoff radius (4.0 f) used in fitting the 15.068 MeV state. The fit to the forward peak is quite good indicating that at forward angles the peak is almost purely due to the $3/2^-$ state at 3.51 MeV. The discrepancy between curve and data at back angles may be due to the presence of neutrons from the 3.56 MeV state. (See page 49)

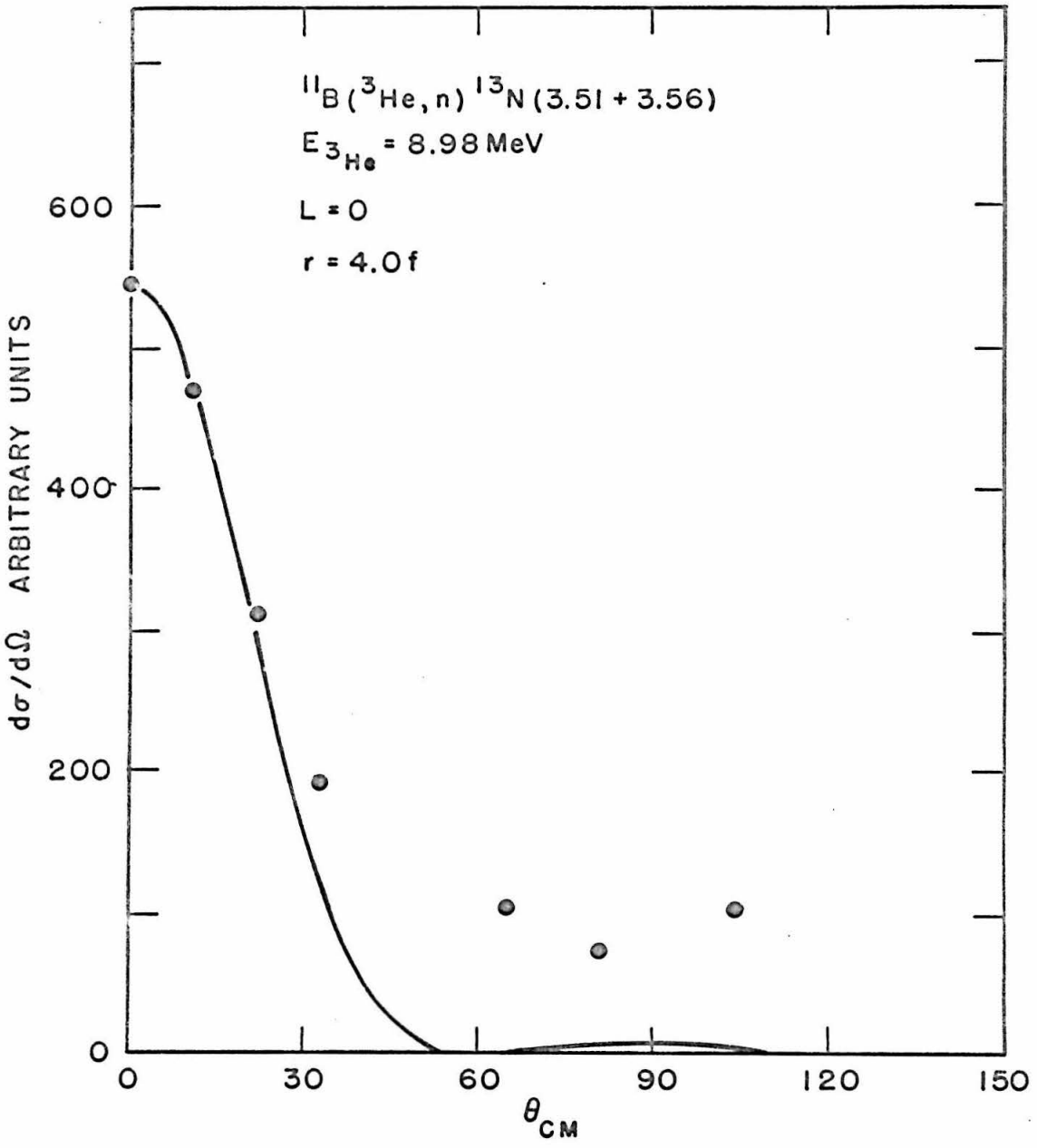
$^{11}B(^{3}He,n)^{13}N(3.51+3.56)$
$E_{^{3}He} = 8.98\,MeV$
L = 0
r = 4.0f
600
400
200
0
0
30
60
90
120
150
θ_{CM}
$d\sigma/d\Omega$ ARBITRARY UNITS

Figure 31

Partial angular distribution of neutrons from the $B^{11}(He^3, n)N^{13}(18.98)$ reaction at an incident energy of 12.5 MeV. The error bars include effects of counting statistics and uncertainties in background subtraction.
(See page 49)

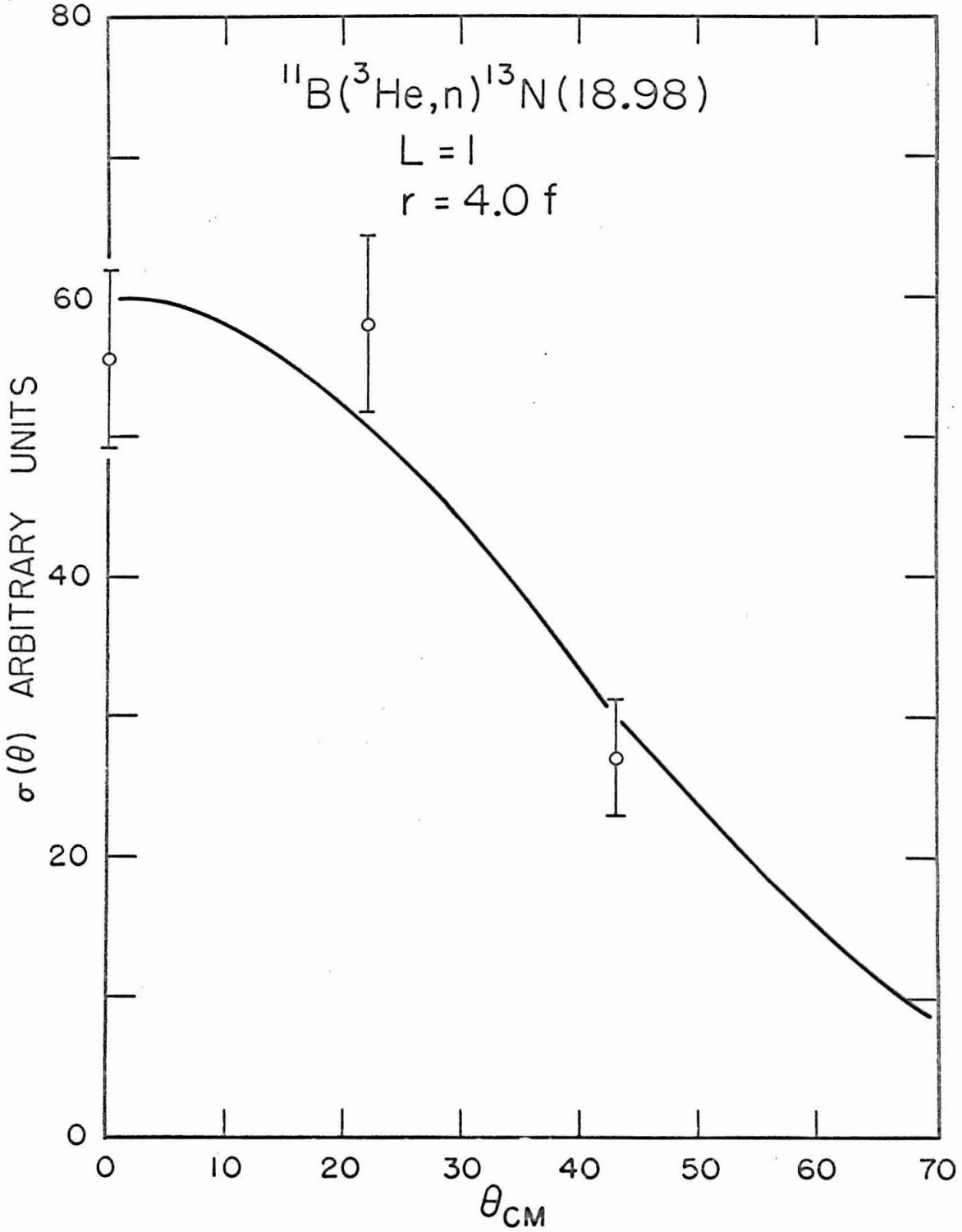
$^{11}B(^{3}He,n)^{13}N(18.98)$
L = 1
r = 4.0 f
80
60
40
20
0
$\sigma(\theta)$ ARBITRARY UNITS
0
10
20
30
40
50
60
70
θ_{CM}

Figure 32

A = 13 isobar diagram. T = 3/2 levels in C^{13} are from Hensley and Barnes (1965, 1966), the O^{13} mass is from Cerny et al., (1966), and the T = 3/2 levels in N^{13} are from the present work. Correspondences which are considered to be well established are indicated by solid lines; those which are tentative are dotted. The correspondences between the (He^3, n) and (He^3, p) results are quite good. In both cases the lowest T = 3/2 levels are populated very strongly. The 18.67 and 19.13 MeV states in C^{13} are populated relatively strongly and presumably correspond to the 18.44 and 18.98 MeV states in N^{13}. In the B^{11}(He^3, p) reaction the 18.47 MeV state is quite weak and the 18.70 MeV state is seen only as a shoulder on the 18.67 MeV level. This is consistent with the suggestion that the N^{13} 18.44 MeV state may be an unresolved doublet. (See page 51)

T=3/2 ISOBARS-MASS 13

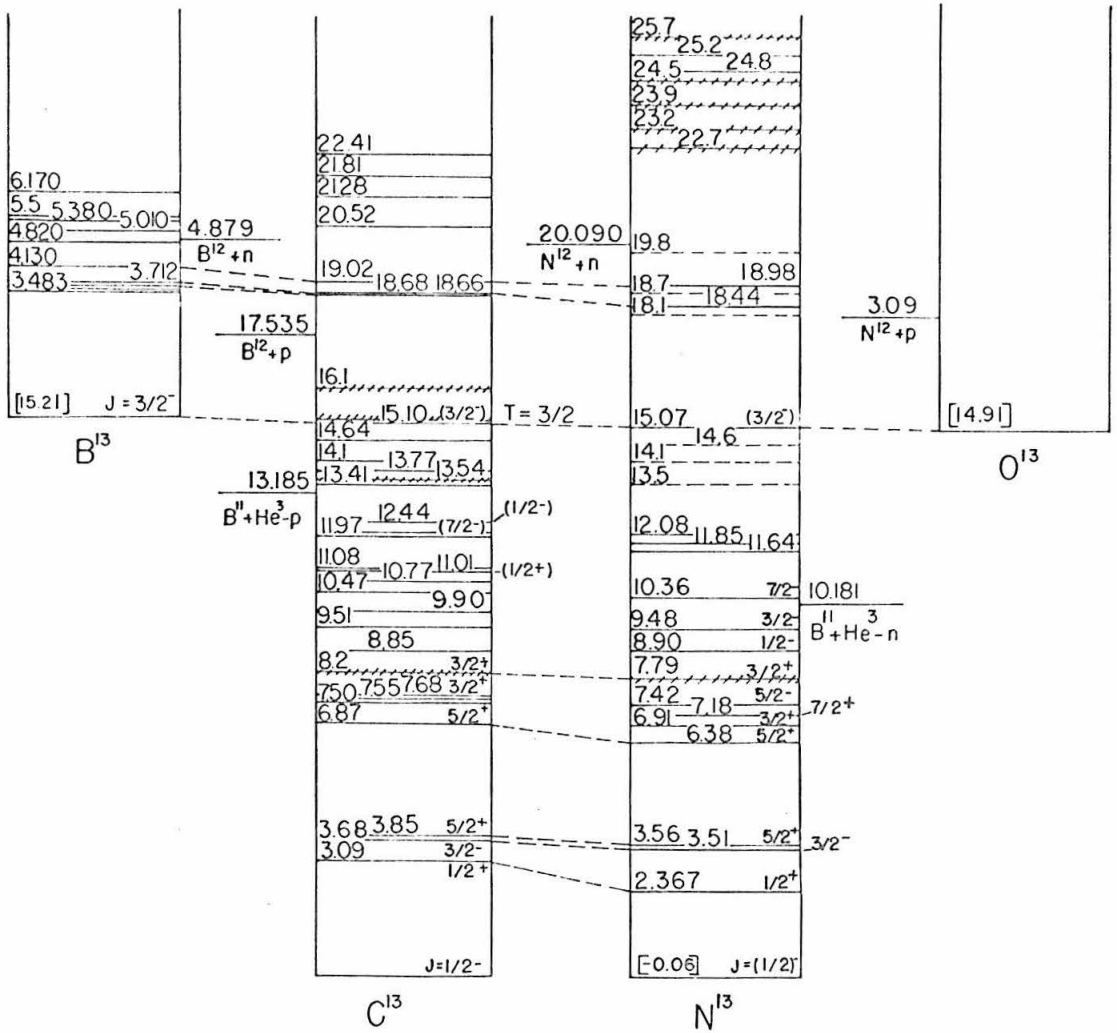

Figure 33

Determination of energy loss in a 5000 Å Ni entrance foil for the gas cell. The yield of high energy gamma radiation is plotted against nominal proton energy, as the beam energy is swept over the 872 keV $F^{19}(p,\alpha\gamma)$ resonance. The energy loss in the foil was taken to be the displacement of the centroid of the resonance when the foil was placed ahead of a thin fluorine target. (See pages 56 and

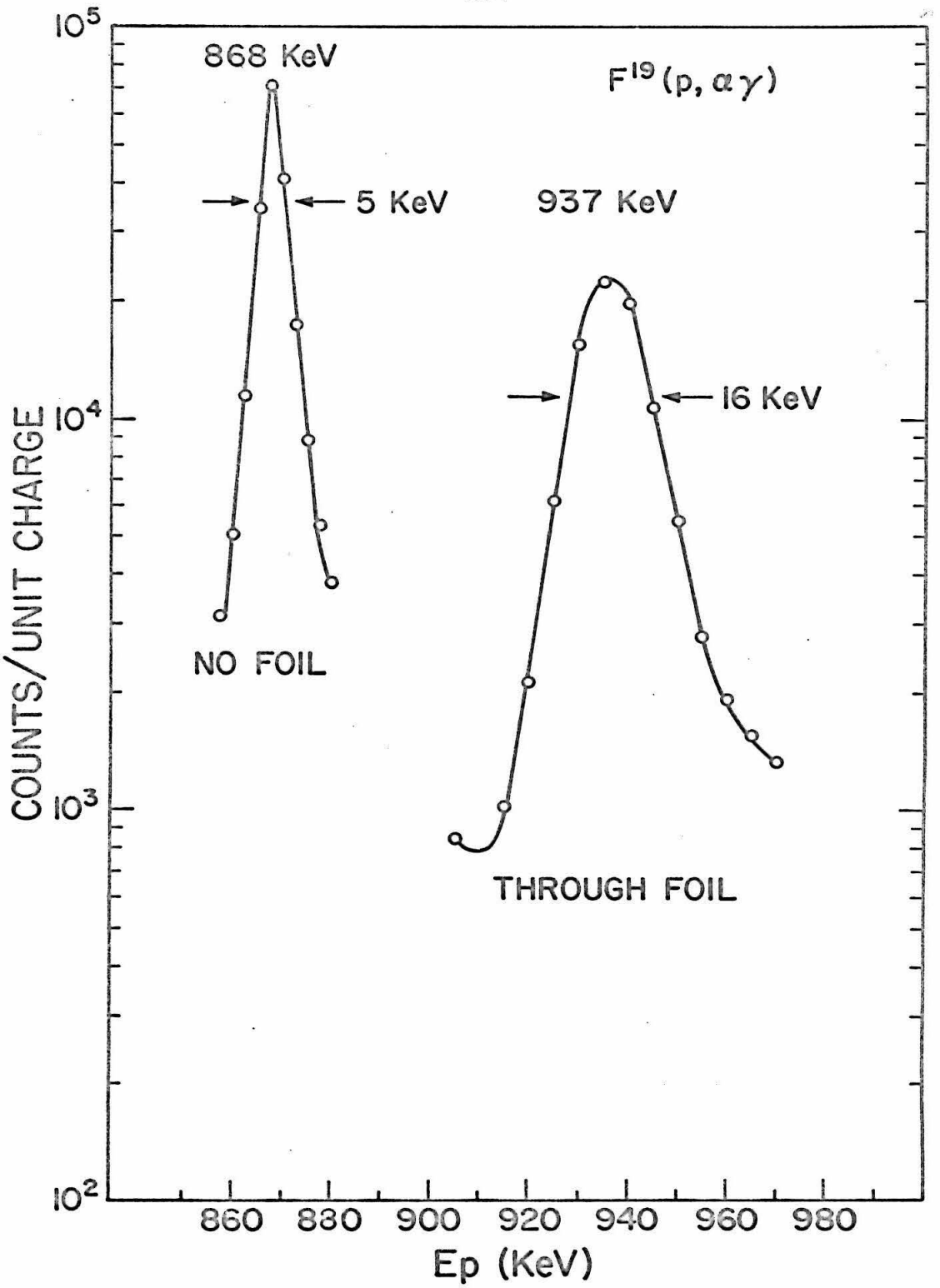
868 KeV
$F^{19}(p, \alpha\gamma)$
5 KeV
937 KeV
16 KeV
NO FOIL
THROUGH FOIL
COUNTS/UNIT CHARGE
10^5
10^4
10^3
10^2
860
880
900
920
940
960
980
Ep (KeV)

Figure 34

Time spectrum of neutrons from the reaction $N^{15}(He^3, n)$ at 10.498 MeV incident energy. The time scale was calibrated using the $N^{15}(\alpha, n)F^{18}(0.0)$ reaction and is approximately 1 ns/ch. The T = 3/2 levels in F^{17} are labelled by their excitation energy. (See page 56)

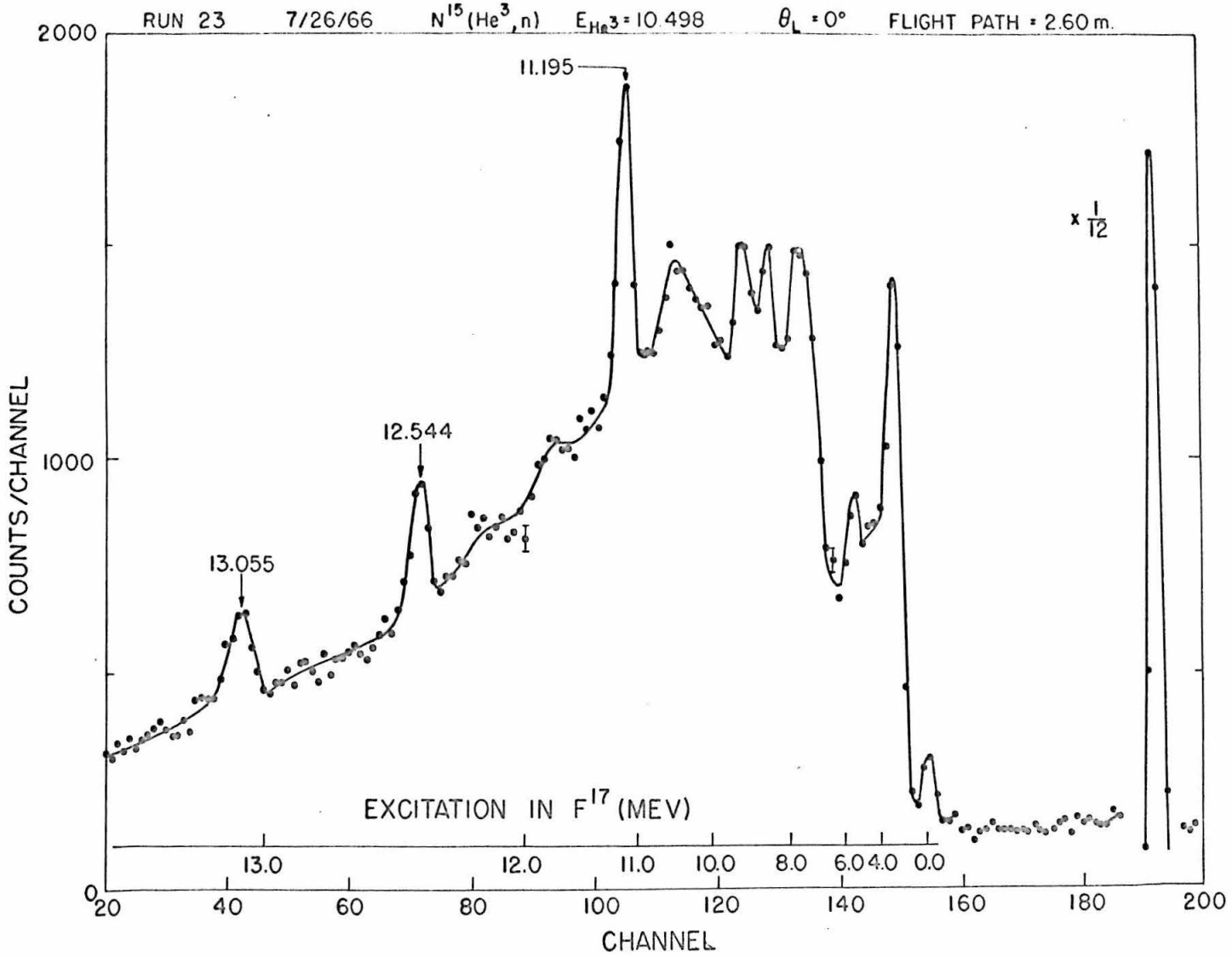
RUN 23 7/26/66 N15(He3,n) EHe3 = 10.498 θL = 0° FLIGHT PATH = 2.60 m.
2000
1000
0
COUNTS/CHANNEL
11.195
12.544
13.055
x 1/12
EXCITATION IN F17 (MEV)
13.0
12.0
11.0
10.0
8.0
6.0
4.0
0.0
20
40
60
80
100
120
140
160
180
200
CHANNEL

Figure 35

Time spectrum of neutrons from the $N^{15}(He^3, n)$ reaction at 11.88 MeV incident energy. The T = 3/2 levels in F^{17} are labelled by their excitation energy. The time scale is approximately 1 ns/ch. (See page 57)

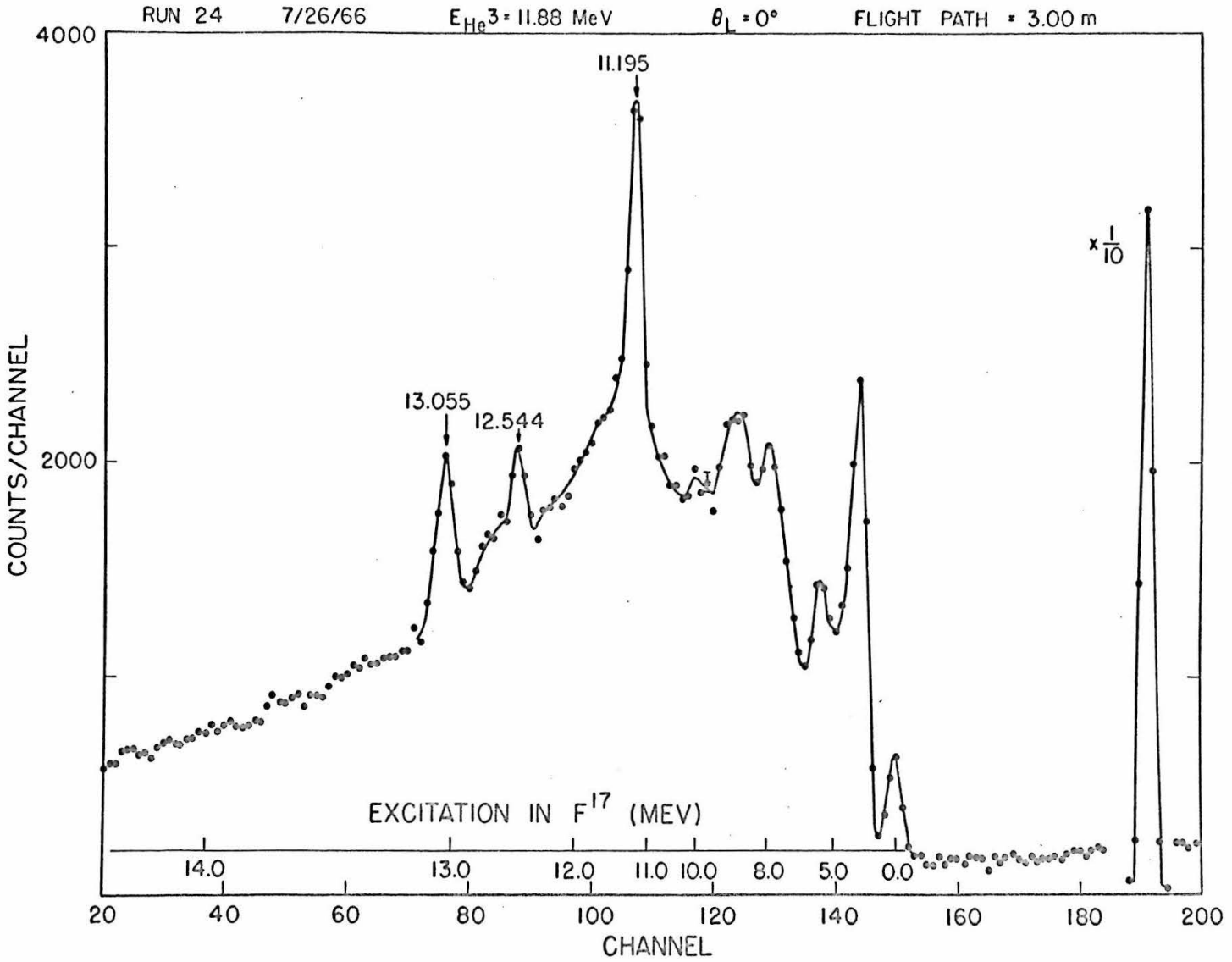
RUN 24 7/26/66 E_{He^3} = 11.88 MeV θ_L = 0° FLIGHT PATH = 3.00 m
4000
2000
COUNTS/CHANNEL
11.195
13.055
12.544
x 1/10
EXCITATION IN F^{17} (MEV)
14.0
13.0
12.0
11.0
10.0
8.0
5.0
0.0
20
40
60
80
100
120
140
160
180
200
CHANNEL

Figure 36

Time spectrum of neutrons from the $N^{15}(He^3, n)$ reaction at 8.255 MeV incident energy. This spectrum was used in a determination of the excitation energy of the lowest T = 3/2 state in F^{17}. The time scale is approximately 1 ns/ch and was calibrated using the spectrum shown in Figure 37. The peak marked SP (spurious) is due to gamma rays from the out-of-phase beam burst. Other peaks are identified with known levels in F^{17}. (See page 58)

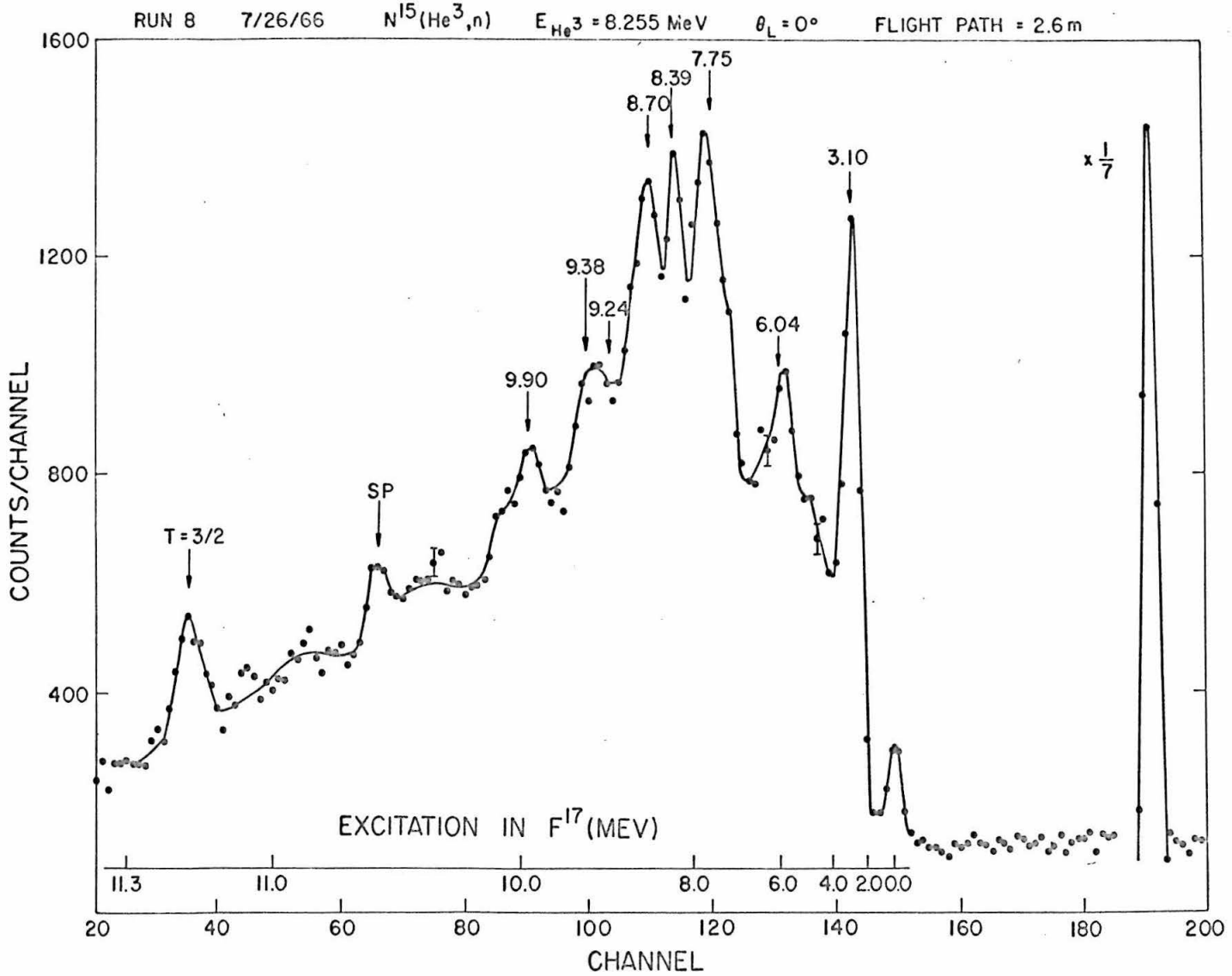
RUN 8 7/26/66 N15(He3,n) E He3 = 8.255 MeV θL = 0° FLIGHT PATH = 2.6 m
COUNTS/CHANNEL
1600
1200
800
400
T = 3/2
SP
9.90
9.38
9.24
8.70
8.39
7.75
6.04
3.10
x 1/7
EXCITATION IN F17 (MEV)
11.3
11.0
10.0
8.0
6.0
4.0
2.0
0.0
20
40
60
80
100
120
140
160
180
200
CHANNEL

Figure 37

Time spectrum from the $N^{15}(\alpha, n)F^{17}(0.0)$ reaction at 8.915 MeV incident energy. This spectrum was used to calibrate the time scale in the spectrum displayed in Figure 36. (See page 58)

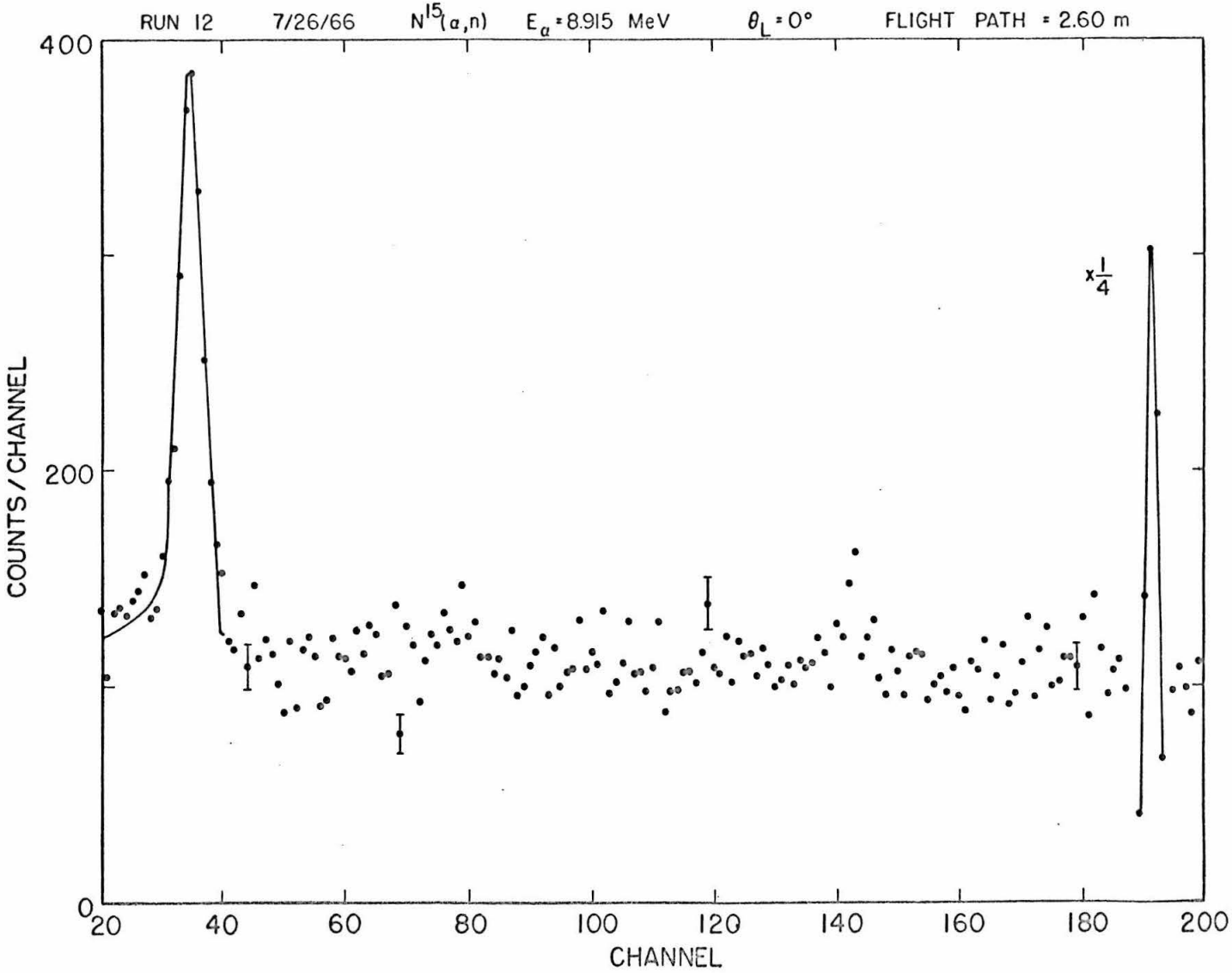
RUN 12 7/26/66 $N^{15}(\alpha,n)$ E_α = 8.915 MeV θ_L = 0° FLIGHT PATH = 2.60 m
COUNTS / CHANNEL
CHANNEL
x 1/4
0
200
400
20
40
60
80
100
120
140
160
180
200

Figure 38

L = 0 angular distribution of neutrons from the $N^{15}(He^3, n)F^{17}(11.195)$ reaction at 10.36 MeV incident energy. In addition to the errors denoted by the flags there is an estimated uncertainty of ± 10% in the absolute normalization. The curve is a DWBA calculation with only the normalization treated as a free parameter. (See page 60.)

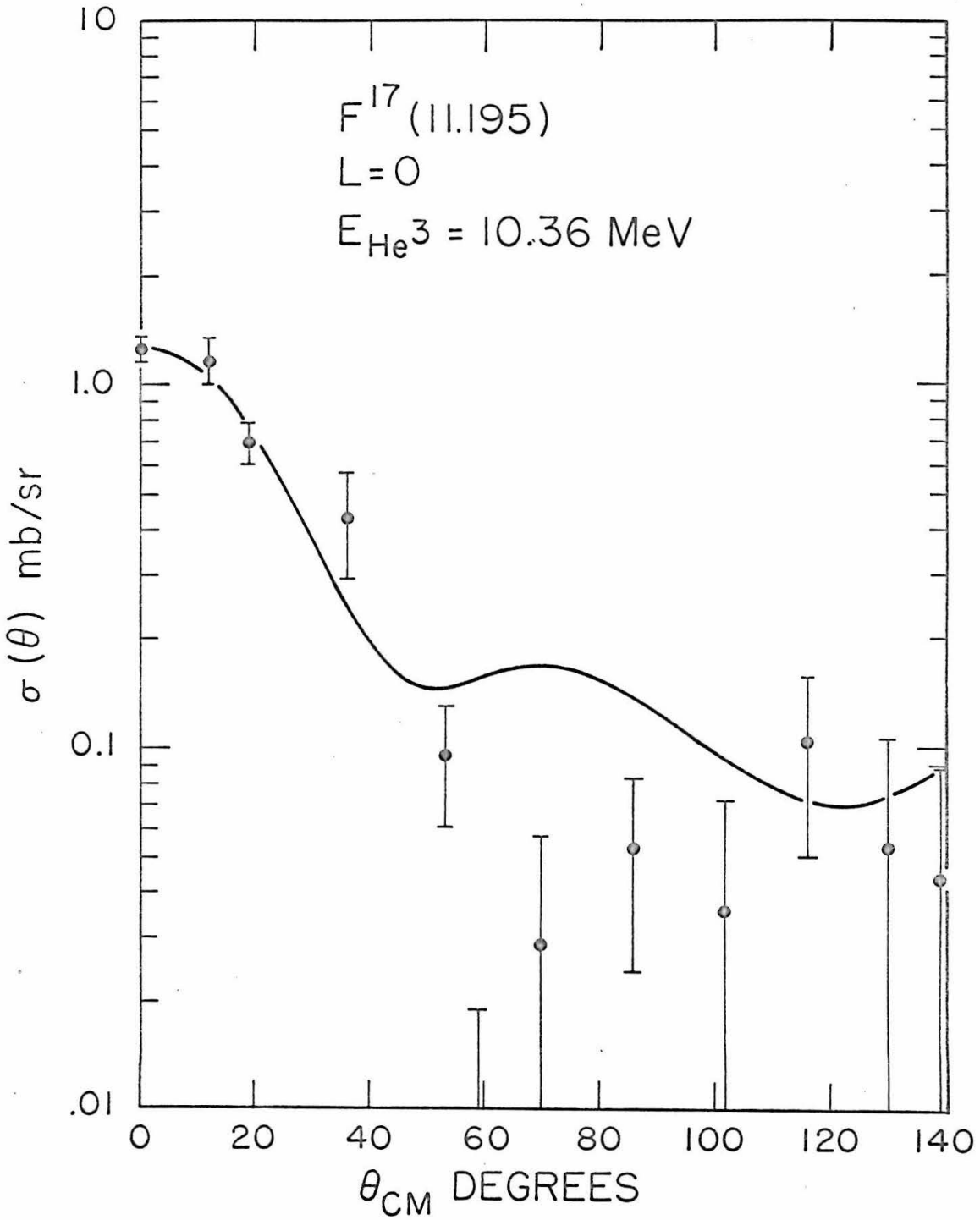
10
1.0
0.1
.01
F^{17} (11.195)
L = 0
E_{He^3} = 10.36 MeV
σ (θ) mb/sr
0
20
40
60
80
100
120
140
θ_{CM} DEGREES

Figure 39

L = 0 angular distributions of neutrons from the reactions $N^{15}(He^3, n)F^{17}(11.195)$ at $E_{He^3} = 11.88$ MeV, and $O^{16}(He^3, n)Ne^{18}(0.0)$ at $E_{He^3} = 10.50$ MeV. In addition to the errors denoted by the flags there is an estimated uncertainty of ± 10% in the absolute normalization. Since both transitions may be thought of as the L = 0 capture of two protons into an empty sd shell, the F^{17} and Ne^{18} angular distributions are expected to be very similar. The curves are DWBA calculations with only the normalizations treated as free parameters.
(See page 60)

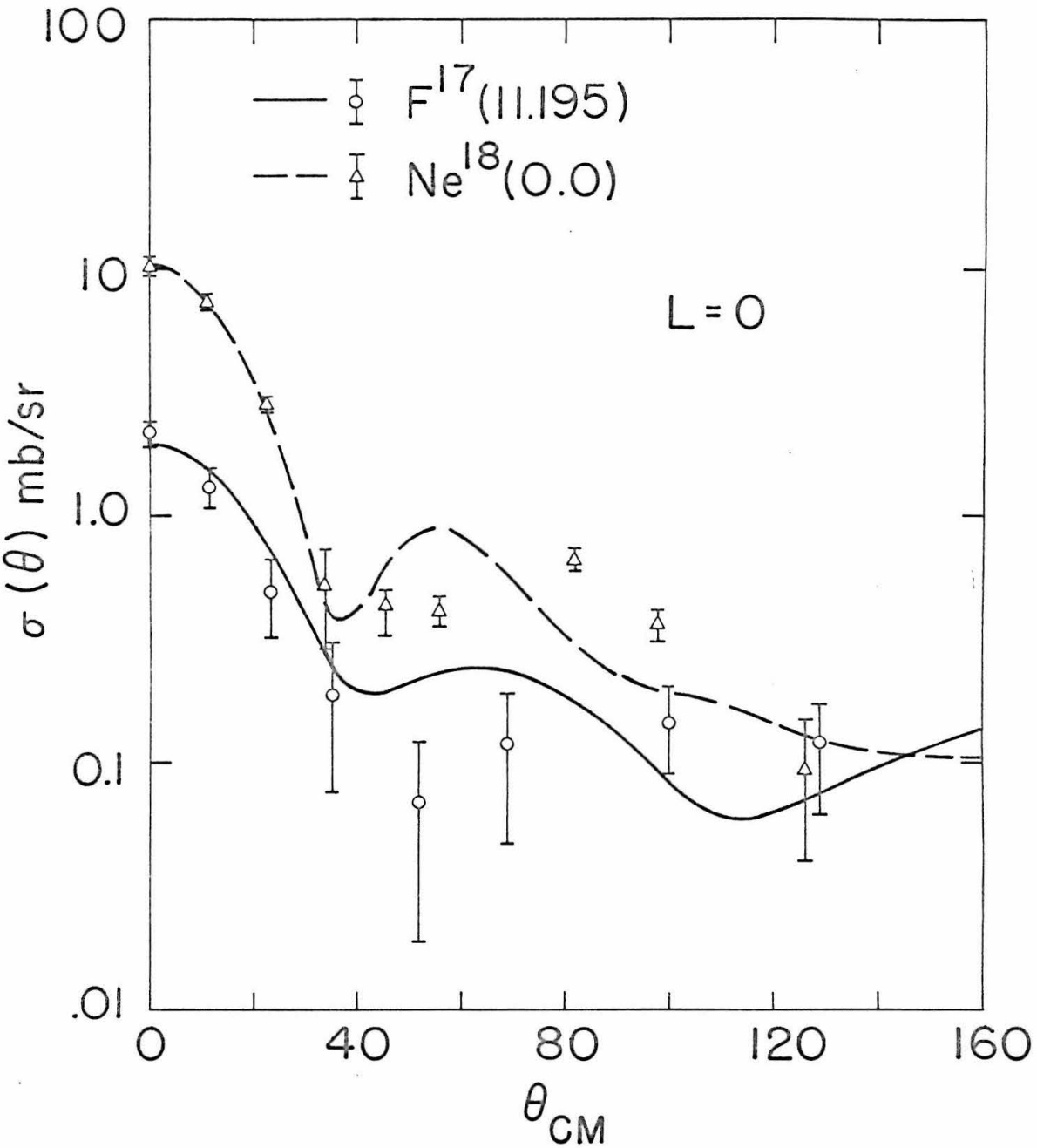
100
10
1.0
0.1
.01
$\sigma(\theta)$ mb/sr
F^{17}(11.195)
Ne^{18}(0.0)
L = 0
0
40
80
120
160
θ_{CM}

Figure 40

L = 2 angular distributions of neutrons from the reactions $N^{15}(He^3, n)F^{17}(12.540)$ at E_{He^3} = 11.88 MeV and $O^{16}(He^3, n)Ne^{18}(1.88)$ at E_{He^3} = 10.50 MeV. In addition to the errors denoted by the flags there is an estimated uncertainty of ± 10% in the absolute normalization. The curves are DWBA calculations with only the normalizations treated as free parameters. Note that in both cases the DWBA curve fails to reproduce the pronounced minimum at 0^o. Since both transitions may be thought of as the L = 2 capture of two protons into an empty sd shell, the F^{17} and Ne^{18} angular distributions are expected to be very similar. (See page 60)

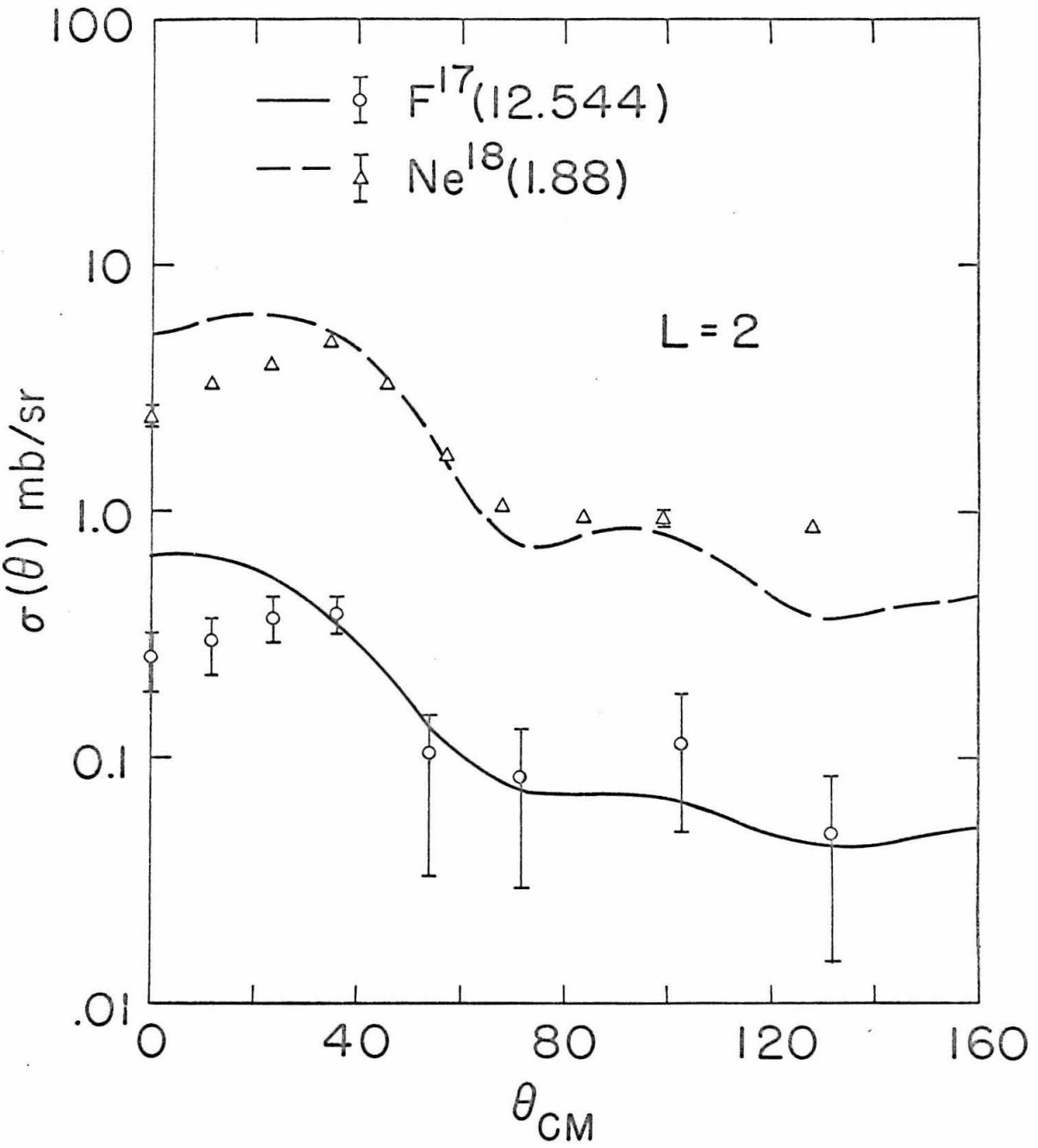
100
10
1.0
0.1
.01
$\sigma(\theta)$ mb/sr
F^{17}(12.544)
Ne^{18}(1.88)
L = 2
0
40
80
120
160
θ_{CM}

Figure 41

Angular distribution of neutrons from the $N^{15}(He^3, n)F^{17}(13.059)$ at 11.88 MeV incident energy. In addition to the errors denoted by the flags there is an estimated uncertainty of ± 10% in the absolute normalization. This level is unbound to diproton decay and cannot be treated by our DWBA code. (See page 60)

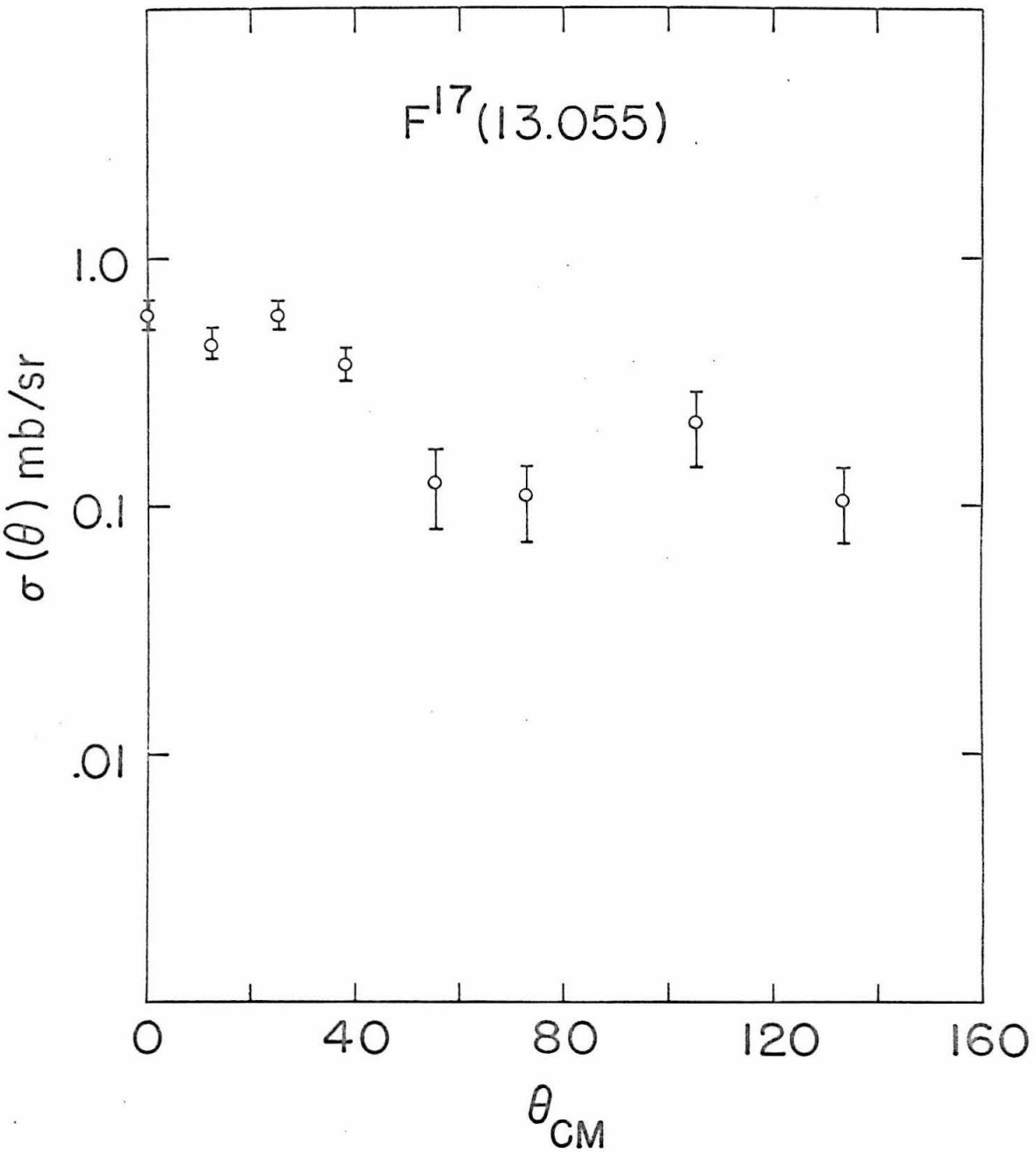
F17(13.055)
1.0
0.1
.01
σ (θ) mb/sr
0
40
80
120
160
θCM

Figure 42

Isobar diagram for the A = 17 nuclei. The notation and Coulomb corrections are described in the caption to Figure 18. For similicity only the low lying T = 1/2 levels are shown. The T = 1/2 levels are taken from Lauritsen and Ajzenberg-Selove (1962), except for the $5/2^+$ assignments to the 3.8 MeV states in O^{17} (Broude et al., 1963) and F^{17} (Segel et al., 1963). The T = 3/2 levels in O^{17} have been taken from studies of the $N^{15}(He^3, p)$ and $O^{18}(He^3, \alpha)$ reactions by Hensley and Barnes (1966). The mass indicated for Ne^{17} was estimated using the quadratic mass law, which predicts a mass excess for Ne^{17} of 16.478 ± .032 MeV. (See page 62.)

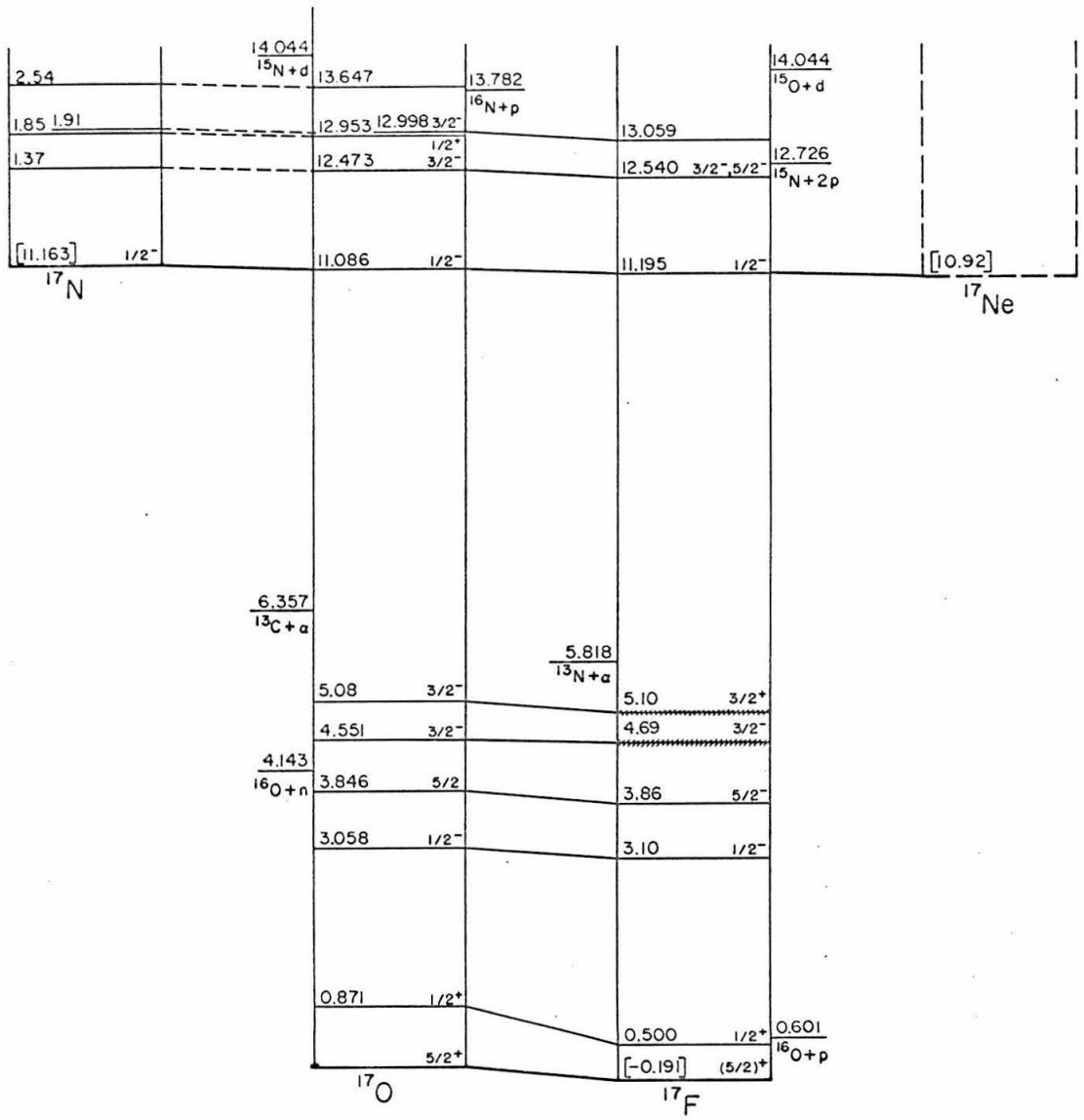
14.044
15N+d
2.54
1.85 1.91
1.37
[11.163] 1/2⁻
17N
13.647
12.953 12.998 3/2⁻
1/2⁺
12.473 3/2⁻
11.086 1/2⁻
13.782
16N+p
13.059
12.540 3/2⁻,5/2⁻
11.195 1/2⁻
14.044
15O+d
12.726
15N+2p
[10.92]
17Ne
6.357
13C+α
5.08 3/2⁻
4.551 3/2⁻
4.143
16O+n
3.846 5/2
3.058 1/2⁻
0.871 1/2⁺
5/2⁺
17O
5.818
13N+α
5.10 3/2⁺
4.69 3/2⁻
3.86 5/2⁻
3.10 1/2⁻
0.500 1/2⁺
[-0.191] (5/2)⁺
17F
0.601
16O+p

Figure 43

Time spectrum of neutrons from the $O^{18}(He^3, n)$ reaction at 5.204 MeV incident energy. This spectrum was used in determinations of the excitation energy and width of the lowest T = 2 state in Ne^{20}. The time scale was calibrated using the $O^{16}(He^3, n)Ne^{18}(0.0)$ reaction and is roughly 1 ns/ch. (See pages 67 and 69.)

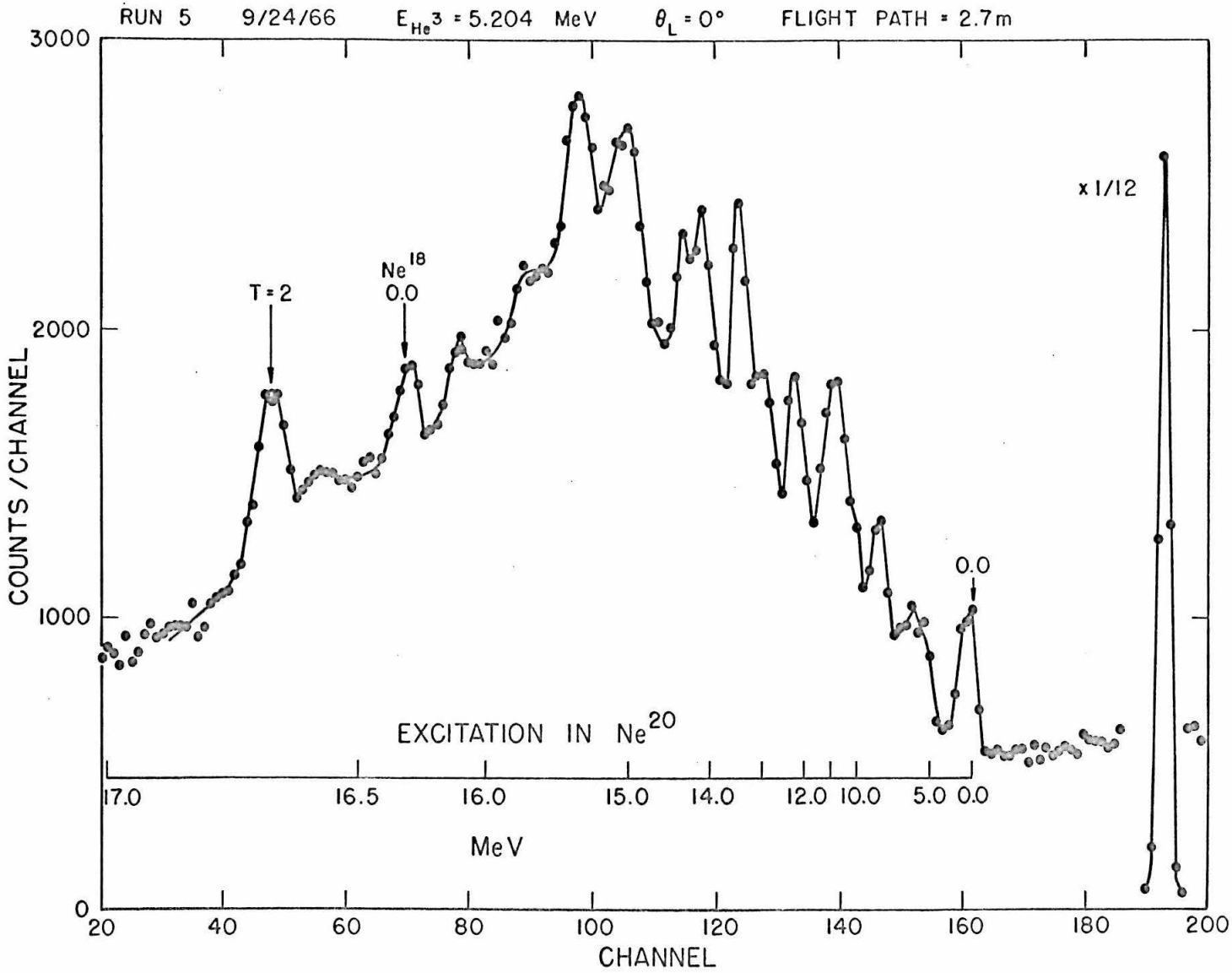
RUN 5 9/24/66 E_{He^3} = 5.204 MeV θ_L = 0° FLIGHT PATH = 2.7m
COUNTS /CHANNEL
CHANNEL
T = 2
Ne^{18} 0.0
0.0
x 1/12
EXCITATION IN Ne^{20}
17.0 16.5 16.0 15.0 14.0 12.0 10.0 5.0 0.0
MeV
0 1000 2000 3000
20 40 60 80 100 120 140 160 180 200

Figure 44

Time spectrum from the $O^{18}(He^3, n)$ reaction at 5.714 MeV incident energy. The lowest T = 2 level in Ne^{20} is quite prominent at this incident energy and appears to be on top of a broad "bump". This "bump" remains prominent at angles up to 45^{o}, although the intensity of the T = 2 peak diminishes. The dotted line indicates our somewhat arbitrary choice of background subtraction. It is typical of those used in forming the angular distribution of Figure 49 . The sloping background to the right of the unresolved ground and first excited state group is composed of neutrons having a flight time, t, longer than one RF period, τ, and which therefore have an apparent flight time $t' = t - \tau$. The time scale is approximately 1 ns/ch. (See pages 67 and 71.)

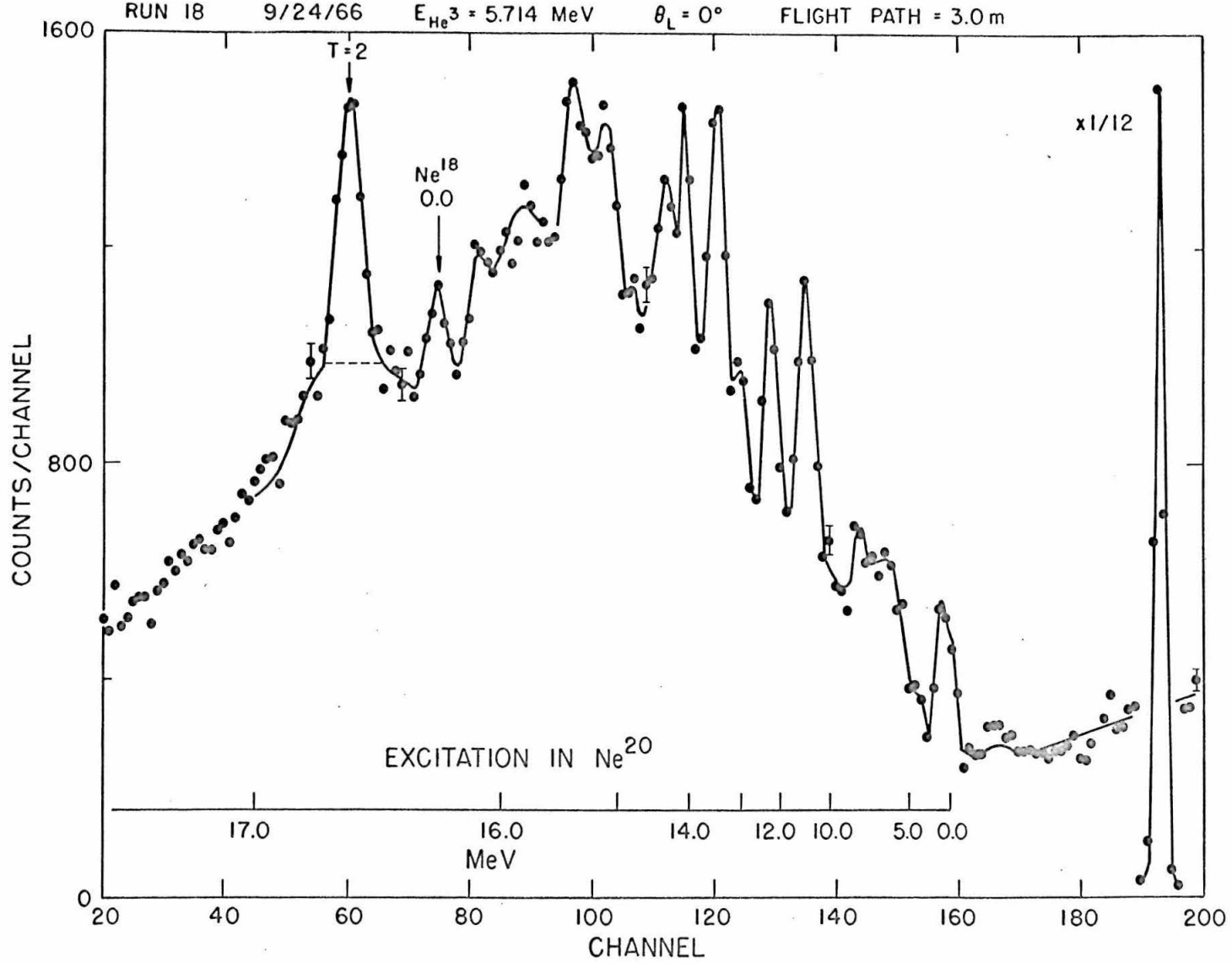
RUN 18 9/24/66 E_{He^3} = 5.714 MeV θ_L = 0° FLIGHT PATH = 3.0 m
T=2
Ne^{18} 0.0
x1/12
COUNTS/CHANNEL
1600
800
0
EXCITATION IN Ne^{20}
17.0
16.0
14.0
12.0
10.0
5.0
0.0
MeV
20
40
60
80
100
120
140
160
180
200
CHANNEL

Figure 45

Time spectrum of neutrons from the $O^{18}(He^3, n)$ reaction at an incident energy of 6.515 MeV. The lowest T = 2 level in Ne^{20} is clearly visible above the intense continuum due to multibody decays. The time scale is approximately 1 ns/ch. (See page 67.)

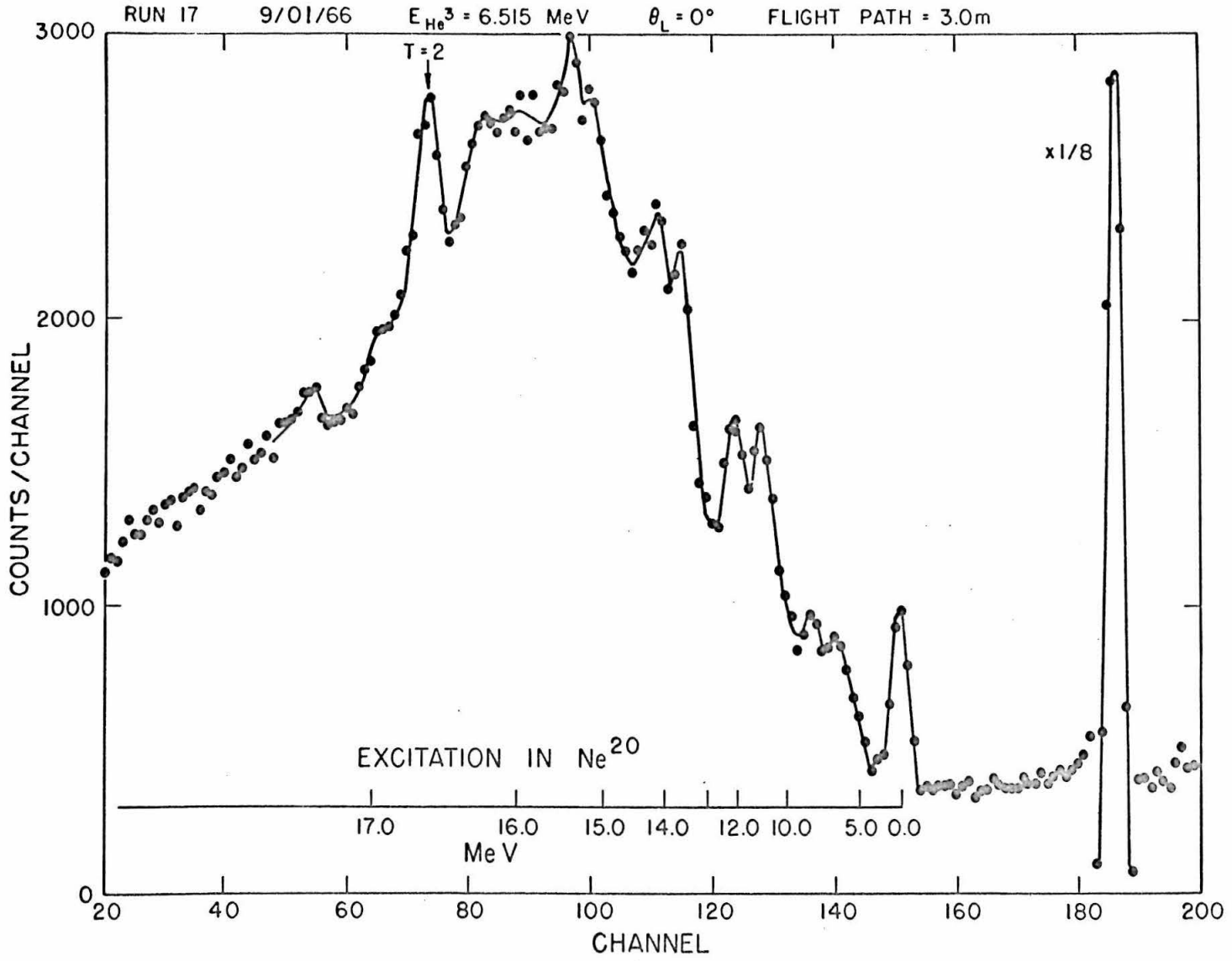
RUN 17 9/01/66 E_{He^3} = 6.515 MeV θ_L = 0° FLIGHT PATH = 3.0m
T = 2
x1/8
COUNTS / CHANNEL
CHANNEL
EXCITATION IN Ne^{20}
17.0 16.0 15.0 14.0 12.0 10.0 5.0 0.0
MeV
0
1000
2000
3000
20 40 60 80 100 120 140 160 180 200

Figure 46

Time spectrum of neutrons from the $O^{18}(He^3, n)$ reaction at 9.01 MeV incident energy. The lowest T = 2 state is labelled; the arrow labelled A marks the excitation of the 18.5 MeV state reported by Cerny et al., (1964). This state is not seen in our spectra. At this incident energy the intense continuum is peaked at an excitation in Ne^{20} close to that of the lowest T = 2 state. (See page 67.)

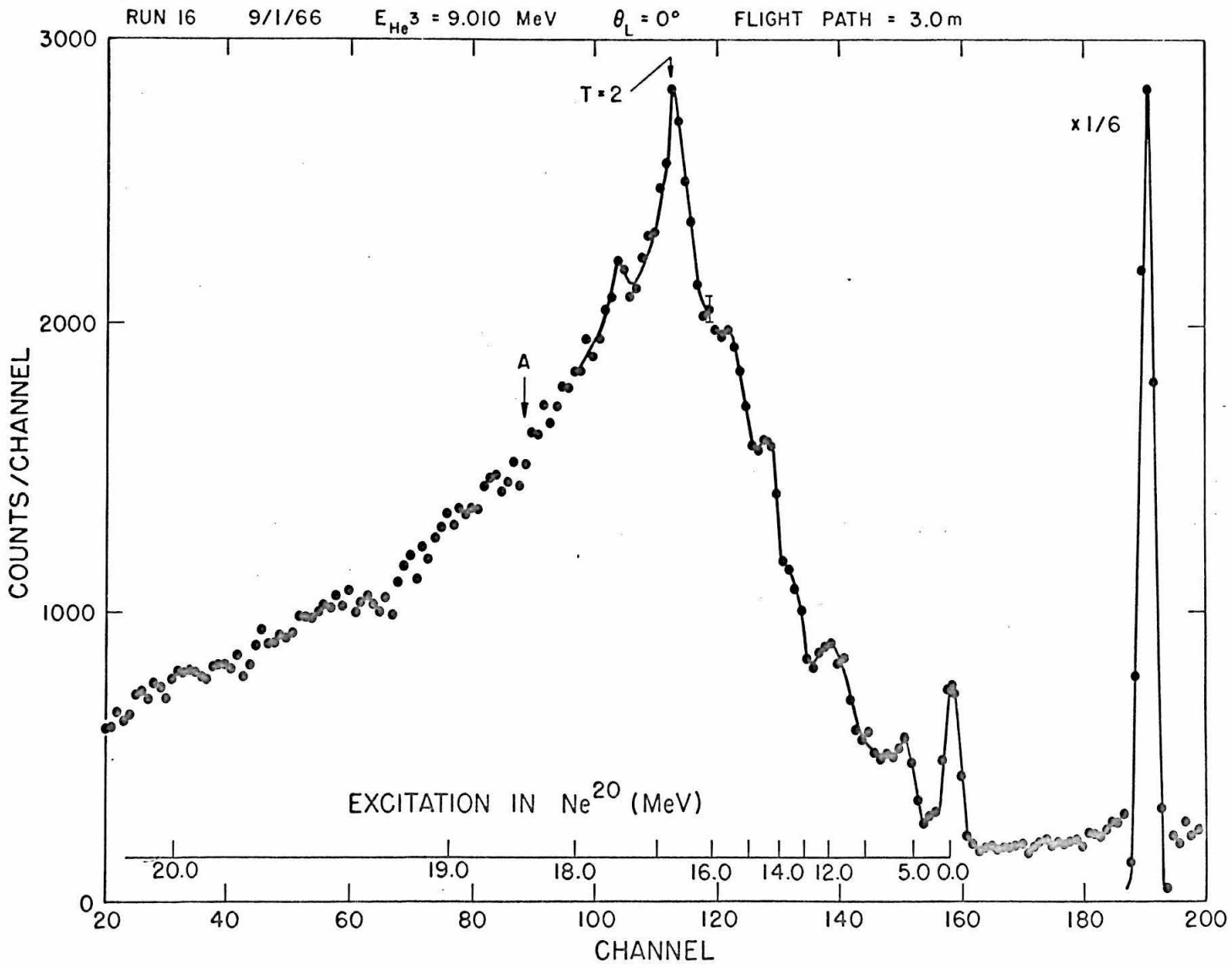
RUN 16 9/1/66 E_{He^3} = 9.010 MeV θ_L = 0° FLIGHT PATH = 3.0 m
T = 2
A
x 1/6
COUNTS/CHANNEL
CHANNEL
EXCITATION IN Ne^{20} (MeV)
20.0
19.0
18.0
16.0
14.0
12.0
5.0
0.0
0
1000
2000
3000
20
40
60
80
100
120
140
160
180
200

Figure 47

Goodness of fit of (He^3, n) Q-values obtained at $\theta_L = 0^\circ$, 10°, 20°, and 30° to a constant versus assumed target mass. The errors used in calculating the goodness of fit were not statistical, but taken from an estimate of the energy uncertainty. Hence the quantity "chi-squared" while a measure of relative goodness of fit, has no interpretation in terms of probabilities. From this graph we infer that the reaction was produced by a target having $16 \leq A \leq 26$. (See page 67.)

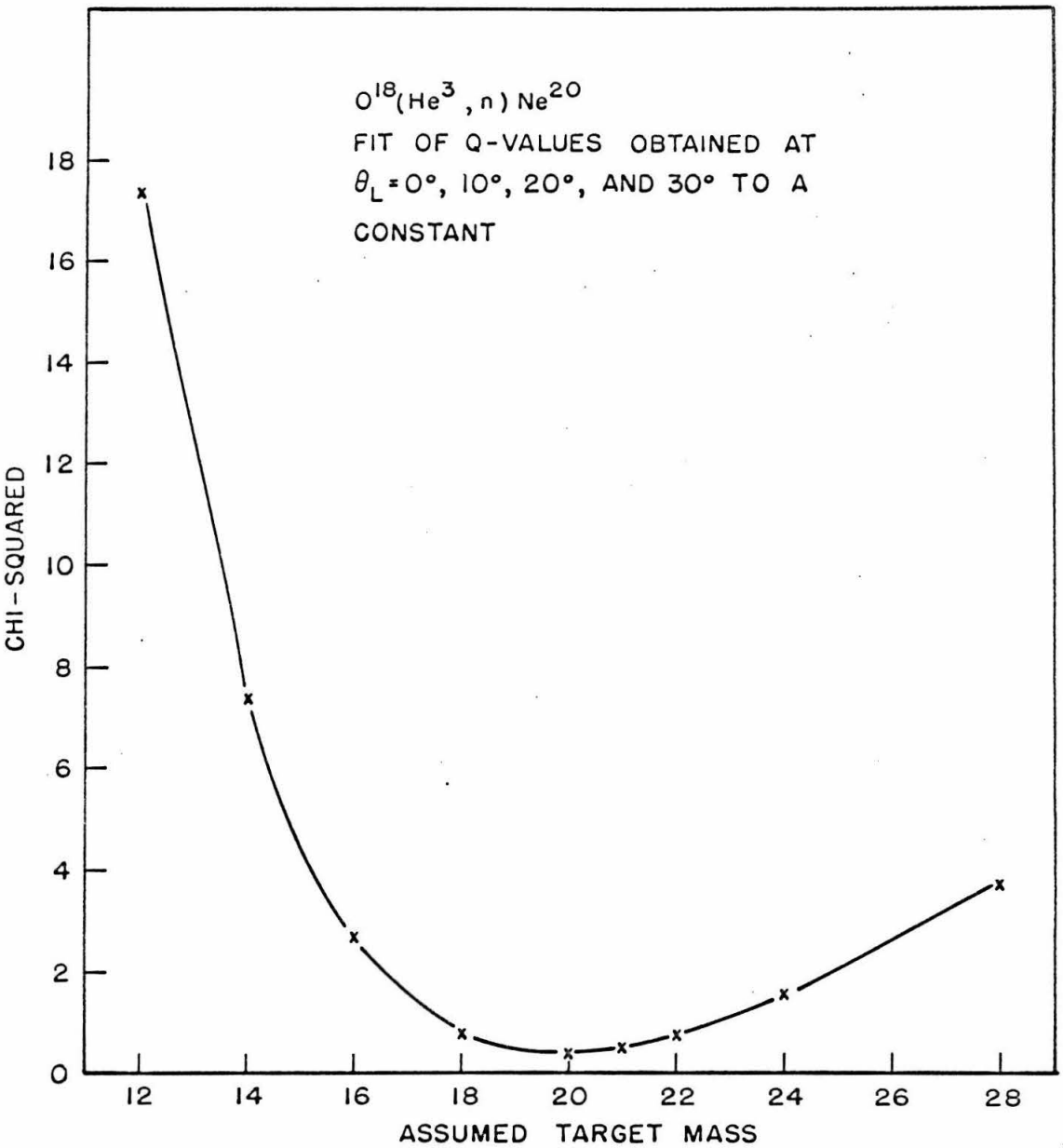
$O^{18}(He^3, n)Ne^{20}$
FIT OF Q-VALUES OBTAINED AT
$\theta_L = 0°$, 10°, 20°, AND 30° TO A
CONSTANT
CHI-SQUARED
0
2
4
6
8
10
12
14
16
18
12
14
16
18
20
22
24
26
28
ASSUMED TARGET MASS

Figure 48

In the upper right we have plotted chi-square as a function of the assumed intrinsic width of the lowest T = 2 state in Ne^{20}. The procedure for calculating the neutron line shape is discussed on page 70. Note the offset scale on the chi-square axis. In the lower part of this figure we have plotted the line shape giving the best fit to the experimental points minus a linear background.

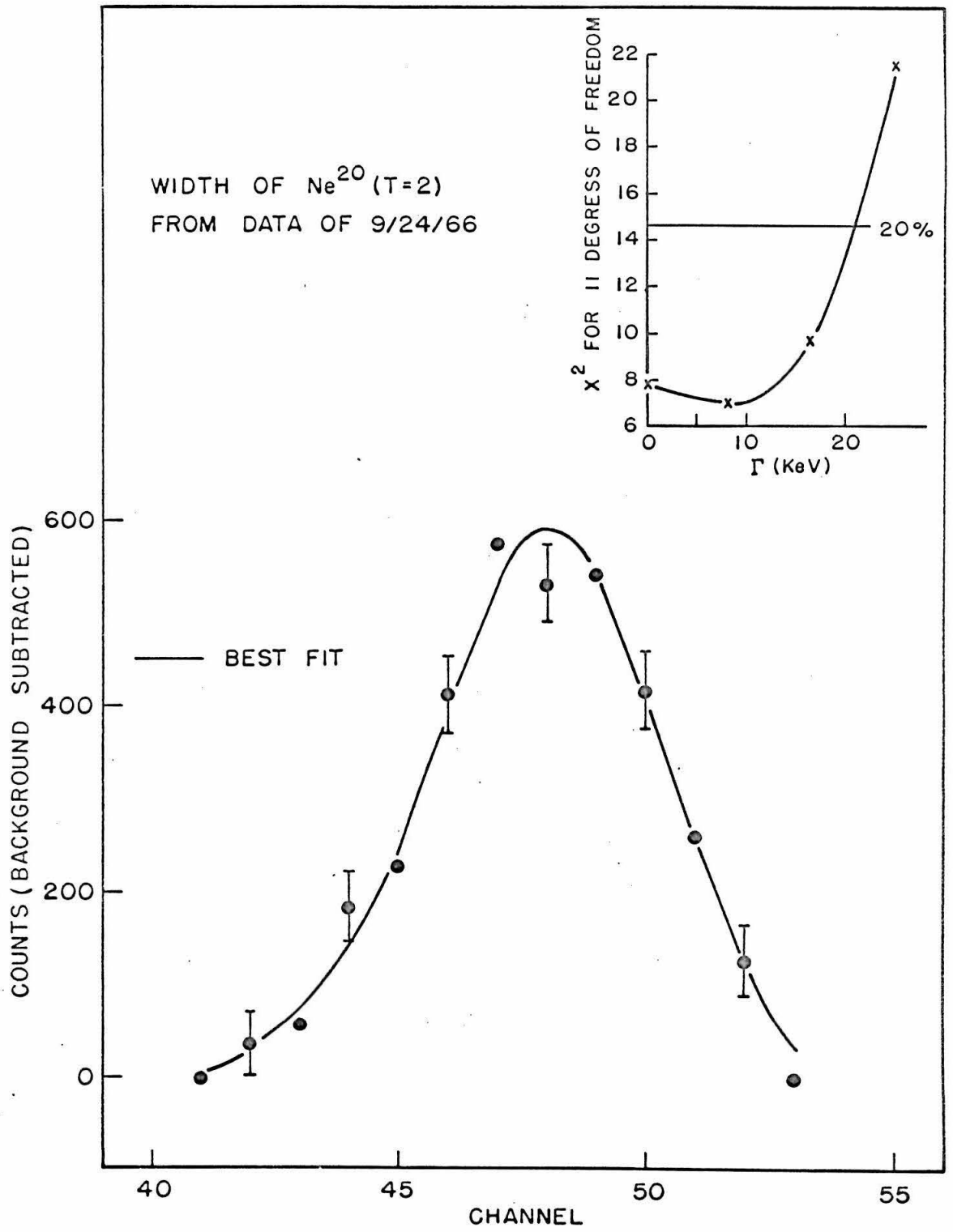
WIDTH OF Ne^{20} (T=2)
FROM DATA OF 9/24/66
χ^2 FOR 11 DEGRESS OF FREEDOM
22
20
18
16
14
12
10
8
6
20%
0
10
20
Γ (KeV)
BEST FIT
COUNTS (BACKGROUND SUBTRACTED)
600
400
200
0
40
45
50
55
CHANNEL

Figure 49

Angular distribution of neutrons from the reaction $O^{18}(He^3, n)Ne^{20}(16.730)$ at 5.70 MeV incident energy. In addition to the errors denoted by the flags there is an estimated uncertainty of $\pm$ 10% in the absolute normalization. (See page 71.)

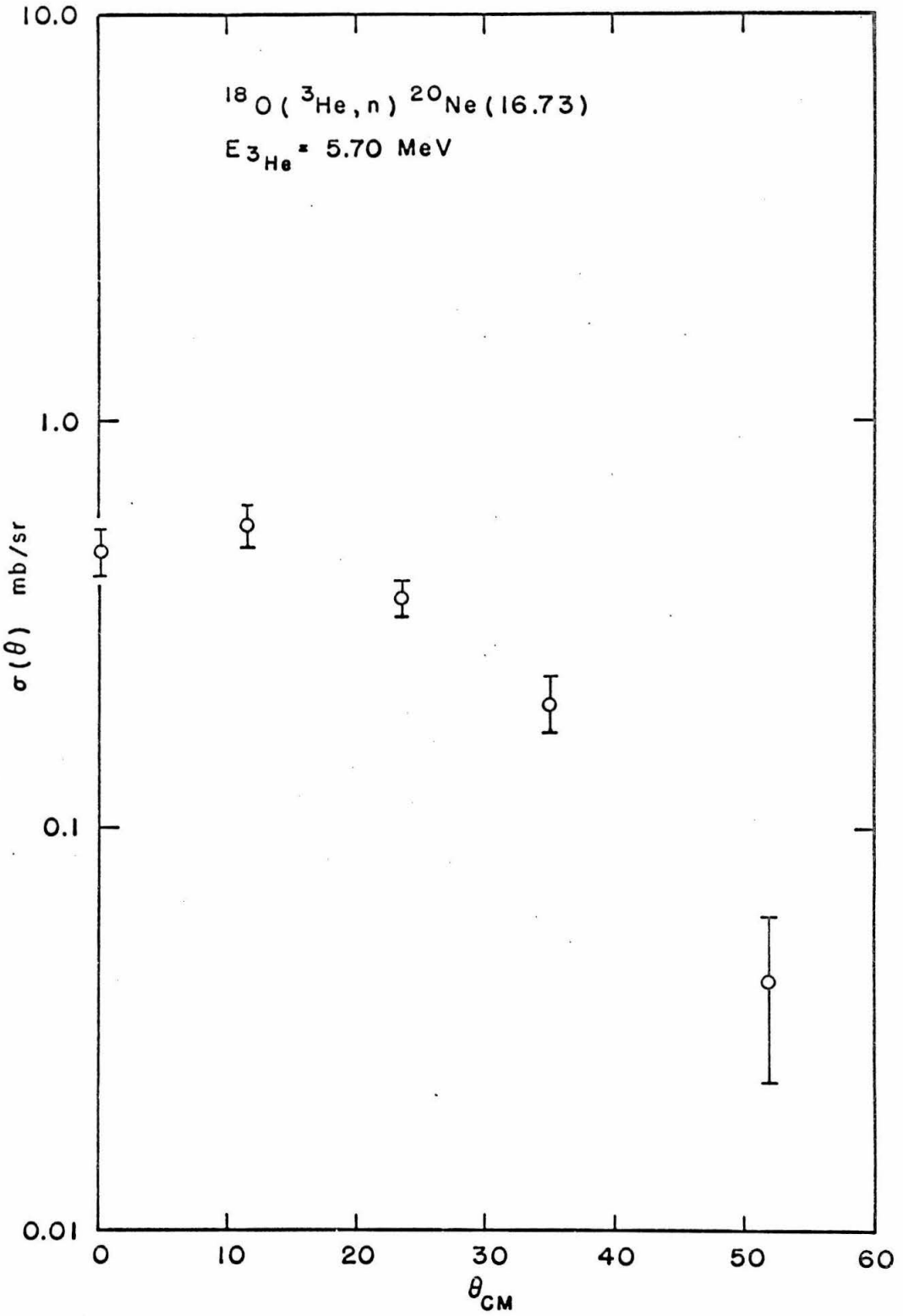
10.0
1.0
0.1
0.01
$^{18}O(^{3}He,n)^{20}Ne(16.73)$
$E_{^{3}He}$ = 5.70 MeV
σ(θ) mb/sr
0
10
20
30
40
50
60
θ_{CM}

Figure 50

Angular distribution of neutrons from the $O^{18}(He^3, n)$ $Ne^{20}(16.730)$ at 7.33 MeV incident energy. The error bars include contributions from counting statistics, and uncertainties in mean background, detector efficiency, and beam current integration. In addition to the errors denoted by the flags, there is an estimated uncertainty of $\pm$ 10% in the absolute normalization. The smooth curves are DWBA fits for L = 0, 1, and 2, with only the normalization treated as a free parameter. The experimental distribution is obviously L = 0. (See page 71.)

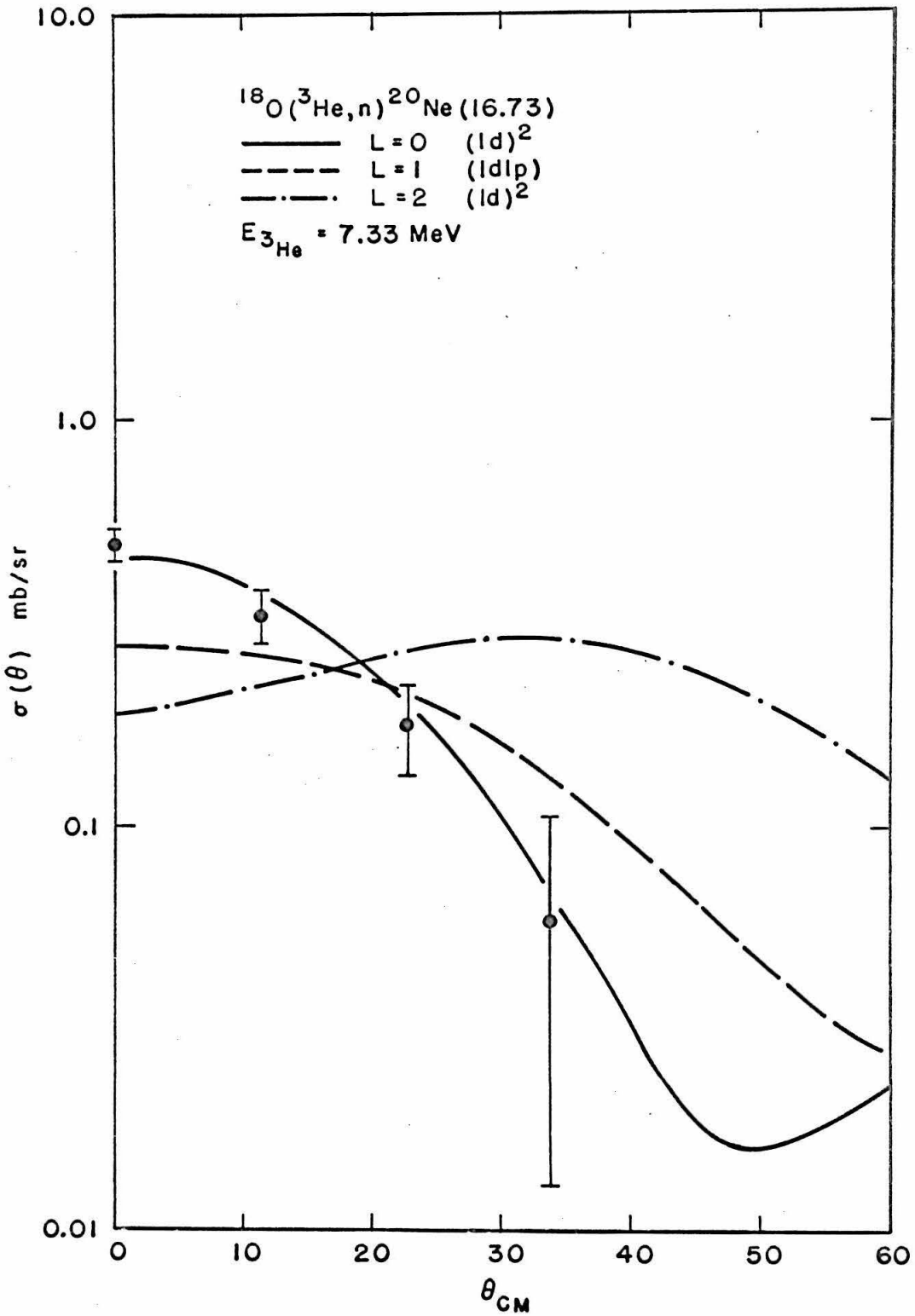
$^{18}O(^{3}He,n)^{20}Ne(16.73)$
L = 0 $(1d)^2$
L = 1 (1d1p)
L = 2 $(1d)^2$
$E_{^3He}$ = 7.33 MeV
10.0
1.0
0.1
0.01
$\sigma(\theta)$ mb/sr
0
10
20
30
40
50
60
θ_{CM}

Figure 51

Energy systematics of higher isospin states accessible with (He^3, n) reactions on targets with $7 \leq A \leq 27$. The Coulomb barrier in the laboratory system, and thresholds for production of the lowest T = 3/2 and T = 2 states are plotted versus A. The Coulomb barriers were calculated using the expression

$$E_c = 1.03 \frac{A+3}{A} \frac{Z_1 Z_2}{A^{1/3} + 3^{1/3}} .$$

The open triangle and circles denote values obtained from an estimate of the excitation energies using a method described on page 39. The experimental implications of this graph are discussed on page 72.

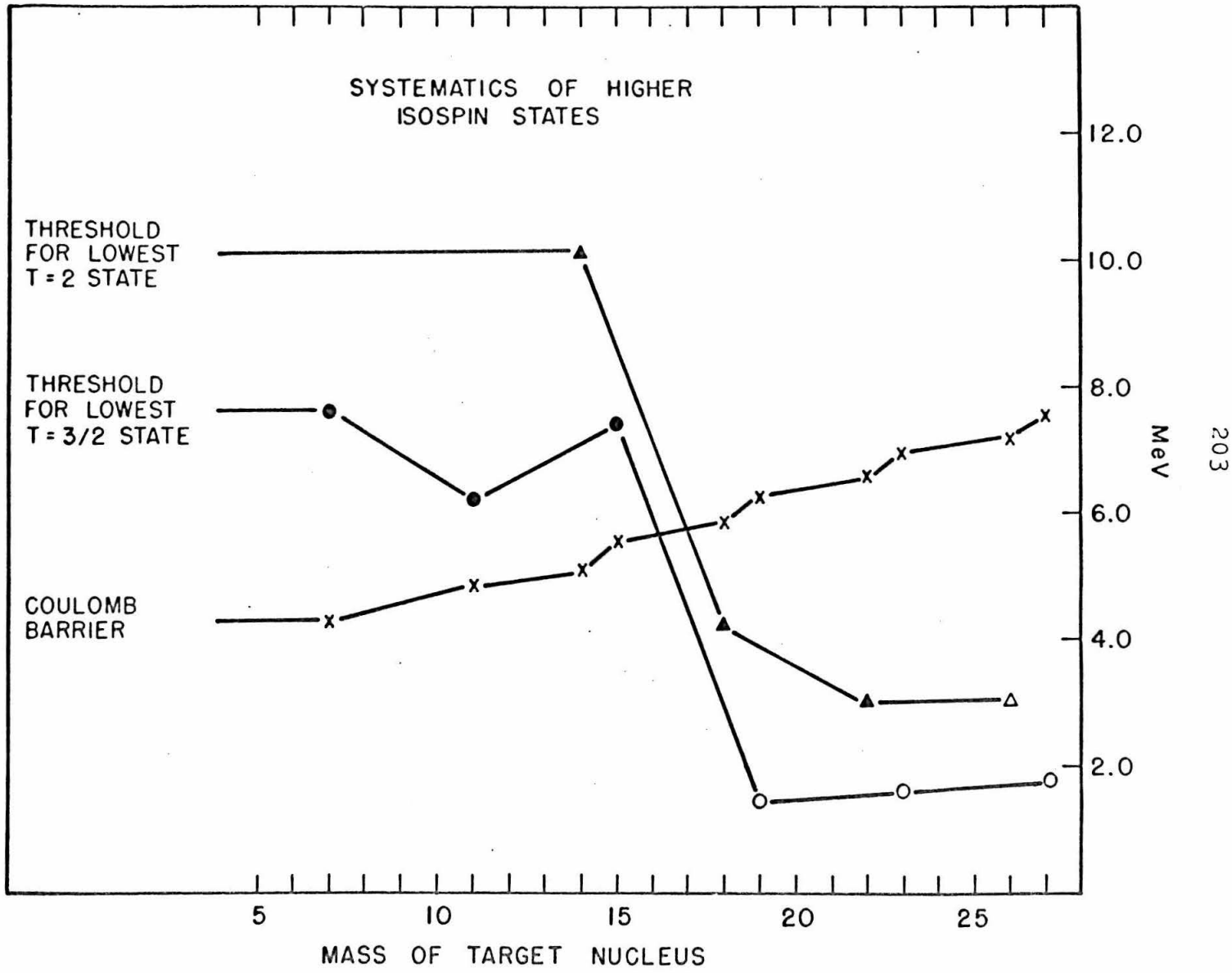
SYSTEMATICS OF HIGHER
ISOSPIN STATES
THRESHOLD
FOR LOWEST
T = 2 STATE
THRESHOLD
FOR LOWEST
T = 3/2 STATE
COULOMB
BARRIER
12.0
10.0
8.0
6.0
4.0
2.0
MeV
5
10
15
20
25
MASS OF TARGET NUCLEUS

Figure 52

Time-averaged values of the pulsed beam and difference currents as a function of phase. The exact shape of these curves depends upon the detailed geometry of the beam handling system. For the Caltech Tandem $\varphi_1 - \varphi_2 \approx 40^{\circ}$.
(See page 74.)

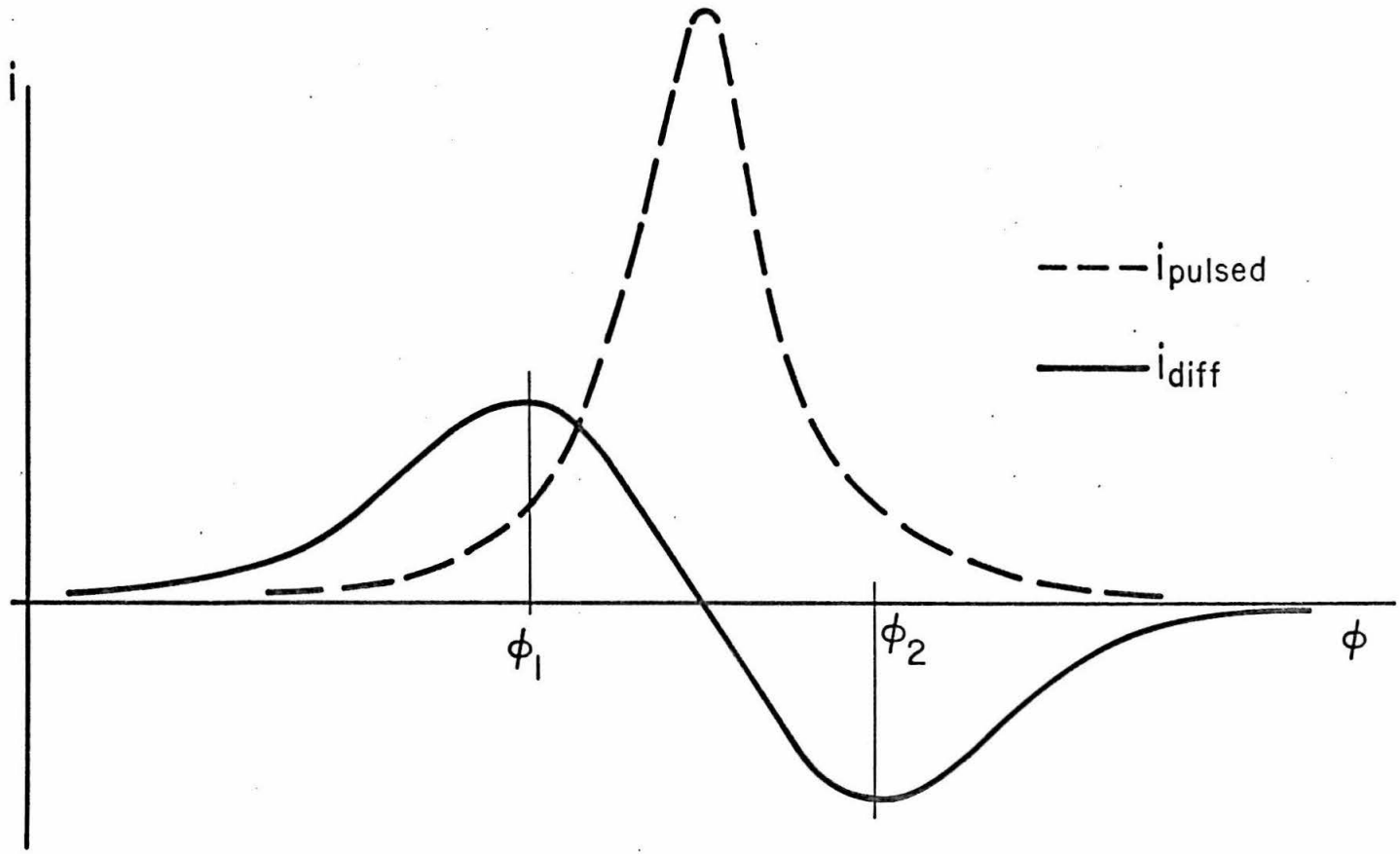
i
i_{pulsed}
i_{diff}
ϕ_1
ϕ_2
ϕ

Figure 53

Circuit diagram of the electronic phase-shifter used in the phase-stabilized beam-pulsing system. The feedback signal comes from the vacuum tube phase detector and is capable of varying the phase by 40^{o}. Three back-biased silicon diodes are used as a voltage-controlled capacitor. (See page 74.)

PHASE SHIFTING NETWORK

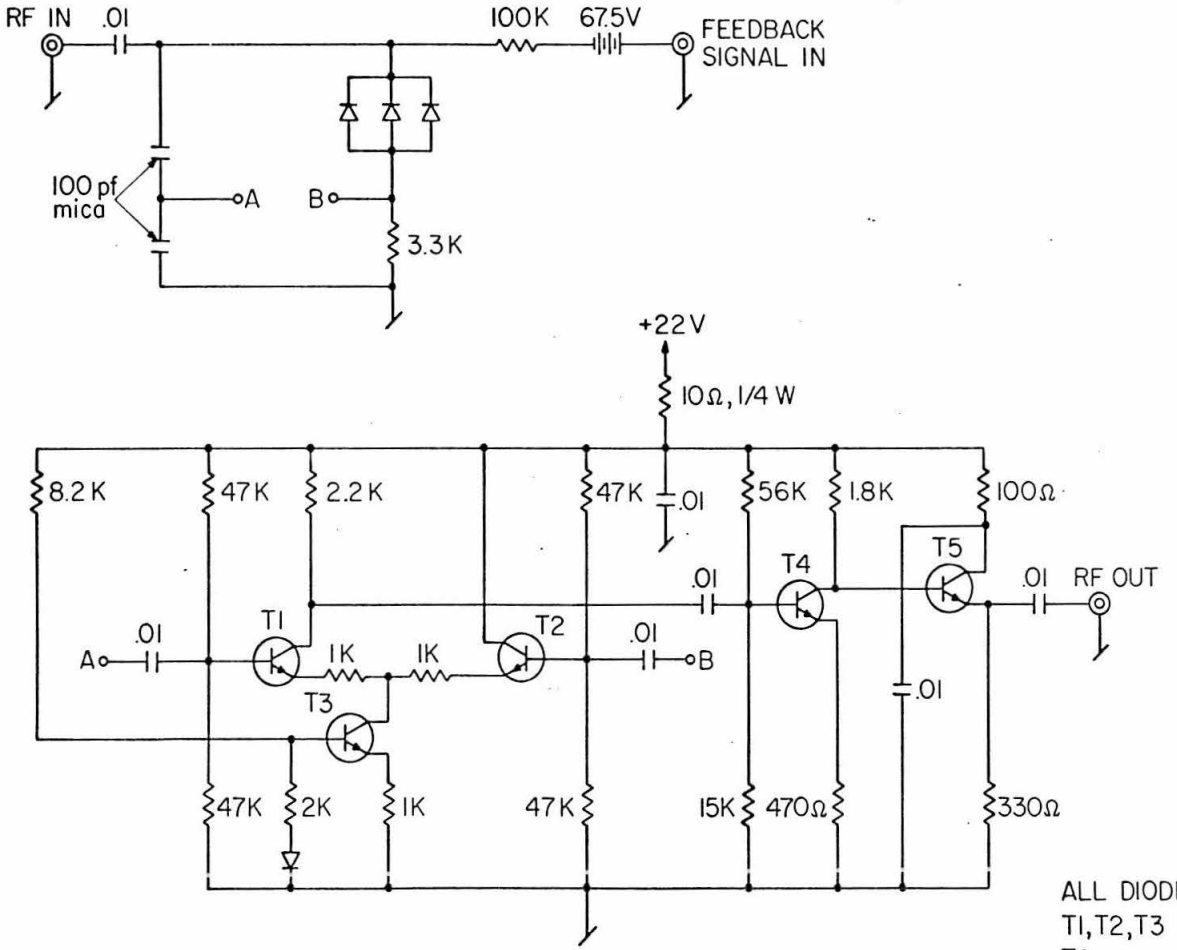

ALL DIODES IN2070

T1, T2, T3	2N3646
T4	2N3904
T5	2N3391